

INTERFACIAL INSTABILITIES IN REACTING FLOWS

by

Nitesh Omprakash Attal

A dissertation submitted to the faculty of  
The University of North Carolina at Charlotte  
in partial fulfillment of the requirements  
for the degree of Doctor of Philosophy in  
Mechanical Engineering

Charlotte

2016

Approved by:

---

Dr. Praveen Ramaprabhu

---

Dr. Mesbah Uddin

---

Dr. Aixi Zhou

---

Dr. Joel Avrin



## ABSTRACT

NITESH OMPRAKASH ATTAL. Interfacial instabilities in reacting flows. (Under the direction of DR. PRAVEEN RAMAPRABHU)

Fluid instabilities, particularly interfacial instabilities, have proven to be a powerful mechanism in driving and sustaining combustion processes in several devices of practical interest. Modern combustors are in fact designed to exploit the mixing and combustion characteristics associated with a broad class of canonical, interfacial instabilities. In spite of their relevance to combustor design, a detailed understanding of such flows has been elusive. While much progress has been made in gaining insights in to the dynamics of shear driven flows, an understanding of the interaction between combustion processes and other interfacial instabilities remains preliminary. In this work, we characterize Rayleigh-Taylor (RT) instability and the shock-driven Richtmyer-Meshkov (RM) instability in the context of combustion. The vast catalogue of research on non-reacting RT and RM flows has demonstrated these instabilities can be manipulated to achieve more efficient and aggressive mixing in comparison with the canonical Kelvin-Helmholtz (KH) problem. This has motivated our efforts to understand RT/RM instability development in the presence of chemical reactions leading to combustion and heat release – we present results from carefully designed numerical simulations of such flows and identify opportunities and challenges in this research space.

## DEDICATION

This dissertation is dedicated to my loving wife and parents.

## ACKNOWLEDGMENTS

My research would not have been possible, if I did not get encouragement and support from a number of people. Their words and suggestions often boosted my courage and determination. I would like to thank my graduate advisor, Dr. Praveen Ramaprabhu, who trusted me and provided the opportunity to work on this complex field of research. He was always accessible and his perpetual energy and enthusiasm motivated me. I would like to thank my committee members Drs. Mesbah Uddin, Aixi Zhou and Joel Avrin for spending their valuable time in reviewing my dissertation. I would like to acknowledge the Flash center at the University of Chicago for providing access to the FLASH code. FLASH was developed by FLASH center at U. Chicago with support from DOE NNSA-ASC OASCR. I would like to thank the National Institute of Computational Sciences, University of Tennessee and National Center of Computational Sciences, Oak Ridge National Laboratory and Argonne Leadership Computing Facility (Argonne National Laboratory) for computer time awarded. On a more personal level, I would like to mention my parents, whose supportive role in my education and upbringing is beyond words. They have always stood by me through the difficult times. I would like to thank all my friends at UNC, Charlotte who made life on and off campus enjoyable. Above all I would like to thank my wife for her love and constant support that kept me sane over the past few years.

## TABLE OF CONTENTS

LIST OF FIGURES	viii
LIST OF TABLES	xiv
CHAPTER 1: INTRODUCTION	1
CHAPTER 2: NUMERICAL METHODS AND CAPABILITIES	10
2.1 FLASH Code Description	13
2.1.1 Hydro Unit	13
2.1.2 EOS Unit	14
2.1.3 Burn Module	15
2.1.4 Diffusion Unit	15
2.2 Development of Chemical Reaction Solvers and Auxiliary Modules	16
2.2.1 Temperature-dependent Equation of State	16
2.2.2 Implicit Mass and Viscous Diffusion Equation Solvers	18
2.2.3 Temperature-dependent Material Properties Database	20
2.2.4 Burn Module	22
CHAPTER 3: PROBLEM FORMULATION AND UNPERTURBED RAYLEIGH-TAYLOR FLAMES	26
3.1 Problem Formulation and Numerical Methods	26
3.2 Unperturbed Flames	35
CHAPTER 4: TWO LAYER RAYLEIGH-TAYLOR FLAMES	40
4.1 Single Mode Perturbation	40
4.2 Multimode Perturbation	48
CHAPTER 5: THREE LAYER RAYLEIGH-TAYLOR FLAMES	57
5.1 Single Mode Perturbation	57
5.2 Multimode Perturbation	66

CHAPTER 6: RICHTMYER-MESHKOV FLAMES	76
6.1 Problem Setup and Numerical Method	76
6.2 Unperturbed Interfaces (cases 31-35)	81
6.3 Non-Reacting RM (CASES 36-41)	87
6.4 Unshocked Perturbed Flames (CASES 42-48)	92
6.5 A Perturbed Flame Accelerated by an Incident Shock (CASES 49-54)	104
6.6 Reshocked Flames (CASE 55)	110
CHAPTER 7: SUMMARY AND CONCLUSIONS	114
REFERENCES	121
APPENDIX A: FLASH VALIDATION	130

## LIST OF FIGURES

- FIGURE 3.1: (a) Schematic of the proposed problem setup to investigate reactive Rayleigh-Taylor Instability and (b) scaled density  $(\rho^* = (\rho - \rho_f) / (\rho_a - \rho_f))$  (solid lines) and pressure  $(P / P_0)$  (dashed lines) across an unperturbed interface  $h_0 = 0$  at  $A=0.2$  (gray) and  $A=0.6$  (black). 1D simulations employed a background acceleration of  $g = 0.6 \times 10^4 g_0$ , where  $g_0 = -981 \text{ cm} / \text{s}^2$ . 28
- FIGURE 3.2: Mixture fraction, scaled density  $(\rho^* = (\rho - \rho_f) / (\rho_a - \rho_f))$  and temperature at  $t=2\text{ms}$  for flames at (a)  $A=0.2$  and (b)  $A=0.6$ . 36
- FIGURE 3.3: Time evolution of Atwood numbers corresponding to fuel-flame  $(A_{f-fl} = (\rho_{fl} - \rho_f) / (\rho_{fl} + \rho_f))$  and flame-air  $(A_{fl-a} = (\rho_a - \rho_{fl}) / (\rho_a + \rho_{fl}))$  interfaces from an unperturbed low Atwood  $(A_{f-a} = 0.2)$  simulation. 37
- FIGURE 3.4: Normalized flame density  $(\rho_{fl}^* = (\rho_{fl} - \rho_f) / (\rho_a - \rho_f))$  from eq. (3.15) and 1D simulations (symbols) plotted against the initial Atwood number associated with the fuel-air interface. Flames with  $\rho_{fl}^* < 0$  develop a three-layer configuration. 39
- FIGURE 4.1: High A interface evolution represented by scaled density in (b-e) inert (case 12) and (f-i) reacting (without 3<sup>rd</sup> layer) RT unstable interfaces (case 13) realized at scaled times  $\tau = 2, 4, 6$  and  $10$  respectively. The initial interface is shown in figure (a) while iso-contours of fuel(black), flame-sheet(gray) and air(white) surfaces are overlaid on scaled density. 42
- FIGURE 4.2: (a) Scaled bubble and spike amplitudes and corresponding (b) Froude numbers for reacting and non-reacting single mode interfaces ( $A = 0.6$ ) against scaled time  $(\tau = t\sqrt{Agk})$ . 42
- FIGURE 4.3: (a) Evolution of the flame expansion parameter  $(\sigma = \rho_{Z_{st_{unburnt}}} / \rho_{Z_{st_{burnt}}})$  for low and high A unperturbed interfaces and (b) comparison of the asymptotic expansion parameter  $(\sigma|_{t \rightarrow \infty})$  with predictions from equilibrium chemistry (equation 4.8). 46
- FIGURE 4.4: Evolution of the mixing zone represented through iso-surfaces of  $4Z(1-Z)$  from  $A = 0.6$  inert and reacting RT interfaces. Images shown correspond to scaled times  $\tau =$  (a, f) 1, (b, g) 5, (c, h) 10, (d, i) 15 and (e, j) 20. The initial interface location  $(x_i)$  is indicated by horizontal arrows in each realization. 47

- FIGURE 4.5: Scaled profiles of planar-averaged mixture fraction and density from  $A = 0.6$ , multimode (a-b) inert and (c-d) reacting interfaces obtained at intervals of  $\Delta\tau = 1$  in the range  $\tau = 5-22$ . The 1d flame profile (case 3) is shown with a thick grey line for comparison. The profiles are plotted against the coordinate  $\left(\xi = (x - x_{Z_{50}}) / (x_{Z_{01}} - x_{Z_{99}})\right)$ . 50
- FIGURE 4.6: Bubble fronts for high  $A$  (a-b) inert and (c-d) reacting interfaces at early ( $\tau = 5$ ) and late times ( $\tau = 20$ ). 52
- FIGURE 4.7: Spike fronts for high  $A$  (a-b) inert and (c-d) reacting interfaces at early ( $\tau = 5$ ) and late times ( $\tau = 20$ ). 53
- FIGURE 4.8: Evolution of mean (a) bubble and (b) spike diameters obtained from the autocorrelation procedure of [3] and the corresponding (c) self-similarity parameter  $(\beta_{b,s})$  plotted against scaled time for  $A = 0.6$ , inert and reacting RT flow. 53
- FIGURE 4.9: Evolution of (a) molecular mixing parameter  $(\theta)$  and scaled bubble and spike amplitude for high  $A$  ( $A=0.6$ ) inert and reacting interfaces against scaled time. The corresponding amplitude growth constants  $(\alpha_{b,s})$  are shown in (b). 55
- FIGURE 5.1: Low  $A$  interface evolution represented by scaled density in (b-e) inert (case 14), globally (f-i) unstable (case 15) and (j-m) stable (case 16) reacting (with 3<sup>rd</sup> layer) RT unstable interfaces realized at scaled times  $\tau = 2, 4, 6$  and 10 respectively. The initial interface is shown in figure (a) while iso-contours of fuel(black), flame-sheet(gray) and air(white) surfaces are overlaid on scaled density. 59
- FIGURE 5.2: Schematic representation of the formation of the third layer in a low Atwood number, fuel-air mixture with a locally stable fuel-flame and locally unstable flame-air interfaces. 60
- FIGURE 5.3: Scaled separation distance  $(ks_d)$  and amplitude  $(kh)$  of the fuel ( $Z_{99}$ ) and flame sheet( $Z_{51}$ ) surfaces plotted against scaled time  $\left(\tau = t\sqrt{A^*gk}\right)$  obtained from simulations with  $\lambda = 0.5 \text{ cm}$  and  $g = 0.6 \times 10^4 g_0$  for  $A_{f-a} = 0.2$  reacting interface. 62
- FIGURE 5.4: (a) Effect of imposed acceleration on the scaled separation distance: Plot of  $(ks_d)$  against scaled time  $\left(\tau = t\sqrt{A^*gk}\right)$ . (b) Fuel surface stability durations as predicted by equation (5.2) and observed in numerical simulations (NS). 63

FIGURE 5.5: (a) Scaled bubble and spike amplitudes and corresponding (b) Froude numbers for reacting and non-reacting single mode interfaces ( $A = 0.2$ ) against scaled time ( $\tau = t\sqrt{A^*gk}$ ). 64

FIGURE 5.6: Schematic of a (a) globally unstable ( $gA_{f-a} < 0$ ) and (b) globally stable ( $gA_{f-a} > 0$ ) three layer RT configuration induced by the flame for  $A_{f-a} = 0.2$ . (c) The scaled density profile ( $\rho^*$ ) obtained from an unperturbed 1D simulation. 68

FIGURE 5.7: Isosurfaces of scaled density  $\rho^* = (\rho - \rho_f) / (\rho_a - \rho_f)$  from inert (left), and reacting interfaces with  $A_{f-a}g < 0$  (middle) and  $A_{f-a}g > 0$  (right column) at scaled times  $\tau = 1.6$  (a, e, i), 5.0 (b, f, j), 10.0 (c, g, k) and 19.0 (d, h, l). The initial interface location ( $x_i$ ) is indicated by horizontal arrows for each realization. 70

FIGURE 5.8: (a) Amplitudes of bubble and spike fronts scaled by box width ( $L$ ) and (b) corresponding mix growth rate ( $\alpha_{b,s}$ ) plotted against scaled time ( $\tau$ ) for cases 28-30. 72

FIGURE 5.9: Plot of surface area of the flame sheet ( $Z_{st}$ ) scaled by the area of box cross section against scaled time ( $\tau$ ) for cases 28-30. 75

FIGURE 6.1: (a) Schematic of the problem setup and (b) x-profiles of the scaled initial density  $\rho^* = (\rho - \rho_{H_2}) / (\rho_{O_2} - \rho_{H_2})$  and mixture fraction ( $Z$ ) from 1D simulation with  $\Delta = 0.12$  m. 78

FIGURE 6.2: (a) Interface position and (b) the corresponding velocity as a function of time from 1D simulations of a reacting front without an incident shock. Results are shown for both a sharp ( $\Delta = 3.8 \times 10^{-3}$  m) and diffuse ( $\Delta = 0.12$  m) front. 83

FIGURE 6.3: Axial profiles of the scaled (a) pressure, (b) density, (c) temperature, and (d) mixture fraction at times 0 s, 15  $\mu$ s, and 60  $\mu$ s from 1D simulations of a reacting front without an incident shock, and with  $\Delta = 0.12$  m. 84

FIGURE 6.4: (a) Interface position based on  $Z_{50}$  and (b) the corresponding velocity as a function of time from 1D simulations of a reacting front with a Mach 1.2 incident shock. Results are shown for both a sharp ( $\Delta = 3.8 \times 10^{-3}$  m) and diffuse ( $\Delta = 0.12$  m) front, as well as for the baseline non-reacting (*cold*) front. 85

FIGURE 6.5: Axial profiles of the scaled (a) pressure, (b) density, (c) temperature, and (d) mixture fraction at times 0 s, 76  $\mu$ s, 0.15 ms and 0.3 ms from 1D simulations of a reacting, diffuse ( $\Delta = 0.12$  m) front with a Mach 1.2 incident shock. 86

- FIGURE 6.6: Contours of  $H_2$  mass fraction (top) and scaled density  $\rho^*$  (bottom) 88  
from 2D simulations of a perturbed, non-reacting interface with  $\Delta/h_0 = 4$ , and driven  
by a Mach 1.2 incident shock. The images are shown at  $kV_0^+(t-t_0) =$  (a)  $-1.4 \times 10^{-2}$   
, (b) 0.38, (c) 0.77, (d) 1.96, and (e) 3.93.
- FIGURE 6.7: Contours of  $H_2$  mass fraction (top) and scaled density  $\rho^*$  (bottom) 88  
from 2D simulations of a perturbed, non-reacting interface with  $\Delta/h_0 = 64$ , and  
driven by a Mach 1.2 incident shock. The images are shown at  $kV_0^+(t-t_0) =$  (a) -  
0.11, (b) 0.27, (c) 0.65, (d) 1.79, and (e) 3.69.
- FIGURE 6.8: Evolution of (a) scaled perturbation amplitudes based on distance 90  
from peak-to-peak of  $Z_{50}$  and (b) the corresponding growth rates as a function of  
scaled time from 2D simulations of a non-reacting front with a Mach 1.2 incident  
shock. Results shown are from simulations with varying  $\Delta/h_0$ .
- FIGURE 6.9: Growth rate reduction factor ( $\psi = V_0^+/V$ ) from the 2D non-reacting, 91  
RM simulations with (a)  $A = 0.5$  and (b)  $A = -0.5$ , plotted against scaled thickness  
( $\delta/\lambda$ ). The squares indicate  $\psi$  calculated from pre-shock quantities, while circles  
indicate the use of post-shock quantities. The prediction of Eq. 1.5(b) with  $C = 2.83$   
is shown as the solid line.
- FIGURE 6.10: Schematic of the pressure waves from burning at a 2D front (a) and 92  
the resulting combustion waves (b) and (c).
- FIGURE 6.11: Scaled peak pressure ( $\langle p \rangle_{max}/p_0$ ) associated with the combustion 94  
waves plotted against the scaled interface thickness ( $\Delta/h_0$ ) for the simulations  
described in section 6.4.
- FIGURE 6.12: A schematic of the interaction of a combustion wave (figure 6.10 (b)) 95  
with the interface ( $Z_{50}$ ). Inset shows incident pressure pulses with a separation  
distance of  $2h_0$ . Such a modulated combustion wave can lead to decompression-  
driven growth of the interface.
- FIGURE 6.13: Contours of (top to bottom) the scaled density  $\rho^*$ ,  $H_2O$  mass 98  
fraction and the scaled temperature  $T^*$  from 2D simulations of a perturbed, reacting interface  
with  $\Delta/h_0 = 2$ , with no incident shock. The images are shown at  $kV_0^+(t-t_0) =$  (a)  
 $-1.6 \times 10^{-4}$ , (b)  $3.4 \times 10^{-2}$ , (c)  $6.8 \times 10^{-2}$ , (d) 0.17, and (e) 0.34.
- FIGURE 6.14: Contours of (top to bottom) the scaled density  $\rho^*$ ,  $H_2O$  mass 100  
fraction and the scaled temperature  $T^*$  from 2D simulations of a perturbed, reacting

interface with  $\Delta/h_0 = 64$ , with no incident shock. The images are shown at  $kV_0^+(t-t_0) =$  (a)  $-9.6 \times 10^{-2}$ , (b) 0.19, (c) 0.48, (d) 1.34, and (e) 2.77.

FIGURE 6.15: Evolution of (a) scaled perturbation amplitudes based on distance from peak-to-peak of  $Z_{50}$  and (b) the corresponding growth rates as a function of scaled time from 2D simulations of a reacting front with no incident shock. Results are shown from simulations with varying  $\Delta/h_0$ . 102

FIGURE 6.16: Time varying reduction factor  $\psi(t)$  from simulations of an unshocked, reacting flame with different initial values of  $\Delta/h_0$ . 104

FIGURE 6.17: Contours of (top to bottom) the scaled density  $\rho^*$ ,  $H_2O$  mass fraction and the scaled temperature  $T^*$  from 2D simulations of a perturbed, reacting interface with  $\Delta/h_0 = 2$ , and driven by a Mach 1.2 incident shock. The images are shown at  $kV_0^+(t-t_0) =$  (a)  $-1.2 \times 10^{-2}$ , (b) 0.39, (c) 0.79, (d) 1.99, and (e) 3.99. 105

FIGURE 6.18: Contours of (top to bottom) the scaled density  $\rho^*$ ,  $H_2O$  mass fraction and the scaled temperature  $T^*$  from 2D simulations of a perturbed, reacting interface with  $\Delta/h_0 = 64$ , and driven by a Mach 1.2 incident shock. The images are shown at  $kV_0^+(t-t_0) =$  (a)  $-9.5 \times 10^{-2}$ , (b) 0.21, (c) 0.51, (d) 1.41, and (e) 2.92. 106

FIGURE 6.19: Time varying reduction factor  $\psi(t)$  from simulations of a shocked, reacting flame with different initial values of  $\Delta/h_0$ . 110

FIGURE 6.20: Evolution of (a) scaled perturbation amplitudes based on distance from peak-to-peak of  $Z_{50}$  (b) and the corresponding growth rates as a function of scaled time from 2D simulations of a reacting front with a Mach 1.2 incident shock. Results shown are from simulations with varying  $\Delta/h_0$ . 110

FIGURE 6.21: Contours of  $H_2O$  mass fraction (top) and scaled temperature  $T^*$  (bottom) from 2D simulations of a perturbed, reacting interface with  $\Delta/h_0 = 2.0$ , and driven by a Mach 1.2 incident shock. The images are shown at (a)  $kV_0^+(t-t_0) = 1.59$  just before reshock and (b)  $kV_0^+(t-t_0) = 7.99$  at late time after reshock. 111

FIGURE 6.22: Growth of the mixing layer width ( $W_{mix}$ ) and the integral planar averaged combustion efficiency  $(\int \langle \eta_c \rangle dx) / W_{mix}$  plotted against scaled time ( $kV_0^+(t-t_0)$ ), for reacting RM with reshock. 113

FIGURE A.1 (a) :Temperature and adiabatic index ( $\gamma$ ) for hydrogen from FLASH compared with high accuracy data compiled by NIST[67] at different densities. 132

FIGURE A.1(b): Temperature and adiabatic index ( $\gamma$ ) for oxygen from FLASH compared with high accuracy data compiled by NIST[67] at different densities.	133
FIGURE A.1(c): Temperature and adiabatic index ( $\gamma$ ) for nitrogen from FLASH compared with high accuracy data compiled by NIST[67] at different densities.	134
FIGURE A.2: Schematic of computational domain for simulation of $2D$ axisymmetric laminar jet.	136
FIGURE A.3: Steady-state, non-dimensional, axial velocity from FLASH compared with DNS[69] and analytic solution[68].	137
FIGURE A.4: Steady-state, non-dimensional momentum $\dot{M}(x)/\dot{M}_0$ and mass $\dot{m}(x)/\dot{m}_0$ fluxes from FLASH. $\dot{M}_0$ and $\dot{m}_0$ are inlet values.	138
FIGURE A.5: Tangential velocity profiles in a decaying vortex at $t = 0.1s$ (initial condition), $t = 0.2s$ and $t = 0.5s$ (a) analytic solution [70] and FLASH (implicit viscous diffusion), (b) analytic solution [70] and FLASH (flux-based viscous diffusion)	140
FIGURE A.6: Plots at $t = 0s$ of (a) mass fraction of Hydrogen, and (b) temperature.	142
FIGURE A.7: Plots at $t = 100\mu s$ for case A.1 (a) mass fraction of $H_2$ , (b) temperature and case A.2 (c) mass fraction of $H_2$ , (d) temperature.	144

## LIST OF TABLES

TABLE 2.1: Summary of capabilities added to FLASH for simulating chemically reacting flows with heat addition.	12
TABLE 3.1: Summary of simulation performed to characterize RT flames.	33
TABLE 6.1: Summary of simulations performed to characterize RM flames.	81
TABLE A.1: 2D Hydrogen ring (reacting) simulations performed using FLASH.	143

## CHAPTER 1: INTRODUCTION

The most common source of energy generation remains the combustion of hydrocarbon based fuel. The energy released in the process of combustion is used to power a diverse array of engineering applications, such as gas turbines, power plants, internal combustion engines, etc. As a large number of these engineering applications consume fuel in a liquid or gaseous state of matter, the study of combustion is inevitably coupled with flow phenomena. Fluid instabilities, particularly interfacial instabilities, have proven to be a powerful mechanism in driving and sustaining combustion processes through the manipulation of such flow phenomena in several devices of practical interest. These instabilities provide a pathway towards chaotic and turbulent flow field, developing from regular, organized structures. When coupled with exothermic reactions, they can provide substantial insights into the turbulent flow physics governing the energy generation in combustors. Modern combustors are in fact designed to exploit the mixing and combustion characteristics associated with a broad class of canonical, interfacial instabilities.

Turbulent mixing triggered by interfacial instabilities[1-4] is a fundamental process that dominates several engineering applications and natural phenomena. In many instances, the turbulence is profoundly modified by heat release at low or high energy densities, and product formation from chemical or nuclear reactions. Furthermore, when the mixing occurs across an interface that initially separates a fuel from an oxidizer medium in a non-premixed configuration, the turbulent mixing is a rate-limiting step that dictates the

progress of the reactions at the flame site. Thus, the flow affects the flame and vice-versa. In a recent, comprehensive review of turbulent mixing, Dimotakis[5] proposed a hierarchy of mixing phenomena extending from passive scalar mixing (Level-1) to so-called Level-3 mixing where the active coupling described above is dominant. While such complex interactions are important in describing flow conditions as they exist in engineering applications, the vast majority of turbulence models that seek to obtain reduced order descriptions of the flow assume[6] self-similar, statistically steady, universal behavior. Thus, reliable data from experiments and simulations is in great demand to verify the validity of these hypotheses, but has not been forthcoming due to challenges in accurately diagnosing these complex flows. While several innovative experimental strategies are available and provide high-quality data, obtaining higher-order moments from experiments of turbulent combustion is all but impossible. The research described herein attempts to break this impasse by performing systematic, high resolution simulations of a new class of idealized flow problems to understand the role of interfacial instabilities in reacting flows.

Interfacial instabilities may be characterized by the driving mechanism, such as shear, buoyancy or impulse from a shock. The Kelvin-Helmholtz (KH) instability occurs at a sharp or diffuse interface separating two streams at different velocities, so that the shear ( $\Delta U$ ) serves to drive the growth of imposed perturbations at the interface. Much of the research on KH instabilities has been motivated by its central role in mixing fuel and oxidizer in several commonly used combustor designs. KH instabilities, whether they occur in a mixing layer, a planar or cylindrical jet have provided a useful canonical framework for understanding non-premixed combustion. In fact, the design of many modern day combustor devices is acutely informed by the desire to exploit the dynamics of KH-driven

mixing between fuel and oxidizer streams. However, there exist alternate combustor designs that exploit the mixing characteristics of other interfacial instabilities such as the buoyancy driven Rayleigh-Taylor (RT) [7,8] or the shock-driven Richtmyer-Meshkov (RM) [9,10] flows. In spite of the importance of these flows in recent combustor designs [11-14], a detailed and comprehensive understanding has not emerged. This is especially true when these flows occur in non-premixed configurations. In this work, we have investigated the dynamics and properties of RT and RM instabilities in the context of non-premixed flames.

The Rayleigh-Taylor instability [7,8] occurs at a perturbed interface between fluids of different densities when the light fluid is accelerated in to the heavier fluid. Infinitesimal perturbations on the interface will grow first exponentially (linear stage), and then secularly with a constant velocity (nonlinear stage). When multiple modes are present, nonlinear interactions are possible yielding an eventual turbulent, mixed state that is self-similar. RTI-driven mixing afflicts a wide range of physical phenomena including energy yield in Inertial Confinement Fusion [15], mantle dynamics [16], type Ia supernovae detonation[17-19], geophysical flows [20-22], and mixing in centrifugal combustors [12,13,23] and liquid rocket engines [24]. Owing to its significance in a wide range of applications, the non-reacting RT instability has been extensively investigated over the last five decades[1,7,8,25-27]. From this body of work, a consensus has emerged on the dynamics of the turbulent RT mixing layer. A single scale perturbation of wave number,  $k = 2\pi/\lambda$  (for a wavelength  $\lambda$ ) and amplitude  $h_0$  ( $h_0 \ll \lambda$ ) at the interface grow exponentially under the influence of imposed acceleration ‘g’ with a growth rate[28],

$$n = \sqrt{Agk} \quad (1.1)$$

where the Atwood number  $\left( A = \frac{\rho_h - \rho_l}{\rho_h + \rho_l} \right)$  parameterizes the density difference between the heavy( $\rho_h$ ) and light( $\rho_l$ ) fluid. The interface growth at this stage is characterized by symmetric interpenetration of heavy and light fluid. Eventually( $kh \sim 1$ ) the heavy fluid penetrates further into the light to form ‘spikes’ while light fluid rises into the heavy as ‘bubbles’. The growth at this stage is marked by terminal bubble( $V_b$ ) and spike( $V_s$ ) velocities[29],

$$V_{b,s} = \sqrt{\frac{2Ag}{C(1 \pm A)k}} \quad (1.2)$$

where  $C = 1(3)$  for 3D(2D) geometry. When the interface is initialized with a broad spectrum of modes, the resulting flow has been observed to be self-similar, with the width of the mixing layer evolving quadratically in time according to [2,3,27,30,31]

$$h_{b/s} = \alpha Agt^2, \quad (1.3)$$

where the subscripts b(s) refers to the advancing bubble(spike) front and  $\alpha$  is the growth rate of the mixing layer.

Recently, RT dynamics has been recognized to play a central role in the performance of combustors that rely primarily on centrifugal loading. Recent innovations in gas turbine design include a shift toward the use of ultra-compact combustors (UCC)[12,13] that operate at high g-loading. UCCs greatly reduce the weight of the gas turbine engine, thus increasing the thrust to weight ratio. In addition, the compact size allows for the inclusion of a reheat cycle between turbines, thus increasing the efficiency of the system. Most common UCC designs involve the admission of fuel and oxidizer streams tangentially in to the combustor chamber, while the g-loading is provided centrifugally through high-speed rotation. Such a configuration in which a non-premixed

fuel and oxidizer interface is subjected to high g-loading ( $\sim 10^4 g_0$ ) is susceptible to the development of the Rayleigh-Taylor (RT) instability[7,8] at the flame site. In spite of this central role, the nature of the interaction between the RT instability and the flame surface has been poorly understood. RT-dominated flames provide unique opportunities in the design and operation of modern combustors, which cannot be realized through device designs that rely primarily on shear-driven mixing to enhance combustion. For instance, in the unstable regime, RT growth will eventually outpace corresponding Kelvin-Helmholtz (KH) growth leading to greater mixing and more efficient burning. Thus, while RT grows self-similarly as  $\sim t^2$ , the shear-driven KH flows evolve as  $\sim t$  (but with a decaying centerline velocity). Correspondingly, the outer scale Reynolds number associated with RT mix (defined as  $Re \equiv \frac{h\dot{h}}{\nu}$ , where  $h(t)$  is the mixing layer width,  $\dot{h}$  is its growth rate and  $\nu$  is the mixture viscosity) will evolve as  $t^3$ , while remaining constant for KH flows[31]. This can allow for more compact designs of combustors, but also render unnecessary several commonly used active and passive mixing augmenters. Furthermore, the faster growth of  $Re$  in RT ensures the flame does not undergo relaminarization upon ignition due to the increased viscosities, a common affliction that impacts several reacting flows. In addition, we have also discovered from preliminary numerical simulations that when the fuel stream is suitably diluted, the flame region can act as a stabilizing layer that can partially suppress the growth of the instability. This effect can be exploited in practical combustors to anchor the flame when necessary or to increase the time for the fuel to burn allowing for cleaner combustion with lesser unburnt fuel. Recently, RTI development in premixed flames [32,33] has been investigated theoretically and numerically, although the corresponding non-premixed configuration has not been studied.

We also discuss non-premixed combustion occurring at the site of a Richtmyer-Meshkov (RM) unstable interface between fuel and oxidizer. The classical RM instability [9,10,34-36] occurs when a perturbed material interface between fluids of different densities is impulsively accelerated, where the acceleration may be provided by a passing shock. The interaction of a shock with a diffusion flame is a familiar situation that arises in many combustion systems. For example, shocks generated within the combustion chamber of an internal combustion engine interact with flame or fuel/air interfaces of various thicknesses. In non-premixed combustion, the shock can enhance mixing at a fuel-air interface through flow instabilities, boosting the rate at which fuel is burnt, thus improving the combustion properties for the system. Shock-flame interactions are also critical in fire safety, where supersonic mixing is undesirable. Furthermore, turbulent mixing and detonation initiated by shock can inform the design parameters and improve the performance of supersonic combustors. While several studies have been devoted to the interaction of shocks with premixed [37,38] and non-premixed [39-41] flames, relatively little attention has been paid to the study of the Richtmyer-Meshkov (RM) instability in the context of shock-flame interaction. We report for the first time, growth rates of the RM instability, when the shock-driven instability occurs at the site of a diffusion flame.

The growth of RM instability depends on the strength of the baroclinic torque deposited at the interface by the shock due to locally misaligned density and pressure gradients. The initial growth of perturbations at the interface is described exactly by a normal-mode analysis of the linearized Euler equations, however no closed-form solution to the growth rate equation exists. Physical insight may be garnered from the so-called impulsive model [9], that treats the instability growth as analogous to an impulsively

accelerated Rayleigh-Taylor instability. Thus, a sinusoidal perturbation will grow according to

$$V_0 = \frac{dh}{dt} = kUAh_0, \quad (1.4)$$

where the  $A$  is the Atwood number defined above, while  $U$  represents the jump velocity imparted to the interface by shock impingement. Naturally, Eq. 1.4 is only valid when the effect of compressibility is minimal, when the incident shock is weak or the fluids have large adiabatic indices. To improve agreement with experiments, Richtmyer [9] suggested using post-shock values (indicated by superscript  $+$ ) for the initial amplitude  $h_0^+$  and the Atwood number  $A^+$  (in Eq. 1.4). Similarly, when the shock travels from a heavy to light medium, Meyer-Blewett [42] prescribe averaging the pre- and post-shock amplitudes to account for a phase reversal of the interface. When the interface has a finite thickness  $\delta$  as a result of mass or viscous diffusion, the RM growth rate is lower than the ideal, and given by [43]

$$\frac{dh}{dt} = \frac{kUA^+h_0^+}{\psi}, \quad (1.5a)$$

$$\psi \approx 1 + C(\delta/\lambda). \quad (1.5b)$$

Eq. 1.5 can be obtained from a modified eigenvalue analysis [43], and has been verified with experimental data (only for  $A > 0$ ) using diffuse gas interfaces by [43] who found the constant  $C \sim 2.8$  for  $A = 0.5$  (we are not aware of a corresponding analysis for RM with  $A < 0$ , but we provide one in chapter 6). Note that classical RM growth at a diffuse interface (Eq. 1.5) is relevant to shock-flame interactions studied in this paper, since in a diffusion flame, the interface thickness determines product formation and the resulting flame properties. When the modal amplitude violates  $kh \ll 1$ , higher harmonics saturate

the growth rate which must now be described by nonlinear models. This stage of development is marked by ‘bubbles’ of light fluid penetrating the heavy, while jets of the heavy fluid are referred to as ‘spikes’.

We describe the modification of the linear RM growth due to burning and heat addition at the material interface of a sinusoidally perturbed  $H_2 - O_2$  diffusion flame. The diffusion thickness is critical to the development of the flame as well as the instability, and has been systematically varied in our study. Early studies of shock interaction with a spherical flame bubble were undertaken experimentally by Markstein [44] who found the baroclinic vorticity deposition led eventually to a chaotic flame. One of the earliest theoretical studies of this problem was by Picone et al. [45], who studied the interaction of a planar shock with a cylindrical region at conditions corresponding to a flame. Several numerical studies followed including the investigation of a shock-flamelet interaction [46,47], shock interaction with a cylindrical jet flame [48], and DDT phenomena in shock-bubble flame interaction [49]. An important variation on this configuration includes the recent experimental study of [50] who achieved combustion due to localized high temperatures from shock-focusing effects within a spherical bubble of premixed combination of  $H_2$ ,  $O_2$ , and  $Xe$ . Similarly, a significant example of such efforts are the linear analysis of [51] and careful simulation study by Khokhlov et al. [52] who investigated the growth of a sinusoidally perturbed premixed flame upon shock impingement, and found the energy release from combustion scaled with the RMI-driven interfacial surface growth[52]. *While these efforts have led to significant insight in to the interaction of a planar shock with a cylindrical flame/bubble and a premixed, sinusoidal flame, we are not aware of studies of RMI at an interface in the context of non-premixed*

*flames*. Understanding RMI in such a setting can be valuable in developing insights in to shock-flame interactions in several engineering applications, where the flame is often non-premixed and the combustion is dictated by instability growth.

The rest of this document is organized as follows: In chapter 2, a brief description of the original FLASH code is followed by detailed description of the modifications we have made to FLASH that enable reactive flow computations, including  $H_2$ -Air chemistry described by three distinct mechanisms,  $CH_4$ -Air chemistry, a comprehensive expansion of the materials database to include temperature-dependent transport properties, an expansion of the EOS suite to include temperature-dependent adiabatic indices for multicomponent mixtures, and extension of the implicit diffusion solver to handle viscous and mass diffusion. In chapter 3-5, we investigate non-premixed RT flames with single wavelength, sinusoidal perturbations and a broadband spectrum of multimode perturbations subject to a constant acceleration using high-resolution, Navier-Stokes simulations. Chapter 6 describes in detail the results from high-resolution, numerical simulations of a single-mode, chemically reacting, Richtmyer-Meshkov (RM) instability, at different interface thicknesses. Finally, some conclusions and opportunities for future work are presented in chapter 7.

## CHAPTER 2: NUMERICAL METHODS AND CAPABILITIES

High-fidelity numerical simulations offer a reliable, non-invasive approach for studying complex flow patterns and multi-physics phenomena. While the advent of massively parallel computing has helped realize large-scale simulations of high Reynolds number flows in idealized geometries, several challenges persist in calculating reacting flows in realistic settings. For instance, Large Eddy Simulations (LES) [53] require careful tuning of inherent model constants and parameters based on the type of flow studied, and thus need to be calibrated using experimental results or computationally expensive Direct Numerical Simulations (DNS). An alternative that has garnered attention recently is the so-called Implicit Large Eddy Simulations (ILES) [54] approach, where scalar and energy dissipation is modeled through the cell-averaged numerical mixing resulting from a finite grid. Such methods are thus ‘model-free’, but their suitability to reacting flows where temperature-dependent transport properties often determine details of the flame properties, is yet to be explored in detail. In this chapter, we have described the development and integration of a chemical reaction suite with the massively parallel FLASH[55] code, originally developed by the FLASH center for Computational Sciences at the University of Chicago. FLASH is a hydrodynamic solver based on the Piecewise Parabolic Method[56] (PPM), and is capable of performing both as a Direct Numerical Simulation (DNS) and an Implicit Large Eddy Simulation (ILES) solver. Thus, the modified code

allows a direct comparison of the accuracy and performance of the ILES paradigm with the DNS approach when applied to reacting flows with heat addition.

In the DNS limit, diffusive transport is computed exactly in FLASH, and is used to update momentum and energy fluxes at every timestep. In contrast, the ILES mode takes advantage of numerical dissipation in so-called ‘under-resolved’ simulations to perform low pass filtering of subgrid modes. Thus, the elimination of an explicit subgrid model makes such schemes attractive for simulation of turbulent flows, as they occur in realistic engineering applications. ILES schemes have been successfully applied to a wide range of challenging problems, including turbulent free shear flow [57], homogeneous compressible turbulence [58] and decaying supersonic turbulence [59]. Where applicable, we compare the performance of ILES and DNS numerical approaches to chemically reacting flow.

The extension to FLASH will render it capable of accurately describing (a)  $H_2$ -Air and  $CH_4$ -Air chemistry, (b) temperature-dependent transport properties relevant to the heat addition process in a reactive flow, (c) multi-species equation of state (EOS) with temperature-dependent adiabatic indices, and (d) diffusion solvers that allow for a range of Lewis/Prandtl/Schmidt numbers. These capabilities are summarized in table 2.1.

When combined with the existing capabilities present in FLASH, the modified solver is expected to find use in investigating a wide range of combustion-related phenomena. The ability to describe reactive flows enables the investigation of the role of chemical timescales, effect of heat addition and flame-induced density variations on a wide variety of laminar and turbulent flows. The existing shock capturing ability in FLASH when combined with the chemical reaction solver will enable simulations of phenomena such as detonation, deflagration, and transition between the two states, which are important

to industrial safety as well as the design of scramjet and pulse detonation engines. FLASH is also equipped with Adaptive Mesh Refinement (AMR), a feature that enables selective refinement of the computational grid, conditioned on local gradients of the primary variables. The data from such simulations can be used for refining and validating turbulent combustion models. Finally, the availability of multiple advection schemes, such as PPM, MUSCL-Hancock and WENO5 within FLASH can be exploited to study their applicability and performance in chemically reacting flow problems.

TABLE 2.1: Summary of capabilities added to FLASH for simulating chemically reacting flows with heat addition.

Relevant Physics	Existing	Added
Reaction Kinetics	Nuclear reaction networks	H <sub>2</sub> -Air and CH <sub>4</sub> -Air
Multi-species Equation of State	Temperature independent	Temperature dependent
Thermal Diffusion	Flux-based Implicit solver	-
Viscous Diffusion	Flux-based	Extended Implicit solver
Mass Diffusion	Flux-based	Extended Implicit solver
Temperature dependent Material properties	-	Species involved in combustion of H <sub>2</sub> & CH <sub>4</sub> (Thermodynamic & Transport)

The rest of this chapter is organized as follows: In § 2.1, a brief description of the original FLASH code and its capabilities is presented. In § 2.2, we describe in detail the modifications we have made to FLASH that enable reactive flow computations, including H<sub>2</sub>-Air chemistry described by three distinct mechanisms, CH<sub>4</sub>-Air chemistry, a comprehensive expansion of the materials database to include temperature-dependent transport properties, an expansion of the EOS suite to include temperature-dependent

adiabatic indices for multicomponent mixtures, and extension of the implicit diffusion solver to handle viscous and mass diffusion.

## 2.1 FLASH Code Description

FLASH was developed by the FLASH center for computational sciences at the University of Chicago to study astrophysical flow problems, and is an open-source, multi-physics simulation software. FLASH is highly parallel, designed for high-performance CFD applications and uses the Message Passing Interface (MPI) protocol for efficient inter-processor communication.

FLASH has a directory structure organization with component groups called ‘units’, which are organized according to their functionality. Adaptive Mesh Refinement (AMR) is implemented through PARAMESH [60], and is dynamically achieved by conditioning the mesh refinement on second order derivatives of the condition variables. In the following sections, we introduce some of the existing units in FLASH, relevant to compressible flow simulations. These units are Hydro, EOS, Burn and Diffuse. For a detailed description of the architecture of FLASH and the numerical methods therein, we refer the reader to [61].

### 2.1.1 Hydro Unit

The Hydro unit in FLASH solves the compressible Euler equations (2.1) – (2.3), written in conservative form [61]:

$$\frac{d\rho}{dt} + \nabla \cdot (\rho V) = 0, \quad (2.1)$$

$$\frac{d\rho V}{dt} + \nabla \cdot (\rho V V) + \nabla P = \rho g, \quad (2.2)$$

$$\frac{d\rho E}{dt} + \nabla \cdot [(\rho E + P)V] = \rho V \cdot g \quad (2.3)$$

where  $g$ ,  $\rho$ ,  $V$ ,  $P$  and  $E$  are the gravitational acceleration, density, velocity, pressure and the total energy per unit mass, respectively. The internal energy ( $e$ ) is obtained separately from equation (2.4),

$$\frac{d\rho e}{dt} + \nabla \cdot [(\rho e + P)V] - V \cdot \nabla P = 0. \quad (2.4)$$

Finally, pressure is updated using an ideal gas equation of state (EOS) described in § 2.1.2. In the case of a multi-species simulation, an advection equation for each species ' $i$ ' in the system is solved,

$$\frac{\partial \rho Y_i}{\partial t} + \nabla \cdot (\rho Y_i V) = 0 \quad (2.5)$$

where  $Y_i$  is the mass fraction of the  $i^{\text{th}}$  species.

To solve the Euler equations, FLASH is equipped with both a directionally split and unsplit algorithm for two types of meshes, a uniform grid and an adaptively refined grid in Cartesian, cylindrical, spherical and polar coordinates. The default numerical method used in FLASH is the directionally split Piecewise Parabolic Method (PPM[56]), an extension to second order of the first order Godunov [62] method.

### 2.1.2 EOS Unit

The equation of state (EOS) unit calculates the thermodynamic properties of an ideal, *gamma-law* fluid. The gamma-law EOS is applicable to a single fluid with a constant adiabatic index ( $\gamma$ ), using equations (2.6) – (2.8) to calculate the thermodynamic properties:

$$P = (\gamma - 1)\rho e, \quad (2.6)$$

$$P = \frac{N_a k \rho T}{A}, \quad (2.7)$$

$$e = \frac{N_a k T}{A(\gamma - 1)}, \quad (2.8)$$

where  $N_a$ ,  $k$ ,  $A$  and  $T$  are the Avogadro number, Boltzmann constant, atomic mass of the fluid and temperature. In the case of a multi-component system containing  $N$  species, the average atomic mass ( $A_{avg}$ ) and adiabatic index ( $\gamma_{avg}$ ) of the fluid mixture are calculated using equations (2.9) and (2.10), respectively:

$$\frac{1}{A_{avg}} = \sum_i \frac{Y_i}{A_i}, \quad (2.9)$$

$$\gamma_{avg} = 1 + \left( A_{avg} \sum_i^N A_i \frac{Y_i}{\gamma_i - 1} \right)^{-1}. \quad (2.10)$$

In § 2.2.1, we describe the extension of this module to handle temperature-dependent specific heats, necessary for modeling combustion flows.

### 2.1.3 Burn Module

The *Burn module* in FLASH was designed to solve nuclear reaction networks, where the evolution of an individual species is governed by [61],

$$\frac{dX_i}{dt} = R_i. \quad (2.11)$$

Here,  $X_i$  and  $R_i$  are the molar fraction and the net rate of change of molar fraction of  $i^{th}$  species due to all the reactions in the reaction network. For multiple species, equation (2.11) represents a set of stiff, coupled ordinary differential equations, which are solved using Kaps-Rentrop (Rosenbrok)[63] or Bader-Deuflhard[64] time integration methods, supplemented by an MA28[65] linear algebra package. We have modified this module to solve a system of stiff equations arising from typical chemical reaction mechanisms (§ 2.2.4).

### 2.1.4 Diffusion Unit

Diffusion effects in FLASH are incorporated through the inclusion of either an explicit flux-based solver or a general implicit diffusion equation solver. The flux-based

diffusion solver is an indirect method to account for diffusion effects, that does not operate on the primary variables, instead updating the fluxes due to diffusion of heat, mass and momentum [61]. In contrast, the implicit solver computes the solution to the general diffusion equation from which the primary variables are directly obtained, so that the solution does not require inputs from other units. The diffusion of variable  $f$  governed by equation (2.12) can be solved with an implicit time-stepping in directionally split or unsplit mode,

$$A \frac{\partial f}{\partial t} + C = \nabla \cdot B \nabla f + D, \quad (2.12)$$

where  $A$ ,  $B$ ,  $C$  and  $D$  can be parameters with spatial variations. The current implementation of the implicit solver in FLASH solves for thermal diffusion, which we have extended in § 2.2.2 to handle mass and momentum diffusive transport.

## 2.2 Development of Chemical Reaction Solvers and Auxiliary Modules

In this section, we describe the additional capabilities we have developed to enable combustion flow simulations using FLASH. These capabilities include a temperature-dependent, multi-species equation of state (EOS) (§ 2.2.1), extension of the implicit solver to handle mass and viscous diffusion (§ 2.2.2), modifications to the Burn module to handle  $H_2$ -Air and  $CH_4$ -Air reaction mechanisms (§ 2.2.4), and an expansion of the materials database (§ 2.2.3) (temperature-dependent transport and thermodynamic properties) to include species commonly involved in the reaction mechanisms.

### 2.2.1 Temperature-dependent Equation of State

The equation of state (EOS) module described in § 2.1.2 was expanded to include multiple species with temperature-dependent properties to enable FLASH to solve chemically reacting flows with heat addition. The extended EOS can be applied to

temperatures ranging from 298K - 5000K, and requires 10 coefficients for each species in the mixture to calculate thermodynamic properties. The existing EOS unit in FLASH [61] can be invoked in three modes according to the input variable pairs supplied in each case viz., *Density-Temperature* ( $\rho, T$ ), *Density-Pressure* ( $\rho, P$ ), and *Density-Internal Energy* ( $\rho, e$ ).

Density-Temperature ( $\rho, T$ ) mode:

In this mode, the EOS routine first calculates the specific heat at constant pressure ( $Cp_i$ ) for each species  $i$  in the mixture according to [66],

$$\frac{Cp_i}{R} = a_1 + a_2 T + a_3 T^2 + a_4 T^3 + a_5 T^4, \quad T \geq 1000K, \quad (2.13)$$

$$\frac{Cp_i}{R} = a_8 + a_9 T + a_{10} T^2 + a_{11} T^3 + a_{12} T^4, \quad T < 1000K, \quad (2.14)$$

where  $R$  is the universal gas constant and  $a_1 - a_5$  and  $a_8 - a_{12}$  are thermodynamic polynomial coefficients of the  $i^{th}$  species in the mixture for  $T \geq 1000$  K and  $T < 1000$  K respectively. Note that coefficients  $a_6, a_7, a_{13}$  and  $a_{14}$  are used to evaluate additional thermodynamic properties by other modules (e.g. Burn) and will be discussed in § 2.2.4. The adiabatic index  $\gamma_i$  at temperature  $T$  corresponding to each species is then computed using

$$\gamma_i = \frac{Cp_i}{Cp_i - R}, \quad (2.15)$$

while the mixture adiabatic index  $\gamma_{avg}$  is obtained from

$$\gamma_{avg} = 1 + \left( A_{avg} \sum_i^N A_i \frac{\gamma_i}{\gamma_i - 1} \right)^{-1}. \quad (2.16)$$

Finally, the pressure ( $P$ ) and internal energy ( $e$ ) are then computed using:

$$P = \frac{R \rho T}{A_{avg}}, \quad (2.17)$$

$$e = \frac{RT}{A_{avg}(\gamma_{avg}-1)}. \quad (2.18)$$

Density–Pressure ( $\rho$ ,  $P$ ) mode:

When ( $\rho$ ,  $P$ ) are supplied as input variables, the temperature of the mixture is first computed using equation (2.17), followed by the mixture adiabatic index obtained from equations (2.13) – (2.16), and internal energy is finally computed from equation (2.18).

Density–Internal Energy ( $\rho$ ,  $e$ ) mode:

Here, ( $\rho$ ,  $e$ ) are provided as inputs, while equation (2.18) is solved iteratively to calculate temperature using the Newton–Raphson root finding algorithm. The solver requires an initial temperature guess, maximum number of iterations, and a tolerance for the absolute allowable error, which are specified in an input file with default values of 1001.0 K, 50 and 1.0e-8 K, respectively. Pressure is then calculated using equation (2.17). We found that the temperature-dependent multi-species EOS suffered no significant degradation in performance compared to the single-species unit, an important consideration in a reactive flow simulation where the EOS unit could be called multiple times over a single Hydro timestep.

The verification of multi-species, EOS unit by comparison with data compiled by NIST [67] is reported in the Appendix.

### 2.2.2 Implicit Mass and Viscous Diffusion Equation Solvers

Diffusion is critical to reactive flows (laminar or turbulent), since it determines abundances of reactants across a flame front, and thus the ultimate reaction rate. However, with temperature variations from heat addition, the transport properties governing the diffusive process may also change significantly, and must be modeled accurately. In this section, we discuss specific modifications to FLASH and the diffusion solvers therein that

enable accurate description of temperature-dependent diffusive transport associated with heat, mass and momentum. Note that FLASH is equipped with a separate ‘flux-based’ diffusion solver (§ 2.1.4) that updates the diffusive fluxes in each direction. In addition, an implicit solver for a general diffusion equation is available in FLASH, and described in § 2.1.4. Currently, the implicit solver is used to solve the thermal diffusion equation (§ 2.1.4). We have extended the use of this solver to compute solutions to the mass and viscous diffusion equations, using an operator splitting approach. Equation (2.12) is the general form of the diffusion equation solved by the implicit solver in FLASH. For example, mass diffusion of species  $i$  may then be written as

$$\rho \frac{\partial Y_i}{\partial t} = \nabla \cdot (\rho D_i \nabla Y_i), \quad (2.19)$$

so that  $Y_i$  represents the mass fraction of species  $i$ ,  $\rho$  is the mixture density and  $D_i$  is the species diffusivity, computed from equations described in § 2.2.3. Thus, for the mass diffusion equation an implicit solver is used, during which FLASH freezes the density field in equation (2.19). Similarly, viscous diffusion effects are solved by rewriting equation (2.12)

$$\rho \frac{\partial v}{\partial t} = \nabla \cdot (\mu \nabla v), \quad (2.20)$$

where  $\mu$  is the temperature-dependent dynamic viscosity of the mixture. Typically, the temperature-dependent viscosity and mass-diffusion coefficients of species  $i$  are specified, while the thermal conductivity is constrained through a constant Lewis number ( $Le_i$ ) assumption. The implementation of these solution methods was verified (reported in the Appendix) by comparing the axial velocity decay of a non-reacting, axisymmetric laminar jet with the analytical solution from [68] and the DNS results of [69] as well as the temporal decay of a potential vortex with analytical solutions from [70].

### 2.2.3 Temperature-dependent Material Properties Database

The material properties database in FLASH was expanded to accommodate temperature-dependent thermodynamic or transport properties of a single- or multi-species system. In reacting flows with significant temperature changes, the material and thermodynamic properties of species can be strong functions of temperature. Since FLASH is organized in to distinct modules, these properties are calculated by individual units in the course of a reactive flow computation. Thus, a central database of coefficients accessible to all units is required to calculate these properties at any given temperature, and has been implemented.

At initialization, a multi-species unit [61] stores several attributes of constituent species required in the course of a simulation. These include the names of the species, the molecular weights, the enthalpies of formation, the temperature-dependent adiabatic indices, the curve-fit polynomial coefficients for thermodynamic [66] and transport [71] properties.

The EOS unit described in § 2.2.1 calculates the thermodynamic properties, while the transport properties (conductivity, viscosity and mass diffusion coefficients) are calculated in separate *material properties* units described below.

Viscosity:

The pure species dynamic viscosity ( $\mu_i$ ) in Poise is calculated using a curve fit polynomial [71] with 8 coefficients ( $b_1 - b_8$ ) for each species. The coefficients are applied based on the temperature, and according to

$$\ln \mu_i = b_1 \ln T + \frac{b_2}{T} + \frac{b_3}{T^2} + b_4, \quad T < 1000\text{K}, \quad (2.21)$$

$$\ln \mu_i = b_5 \ln T + \frac{b_6}{T} + \frac{b_7}{T^2} + b_8, \quad T \geq 1000\text{K}. \quad (2.22)$$

The coefficients required in these calculations are accessed from the central database described above. The multi-species mixture viscosity ( $\mu_{mix}$ ) can then be calculated by a combination averaging formula [72] such as equation (2.23)

$$\mu_{mix} = \frac{1}{2} \left[ \sum_{i=1}^N \mu_i X_i + \left( \sum_{i=1}^N \frac{X_i}{\mu_i} \right)^{-1} \right], \quad (2.23)$$

or by using a semi-empirical formula [73]

$$\mu_{mix} = \sum_{i=1}^N \frac{\mu_i X_i}{\sum_{j=1}^N X_j \Phi_{ij}} \text{ and } \Phi_{ij} = \frac{1}{\sqrt{8}} \left( 1 + \frac{A_i}{A_j} \right)^{-\frac{1}{2}} \left( 1 + \left( \frac{\mu_i}{\mu_j} \right)^{\frac{1}{2}} \left( \frac{A_i}{A_j} \right)^{\frac{1}{4}} \right)^2. \quad (2.24)$$

Thermal Conductivity:

The pure species conductivity ( $\lambda_i$ ) in W/cm-K is computed from a curve fit polynomial [71] with coefficients ( $c_1 - c_8$ ) for each species given by,

$$\ln \lambda_i = c_1 \ln T + \frac{c_2}{T} + \frac{c_3}{T^2} + c_4, \quad T < 1000\text{K}, \quad (2.25)$$

$$\ln \lambda_i = c_5 \ln T + \frac{c_6}{T} + \frac{c_7}{T^2} + c_8, \quad T \geq 1000\text{K}. \quad (2.26)$$

The multi-species mixture conductivity ( $\lambda_{mix}$ ) is then obtained from the combination averaging formula [72]

$$\lambda_{mix} = \frac{1}{2} \left[ \sum_{i=1}^N \lambda_i X_i + \left( \sum_{i=1}^N \frac{X_i}{\lambda_i} \right)^{-1} \right]. \quad (2.27)$$

Alternately, the mixture conductivity could be obtained from a constant Lewis number assumption:

$$\lambda_{mix} = \rho Le_i D_{im} c_p. \quad (2.28)$$

Here,  $Le_i$  and  $D_{im}$  are the Lewis number and mass diffusion coefficient of the  $i^{th}$  species in a mixture containing  $N$  species. Note that when  $\lambda_{mix}$  is obtained using equation (2.28), the mass diffusion coefficients  $D_{im}$  have been calculated independently from equation (2.30) below.

Mass diffusion:

For a given Lewis number, the mass diffusion coefficient of the  $i^{th}$  species in the mixture ( $D_{im}$ ) can be calculated using,

$$D_{im} = \frac{\lambda_{mix}}{\rho Le_i c_p}, \quad (2.29)$$

where  $\lambda_{mix}$  is independently available from equations (2.25 – 2.27). We have also implemented the option to calculate the mass diffusion coefficient independently without making assumptions on the Lewis number. This is achieved by assuming the mass diffusion coefficient  $D_{im}$  of each species  $i$  in the mixture ( $m$ ) to be equal to that of a binary gas system  $A-B$  ( $D_{AB}$ ), where  $A$  and  $B$  can be any major species pair. Then, the binary diffusion coefficient  $D_{AB}$  of the system is calculated using the Chapman and Enskog solution [74] to the Boltzmann equation,

$$D_{AB} = \frac{0.00266 T^{1.5}}{P M_{AB}^{0.5} \sigma_{AB}^2 \Omega_D}, \quad (2.30a)$$

$$M_{AB} = 2 \left[ \frac{1}{A_A} + \frac{1}{A_B} \right]^{-1}, \quad (2.30b)$$

$$\sigma_{AB} = (\sigma_A + \sigma_B), \quad (2.30c)$$

where  $\sigma_{AB}$  is the characteristic length of the intermolecular forces,  $\Omega_D$  is the diffusion collision integral,  $\sigma_A$  and  $\sigma_B$  are the Lennard-Jones lengths of species  $A$  and  $B$ , and  $A_A$  and  $A_B$  are molecular weights of species  $A$  and  $B$ . Our current implementation in FLASH includes the following binary gas systems:  $H_2 - O_2$ ,  $N_2 - O_2$  or  $CH_4 - O_2$ .

#### 2.2.4 Burn Module

We describe the implementation of  $H_2$ -Air and  $CH_4$ -Air reaction kinetics to the existing *Burn* module in FLASH. A general reaction mechanism involving  $N$  species and  $m$  reactions can be represented as:

$$\sum_{k=1}^N v_{kj}' M_k \Leftrightarrow \sum_{k=1}^N v_{kj}'' M_k, \quad (2.31)$$

where  $v_{kj}'$  and  $v_{kj}''$  are the stoichiometric molar coefficients of species labeled  $M_k$  in the  $j^{\text{th}}$  reversible reaction. Thus, the net rate ( $q_k$ ) of formation or consumption of the  $k^{\text{th}}$  species is the sum of contributions from all reactions in the reaction involving that species, and written as

$$q_k = \sum_{j=1}^m q_{kj}, \quad (2.32a)$$

where

$$q_{kj} = (v_{kj}'' - v_{kj}') \left( k_{fj} \prod_{k=1}^N C_{M_k}^{v_{kj}'} - k_{bj} \prod_{k=1}^N C_{M_k}^{v_{kj}''} \right). \quad (2.32b)$$

In equation (2.32b),  $q_{kj}$  is the rate of formation (or consumption) of the  $k^{\text{th}}$  species in reaction  $j$ ,  $k_{fj}$  and  $k_{bj}$  are the corresponding forward and backward reaction rates, while  $C_{M_k}$  is the concentration of the  $k^{\text{th}}$  species. For most reaction mechanisms, the forward reaction rates are given in the form of an Arrhenius equation,

$$k_{fj} = AT^\alpha e^{\left(\frac{-E_a}{RT}\right)}, \quad (2.33)$$

where  $\alpha$ ,  $A$  and  $E_a$  are the temperature index, pre-exponential factor and activation energy respectively. To compute the backward reaction rates, the concentration-based reaction equilibrium constant ( $K_c$ ) is first evaluated from

$$K_c = \left(\frac{RT}{P}\right)^{-\Delta v} e^{\left(\frac{\Delta G_T}{RT}\right)}. \quad (2.34)$$

Here,  $\Delta v$  is the change in mole number (between products and reactants), while  $\Delta G_T$  represents the corresponding change in the Gibbs free energy. The Gibbs free energy for each species is calculated according to [75]

$$\frac{G_T}{RT} = a_1(1 - \ln T) - \frac{a_2 T}{2} - \frac{a_3 T^2}{6} - \frac{a_4 T^3}{12} - \frac{a_5 T^4}{20} + \frac{a_6}{T} - a_7, T \geq 1000\text{K} \quad (2.35a)$$

$$\frac{G_T}{RT} = a_8(1 - \ln T) - \frac{a_9 T}{2} - \frac{a_{10} T^2}{6} - \frac{a_{11} T^3}{12} - \frac{a_{12} T^4}{20} + \frac{a_{13}}{T} - a_{14}, \quad T < 1000\text{K} \quad (2.35b)$$

where  $a_1 - a_{14}$  are the polynomial coefficients [66] from a curve fit of the thermodynamic data for a given species. From the equilibrium constant  $K_c$ , the backward reaction rates can be inferred:

$$k_{bj} = \frac{k_{fj}}{K_c}. \quad (2.36)$$

From equations (2.32), it is clear that a reaction mechanism involving  $N$  species could be formulated as a system of  $N$  coupled ordinary differential equations. The resulting ODE system is stiff, owing to large variations (several orders of magnitude) in the reaction rates and the corresponding eigenvalues. We use two implicit ODE integrators already available in FLASH viz., the Bader-Deuflhard [64] and Kaps-Rentrop [63] schemes (along with linear algebra package MA28[65]) to solve the stiff system of equations represented by the general equation (2.32a). For both methods, the energy generated ( $e_g$ ) during a time advancement  $\Delta t$  is calculated using

$$e_g = \sum_i^N \frac{h_{f_i}}{A_i} (Y_{i_t} - Y_{i_{t+\Delta t}}), \quad (2.37)$$

where  $h_{f_i}$  is the heat of formation,  $Y_{i_t}$  and  $Y_{i_{t+\Delta t}}$  are the mass fractions of the  $i^{\text{th}}$  species before and after the time advancement respectively.

We have implemented three reaction mechanisms for  $H_2$ -Air combustion and one for  $CH_4$ -Air combustion in FLASH. The 9-species, 19 reaction  $H_2$ -Air mechanism of Billet [76] is reduced from the detailed acetylene combustion mechanism of [77], and was used [76] to study the interaction of acoustic waves with circular and spherical hydrogen diffusion flames and reactive shock-bubble interactions. We have also implemented the 9-species, 19-step reversible reaction mechanism of Mueller et al. [78] as adapted by [79] to

simulate premixed  $H_2$ -Air vortex rings. The third-body efficiencies ( $M$ ) for all the reactions in this mechanism were taken from [78]. Both mechanisms exclude  $NO_x$  chemistry important for industrial high-temperature burners. Finally, we have also included the 11-species, 20-step reversible reaction mechanism of Katta and Roquemore [80], which was originally used to study the tip opening phenomena in premixed  $H_2$ -Air Bunsen burner flames. The calculated burning velocities [80] from this mechanism were in excellent agreement with [81] for equivalence ratios less than 2.5, while higher equivalence ratios resulted in underpredicted values of the burning velocities. Note that in our implementation of this mechanism, the third body efficiency ( $M$ ) for all the species was assumed to be unity.

We have reported the results from validation of the above capabilities through comparison with analytical solutions, and published numerical and experimental data in [82]. The validation cases included comparison of temporal evolution of species and temperature in a well stirred reactor, comparison of adiabatic flame temperature data, advection of reacting and non-reacting 1D fronts, 2D laminar premixed methane–air flame in a Bunsen burner configuration, shock-driven combustion of an initially circular hydrogen bubble, and a reacting Richtmyer–Meshkov instability not studied previously. Additional verifications for the modified code not presented in [82] are presented in the Appendix.

## CHAPTER 3: PROBLEM FORMULATION AND UNPERTURBED RAYLEIGH-TAYLOR FLAMES

In this chapter we investigate the dynamics of non-premixed Rayleigh-Taylor flames. We first discuss the dynamics of a 1D reacting front (§3.2) to explore the effect of flame formation in the absence of hydrodynamic instability (unperturbed). This is followed by an examination of interaction between RT instability and flame through 2D single-mode and 3D multimode (turbulent) simulations for high (in chapter 4) and low (chapter 5) A flames.

### 3.1 Problem Formulation and Numerical Methods

We consider the Rayleigh-Taylor instability of a perturbed interface schematically depicted in Figure 3.1(a), where the lighter fuel ( $H_2 + N_2$ ) in region I supports the heavier Air in region II against an imposed background acceleration ( $g$ ). The fluids are initially in thermal equilibrium, with a uniform temperature  $T_0 = T_f = T_a = 1000K$ , (subscripts a/f denote air/fuel) that is chosen to ensure the mixture at the fuel-air interface will auto-ignite to form the flame surface. The density ratio is parametrized by the Atwood number  $(A_{f-a} = \frac{\rho_a - \rho_f}{\rho_a + \rho_f})$ , and can be directly and systematically varied in the simulations discussed here by changing the level of  $N_2$  dilution in the fuel stream. Pressure at the interface ( $x = x_i$ ) is initialized to  $P_0 = 1 atm$ , and varies away from the interface (figure 3.1b) in a manner that satisfies the hydrostatic thermal equilibrium condition:

$$P(x) = P_0 e^{\left\{ \frac{g(x-x_i)}{R_s T_0} \right\}}. \quad (3.1)$$

In eq. (3.1),  $R_s$  denotes the specific gas constant. We initialize density (and other thermodynamic variables) from (P,T) through an ideal gas equation of state. Finally, we impose hydrostatic outflow conditions on y-z boundaries, and periodic conditions on x-z and x-y boundaries. FLASH uses pseudo-cells (guard cells) outside the computational domain to enforce these boundary conditions. For instance, the hydrostatic equilibrium condition is enforced at the outlet boundaries according to [83] by first assuming constant T and species concentrations in the guard cells and then integrating,

$$\frac{dP}{dx} = \rho g, \quad (3.2)$$

for an assumed second order  $\rho(x)$  profile [83] constructed from cell averaged values of  $\rho$ . The resulting equation is then iteratively solved by adjusting the density in the guard cells through the equation of state to calculate  $P(\rho, T)$ . For additional details, we direct the readers to [83].

We track the progress of the single mode RT in time as the locus of extrema of the mixture fraction (Z)[84,85],

$$Z \equiv \frac{\left(\frac{Z_H}{2W_H} + \frac{Z_{O_a} - Z_O}{W_O}\right)}{\left(\frac{Z_{H_f}}{2W_H} + \frac{Z_{O_a}}{W_O}\right)}, \quad (3.3)$$

$$Z_H = W_H \left( \frac{2Y_{H_2}}{W_{H_2}} + \frac{Y_H}{W_H} + \frac{2Y_{H_2O}}{W_{H_2O}} + \frac{Y_{OH}}{W_{OH}} + \frac{Y_{HO_2}}{W_{HO_2}} + \frac{2Y_{H_2O_2}}{W_{H_2O_2}} \right), \quad (3.4)$$

$$Z_H = W_O \left( \frac{2Y_{O_2}}{W_{O_2}} + \frac{Y_O}{W_O} + \frac{Y_{H_2O}}{W_{H_2O}} + \frac{Y_{OH}}{W_{OH}} + \frac{2Y_{HO_2}}{W_{HO_2}} + \frac{2Y_{H_2O_2}}{W_{H_2O_2}} \right). \quad (3.5)$$

In the above equation,  $Z_i$ ,  $W_i$  and  $Y_i$  are the mixture fraction, molecular weight and mass fraction of the  $i^{th}$  species, while  $Z_{O_a}$  and  $Z_{H_f}$  are the atomic mixture fraction of O and H evaluated in the air and fuel streams respectively. Note that  $Z$  varies smoothly (and monotonically) across the burning interface (unlike density or individual species mass

fractions) making it a reliable and convenient metric for comparing the reacting interface with its non-reacting counterpart.

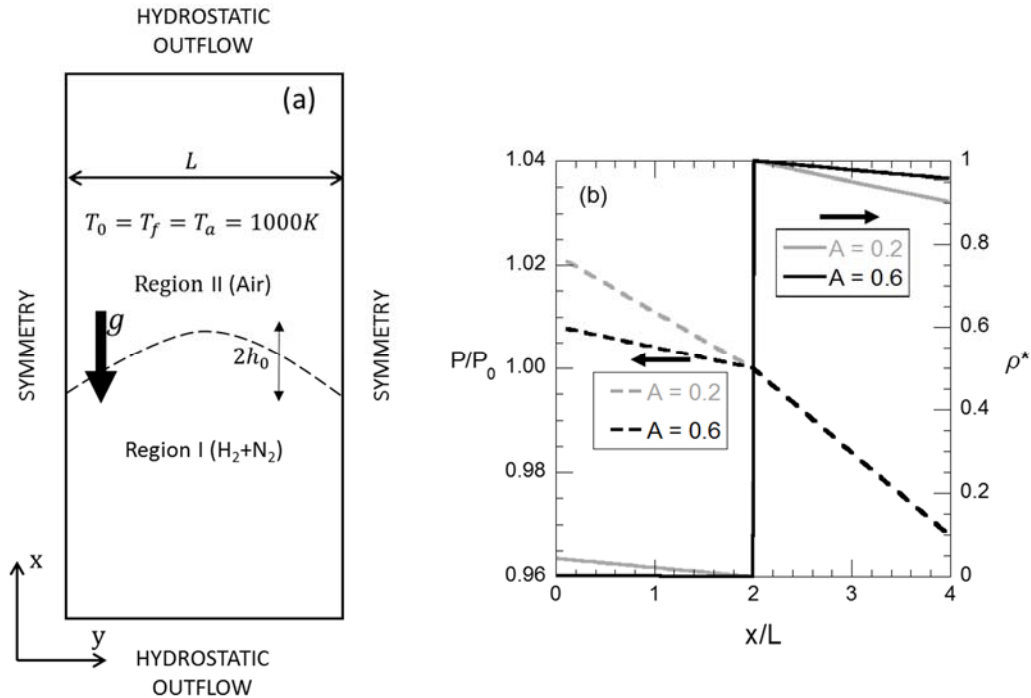


FIGURE 3.1: (a) Schematic of the proposed problem setup to investigate reactive Rayleigh-Taylor Instability and (b) scaled density ( $\rho^* = (\rho - \rho_f) / (\rho_a - \rho_f)$ ) (solid lines) and pressure ( $P/P_0$ ) (dashed lines) across an unperturbed interface  $h_0 = 0$  at  $A=0.2$  (gray) and  $A=0.6$  (black). 1D simulations employed a background acceleration of  $g = 0.6 \times 10^4 g_0$ , where  $g_0 = -981 \text{ cm/s}^2$ .

The reacting and inert simulations performed as part of this work may be classified in to three broad categories: (i) 1D simulations with an unperturbed interface, (ii) 2D simulations with imposed single-mode perturbations and (iii) 3D simulations with imposed multimode perturbations that eventually degrade to a turbulent state. Simulations in each category were repeated for different values of  $A$ , and are catalogued in table 3.1. The 1D simulations were initialized with  $x$ -profiles of ( $Z$  and  $P$ ) at a constant temperature specified according to eqs. (3.1) – (3.5) while the rest of the thermodynamic quantities ( $\rho$ ,  $E$ , etc) were calculated consistently using a temperature-dependent, multispecies equation of state.

The single-mode simulations were initialized with a similar specification of the state variables, but the material interface between the fuel mixture and air supported a perturbation waveform,  $\cos(ky)$  with a wavenumber ( $k = \frac{2\pi}{\lambda}$ ). The interface thickness is finite and specified according to [86],

$$s = \frac{(x_i + h_0 \cos(ky) + \delta - x)}{\delta} \quad (3.6)$$

Then, the mixture fraction profile across the interface is given by

$$Z(x) = \begin{cases} 0 & s \leq 0 \\ 1 & s \geq 1 \\ 1 - e^{|s|^\varepsilon \ln(\alpha)} & 0 < s < 1 \end{cases} \quad (3.7)$$

where  $\varepsilon$ ,  $\delta$ ,  $x_i$ , and  $h_0$  represent the machine zero (approximated to  $10^{-30}$ ), the initial interface thickness ( $\delta \approx 3\Delta x$ ), location of the interface and the perturbation amplitude respectively. The single-mode simulations were performed with wavelengths  $\lambda = 0.3, 0.5$  and  $1.0$  cm, while the acceleration driving the flow was varied from  $6,000g_0 - 48,000g_0$ , relevant to realistic UCC operating conditions [12,13]. The multimode simulations (case 26-30) were initialized by imposing a narrowband spectrum of waves at the material interface, so that the perturbation amplitudes satisfy [3]

$$h(y, z, t = 0) = \sum_{k_y, k_z} \begin{bmatrix} a_k \cos(k_y y) \cos(k_z z) + \\ b_k \sin(k_y y) \cos(k_z z) + \\ c_k \cos(k_y y) \sin(k_z z) + \\ d_k \sin(k_y y) \sin(k_z z) \end{bmatrix} \quad (3.8)$$

When viscous effects are accompanied by diffusive broadening of the interface, a perturbed interface grows exponentially in the linear stage with a growth rate exponent [87],

$$n = \sqrt{\left(\frac{Agk}{\psi}\right) + \nu^2 k^4 - (\nu + D)k^2} \quad (3.9)$$

where  $\nu$  and  $D$  are the kinematic viscosity and mass diffusivity respectively. The growth reduction factor ( $\psi$ ) in the above equation varies with time for a wide range of Atwood numbers such that,  $\psi(t) \approx \frac{2k\sqrt{Dt}}{1.2} + 1$  [87]. The fastest growing wavelength ( $\lambda_{max}$ ) to emerge from linear growth of the initial perturbation wavepacket is determined by numerically solving eq. (3.9) with the condition  $\frac{dn}{dk} = 0$  at any given instance in time. Using  $L = 8 \text{ cm}$  and  $g = 6 \times 10^3 g_0$  for cases (26) – (30), we estimate  $\lambda_{max}$  to be  $\sim 0.3 \text{ cm}$  and  $0.5 \text{ cm}$  at  $t = 0$  and at ignition respectively.

We briefly demonstrate our methodology to ensure our turbulent reacting and non-reacting RT simulations were adequately resolved. For the reacting RT, mesh resolution is dictated by the three distinct criteria: the resolution of the Kolmogorov scale, resolution of the flame thickness and satisfaction of a cell-based Grashof number criteria to ensure suppression of spurious grid-based modes driven by the buoyancy of the flow. We address each of these requirements in detail. During the turbulent self-similar growth, RT interfaces subjected to a constant acceleration evolve as [1-3,30,31,88]  $h \sim \alpha A g t^2$ . Accordingly, the Kolmogorov scales ( $\eta$ ) may be estimated from the flow Reynolds number ( $Re \equiv \frac{h\dot{h}}{\nu}$ ) as follows,

$$\eta = h Re^{-\frac{3}{4}} = h \left( \frac{h\dot{h}}{\nu} \right)^{-\frac{3}{4}} = \frac{\left( \frac{\nu}{2} \right)^{0.75} t^{-0.25}}{\sqrt{\alpha A g}}, \quad (3.10)$$

and is thus a weak function of time. Thus, scale separation in self-similar RT implies a Kolmogorov scale nearly independent of time, a result that is fortuitous to the design of numerical simulations since the smallest flow scales dictate the grid resolution. The multimode simulations employed a uniform grid with 256 zones/L, so that the mesh resolution satisfied  $\Delta x \sim \eta$  where  $\eta$  is the Kolmogorov length scale, sufficient to resolve

[89,90] the late time turbulent flow field. A second concern, particular to simulations of RT flows, is the growth of grid-generated, spurious modes that can nevertheless be driven by the buoyant forces in the flow. The criterion for the growth of such numerical modes may be given in terms of a grid Grashof number[1],

$$Gr_{\Delta x} = \frac{g\Delta\rho V}{\rho\nu^2} = \frac{2Ag\Delta x^3}{\nu^2}. \quad (3.11)$$

where  $\nu$  is the mixture viscosity, while  $\Delta x$  is the grid size. For numerical modes to be stabilized by viscous diffusion,  $\Delta x$  must be small enough so that  $Gr_{\Delta x} < 1$ . Note that the above equation does not account for suppression of perturbation growth by mass diffusion. In the presence of mass diffusion, eq. 3.9 may be used to estimate a cut-off wavelength ( $\lambda_{min}$ ), such that perturbations smaller than  $\lambda_{min}$  show no growth ( $n \leq 0$  due to diffusion). The cut-off wavelength for cases 26-30 was found to be  $\sim 0.11$  cm. The grid resolution employed for cases 26-30  $\Delta x \approx \lambda_{min}/4$  ensures suppression of spurious grid-based modes by viscous and mass diffusion. Thus the condition,  $Gr_{\Delta x} < 1$  for resolution requirement may be relaxed under the influence of mass diffusion such that  $Gr_{\Delta x} = \frac{2Ag\Delta x^3}{(\nu+D)^2} \sim 1$ , satisfied by our simulations (cases 26-30).

In addition to the flow scales, the flame/reaction zone thickness also dictates the mesh resolution used in the simulations. The flame thickness ( $L_f$ ) is given by [84],

$$L_f \sim \frac{Z_R}{\Delta Z_H}, \quad (3.12)$$

where  $Z_R$  is the peak combustible range of atomic H mixture fraction ( $Z_H$ ) and  $\Delta Z_H$  is the corresponding gradient across the mixing width. For atmospheric  $H_2$ -Air flames,  $Z_R \approx 0.015$  [84]. For an interface initially at rest, the flame thickness is diffusion controlled, and

may be estimated as  $L_f \sim \frac{Z_R}{Z_{Hf}} L_d \sim \frac{Z_R}{Z_{Hf}} (8\sqrt{D_{fl}t})$  where  $L_d$  is the interface thickness,  $D_{fl}$  is

the mass diffusion coefficient at the flame site ( $Z = Z_{st}$ ) and  $Z_{H_f}$  is the atomic H mixture fraction in fuel stream. The resolution employed in this work for cases 26-30 (multimode perturbations) is estimated to be  $\Delta x \approx L_f/5$  at ignition sufficient to resolve autoignition of fuel-air mixture and subsequent flame dynamics (following ignition  $L_f$  increases with time).

TABLE 3.1: Summary of simulation performed to characterize RT flames.

Case	Perturbation	$\lambda$ (cm)	$h_0$ (cm)	React	$A_{f-a}$	$g$	Dimension	Resolution		
1-5	None	-	-	Yes	0.2, 0.4, 0.6, 0.7, 0.87	$6e3g_0$	1D (2cm)	256		
6				Yes	0.2	$-6e3g_0$				
7	Single Mode	1.0	$\frac{0.015}{k}$	Yes	0.2	$6e3g_0$	2D ( $6\lambda \times \lambda$ )	256/ $\lambda$		
8				Yes	0.2	$1e4g_0$				
9				Yes	0.2	$2e4g_0$				
10-11				Yes	0.2, 0.6	$4e4g_0$				
12		0.5	$\frac{0.05}{k}$	No	0.6	$6e3g_0$				
13				Yes	0.6	$6e3g_0$				
14				No	0.2	$6e3g_0$				
15				Yes	0.2	$6e3g_0$				
16				Yes	0.2	$-6e3g_0$				
17-19				Yes	0.4, 0.7, 0.87	$6e3g_0$				
20				Yes	0.2	$12e3g_0$				
21				Yes	0.2	$18e3g_0$				
22				Yes	0.2	$24e3g_0$				
23				0.3	$\frac{0.1}{k}$	Yes			0.2	$18e3g_0$
24						Yes			0.2	$24e3g_0$
25						Yes			0.2	$30e3g_0$
26				Multimode (L=8cm)	$\frac{L}{32}$ to $\frac{L}{16}$	$\frac{h_{rms}}{L}$ $\frac{12}{1e4}$			No	0.6
27	Yes	0.6	$6e3g_0$							
28	No	0.2	$6e3g_0$							
29	Yes	0.2	$6e3g_0$							
30	Yes	0.2	$-6e3g_0$							

The simulations were performed using the modified version of FLASH[55,82], described in chapter 2. The ‘Hydro’ unit is used to solve the Euler equations on a finite volume mesh, using the Piecewise Parabolic Method [56]. Diffusive transport of mass, momentum and heat are implemented separately in an operator-split timestep, through a dedicated Diffuse unit that solves diffusion equations for species, velocities and temperature using a Crank-Nicholson scheme. Hydrogen combustion is described through a  $H_2$ -air, 19-step, 9-species detailed reaction mechanism [76]. The reaction rates are modelled through Arrhenius equations, so that the nine coupled species evolution equations were numerically integrated in time, using a variable order Bader-Deuflhard [64] method capable of handling the inherent stiffness of the ODE system. Note that each species in the reaction kinetics is represented in the simulation database with temperature-dependent thermodynamic [66] and transport properties [71]. The specific heat ( $Cp_i$ ) for each species in the reaction mechanism is modelled as a 4th order temperature polynomial requiring a total of 10 coefficients [66] (5 each for 300-1000K and 1000-5000K range). The mixture adiabatic index (equation 2.16) is then computed to evaluate the mixture thermodynamic properties using the ideal gas equation of state. Mixture transport properties are obtained either through combination averaging or constraints on the Lewis number or the Schmidt number. Thus, the dynamic mixture viscosity ( $\mu_{mix}$ ) is obtained by combination-averaging of individual species viscosities ( $\mu_i$ ) according to equation (2.23) [72,76]. Note that the species viscosity is modelled as a temperature-dependent polynomial according to [71]. Similarly, the mass diffusivity of the mixture is derived from the mixture viscosity by assuming a constant Schmidt number ( $\sim 0.75$ ) for all the species involved, an approach that has shown to be accurate [91] for the transport of major species in  $H_2$ -Air combustion. To

avoid the development of local density gradients due to the imbalance between thermal and mass fluxes that could complicate our problem definition, we define the mixture thermal conductivity by imposing a unity Lewis number condition. Finally, the computations were performed with a CFL constraint on the timestep to ensure stability.

### 3.2 Unperturbed Flames

In this section, we describe results from 1D simulations of chemically reacting, unperturbed interfaces driven by a constant acceleration field of  $\pm 6000g_0$ . The absence of perturbations at the interface allows us to isolate the flame dynamics as a function of the Atwood number, without regard to instability development. In our simulations, an initially sharp interface separating the fuel and air streams is centrally located in a 2 cm long computational domain. Diffusion across the interface produces a combustible mixture that autoignites at  $t_{ign} \approx 0.34 \text{ ms}$  and  $\approx 0.28 \text{ ms}$  for  $A = 0.2$  and  $0.6$  respectively (where  $t_{ign}$  is defined as the time to attain a 20% increase in temperature). The ignition of such a diffuse layer generates localized combustion waves [92] that impart a weak, time-dependent acceleration ( $g_c(t) \approx 0.5 \times t^{-1.2} \text{ cm}^2/\text{s}$ ) on the interface which we identify from the location of the 50% mixture fraction level. Since the applied acceleration is large, we find the effects of the combustion wave to be insignificant in comparison ( $\max(g_c(t)) \approx 0.2\%$  of applied  $g$ ). In figure 3.2, we plot the scaled density ( $\rho^* = \frac{\rho - \rho_f}{\rho_a - \rho_f}$ ), the scaled temperature ( $\frac{T}{T_0}$ ) and the mixture fraction for (a)  $A=0.2$  and (b)  $A=0.6$  at late times ( $t = 2\text{ms}$ ) when the flames have asymptotically approached their maximum temperature. Note that the peak temperatures at this time are within 15% of the equilibrium adiabatic flame temperature calculated from [93]. Across the burning interface (figs. 3.2a), the mixture fraction varies

monotonically and exhibits a symmetric profile for the flame with  $A = 0.2$  ( $Z_{st}|_{A=0.2} \approx 0.45$ ). On the contrary for  $A=0.6$  flames, the  $Z$ -profile spreads asymmetrically about its initial position ( $x=1\text{cm}$ ). This is attributed to (a) enhanced diffusion in the proximity of the flame region ( $Z_{st}|_{A=0.6} \approx 0.11$ ) and (b) larger (smaller) flame induced velocities in the lighter (heavier) fuel (air) stream. In figs. 3.2b, the scaled density exhibits regions with  $\rho^* < 0$  for flame conditions with  $A=0.2$ , indicating the presence of a flame region lighter than the fuel and oxidizer streams. The inflection point in the density profile occurs at the location of the flame sheet, resulting in distinct RT stable fuel-flame ( $A_{f-fl} \approx -0.2$ ) and unstable flame-air ( $A_{fl-a} \approx 0.38$ ) interfaces. Under these conditions, the baseline flow is then transformed to a three-layer RT problem with an important distinction: Here, the third layer is active and sustains itself with fresh influx of combustion products. When such conditions exist, the underlying RT flow and flame properties are profoundly modified.

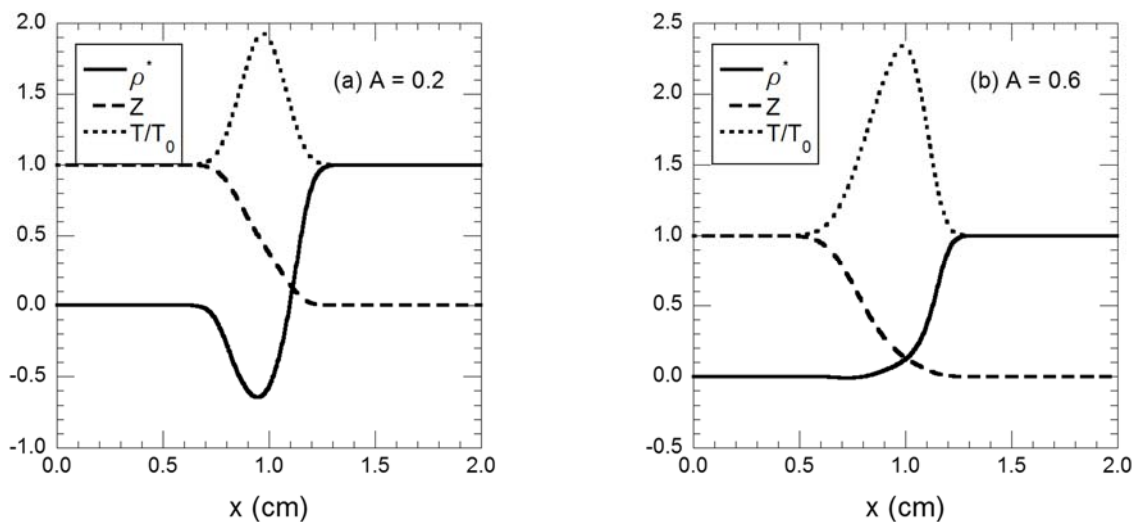


FIGURE 3.2: Mixture fraction, scaled density ( $\rho^* = (\rho - \rho_f) / (\rho_a - \rho_f)$ ) and temperature at  $t=2\text{ms}$  for flames at (a)  $A=0.2$  and (b)  $A=0.6$ .

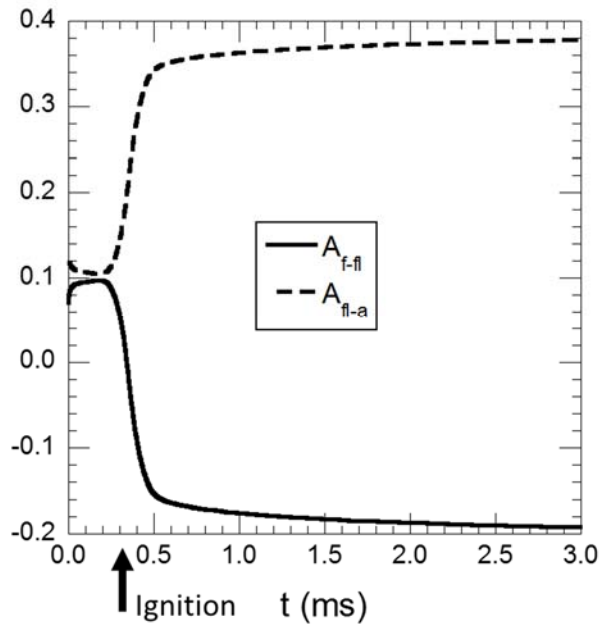
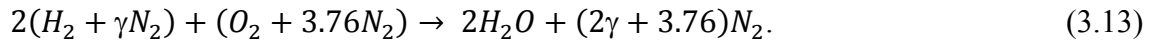


FIGURE 3.3: Time evolution of Atwood numbers corresponding to fuel-flame ( $A_{f-fl} = (\rho_{fl} - \rho_f) / (\rho_{fl} + \rho_f)$ ) and flame-air ( $A_{fl-a} = (\rho_a - \rho_{fl}) / (\rho_a + \rho_{fl})$ ) interfaces from an unperturbed low Atwood ( $A_{f-a} = 0.2$ ) simulation.

The time evolution of local Atwood numbers corresponding to fuel-flame ( $A_{f-fl} = \frac{\rho_{fl} - \rho_f}{\rho_{fl} + \rho_f}$ ) and flame-air ( $A_{fl-a} = \frac{\rho_a - \rho_{fl}}{\rho_a + \rho_{fl}}$ ) interfaces is depicted in figure 3.3 for case 1 ( $A_{f-a} = 0.2$ ). Upon ignition ( $t = 0.34$ ms), the density in the flame region rapidly decreases thereby increasing (decreasing) the local flame-air (fuel-flame) Atwood number. Asymptotically,  $A_{fl-a}$  attains a value roughly twice that of the original fuel-air interface. The value of  $A_{f-fl}$  on the other hand undergoes a sign reversal and asymptotically retains the magnitude of the original fuel-air interface. Thus, from figs. (3.2a) and (3.3), the flame acts as an active third layer (constantly replenished with fresh products of combustion), and transforms an initially unstable RT interface into distinct RT stable (fuel-flame) and unstable (flame-air) interfaces. The conditions for the existence of such a flame-generated

third layer may be derived by the following simple analysis based on a 1-step reaction model:



In the above equation, the fuel stream ( $H_2$ ) is assumed to be diluted with  $\gamma$  moles of  $N_2$ , which can be controlled to vary the initial Atwood number across the fuel-air interface ( $A_{f-a}$ ). Furthermore, the adiabatic flame temperature  $T_{ad}$  may be expressed as a polynomial function of the Atwood number, so that:

$$T_{ad} = \sum_{i=0}^6 a_i A_{f-a}^i. \quad (3.14)$$

In eq. (3.14), the polynomial coefficients were obtained from fitting to adiabatic flame temperature data from [93] for  $H_2$ -air combustion. The flame density may then be obtained as an explicit function of the Atwood number through the equation of state,

$$\rho_{fl} = \frac{P_0}{T_{ad}R/W_{fl}} \quad (3.15)$$

where the flame molecular weight ( $W_{fl}$ ) is obtained ( $W_{fl} = \frac{2W_{H_2O} + (2\gamma + 3.76)W_{N_2}}{2 + 2\gamma + 3.76}$ ) for products that appear on the RHS of equation (3.13). In figure 3.4, we plot  $\rho_{fl}^* = \frac{\rho_{fl} - \rho_f}{\rho_a - \rho_f}$  as a function of  $A_{f-a}$  from eq. (3.15), and find that for  $A_{f-a} < 0.5$ ,  $\rho_{fl}^* < 0$  so that a stable 3<sup>rd</sup> layer can be expected (similar criteria can easily be developed for other commonly used fuels). We have performed several 1D unperturbed simulations at different values of  $A_{f-a}$ , and find the simulations verify the criteria for third layer formation suggested by eq. (3.15) and fig. 3.4. We also plot  $\rho_{fl}^*$  obtained from the simulations in fig. 3.4, which are in good agreement with eq. (3.15).

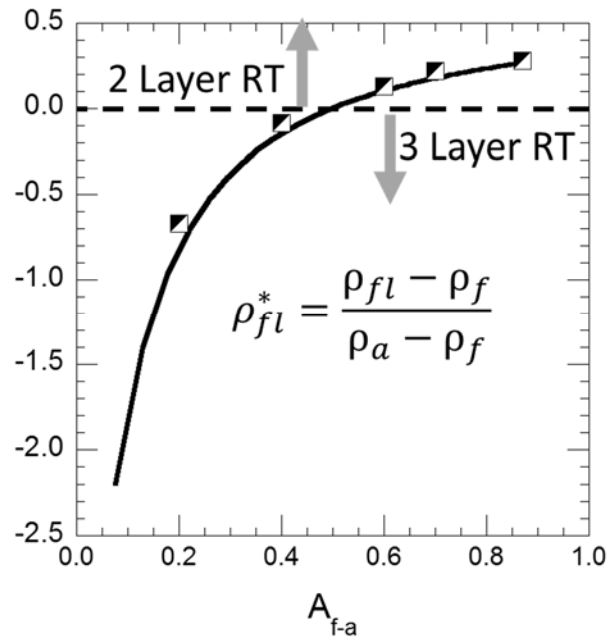


FIGURE 3.4: Normalized flame density ( $\rho_{fl}^* = (\rho_{fl} - \rho_f) / (\rho_a - \rho_f)$ ) from eq. (3.15) and 1D simulations (symbols) plotted against the initial Atwood number associated with the fuel-air interface. Flames with  $\rho_{fl}^* < 0$  develop a three-layer configuration.

In summary, based on 1D simulations and analysis presented in this section, we expect the flame-generated third layer to profoundly affect the density stratification and thereby, the evolution of the corresponding low A RT flames.

## CHAPTER 4: TWO LAYER RAYLEIGH-TAYLOR FLAMES

In this chapter, we examine the evolution of high  $A_{f-a}$  ( $> 0.5$ ) RT flames that retain their initial two-layer configuration through the combustion and heat addition processes. We discuss flames arising from both (§4.1) single-scale and (§4.2) multimode initial perturbations. Simulations initialized with a single-wavelength perturbation can provide valuable insights in to the linear and nonlinear stages of RT development, and can thus inform our understanding of the corresponding multimode problem [3,30,94,95].

### 4.1 Single Mode Perturbation

We describe results from detailed 2D, single-mode simulations of the inert (case 12) and reacting (case 13) RT problem at  $A = 0.6$ . At this Atwood number, the original two-layer configuration is preserved through the ignition and combustion processes. We also analyse the evolution of the fuel ( $Z=99\%$ ), flame sheet ( $Z = Z_{st} = 11.57\%$ ) and air ( $Z= 1\%$ ) surfaces in each case. When burning is present at the interface, it affects the flow and flame dynamics by (a) increasing diffusive transport, (b) enhancing the characteristic velocity scales by a factor proportional to a flame expansion ratio and (c) modifying the underlying density stratification for  $A_{f-a} < 0.5$  (discussed later in chapter 5). The increase in diffusive transport is due to higher flame temperatures, and results in a subsequent reduction in RT growth [87]. The flame expansion (discussed in chapter 3) serves as a countervailing effect and enhances RT growth. Figure 4.1 illustrates these issues qualitatively, and depicts contours of scaled density  $\left(\rho^* = \frac{\rho - \rho_f}{\rho_a - \rho_f}\right)$  from (b-e) inert and (f-

i) reacting RT unstable interfaces at  $A = 0.6$  ( $\lambda = 0.5 \text{ cm}$  and  $g = 6 \times 10^3 g_0$ ), realized at different scaled times. In these figures, the fuel ( $Z = 0.99$ ), flame sheet ( $Z = Z_{st}$ ) and air ( $Z = 0.01$ ) surfaces are indicated by black, grey and white lines respectively. The early stages of non-reacting RT evolution (figures 4.1 b-c) is marked by a thickening of the interface due to diffusion effects, while perturbations appear to grow symmetrically. The diffusive broadening develops as  $\sqrt{t}$  and eventually saturates (figures 4.1 d-e) at late times, as the perturbation growth enters a stage of nonlinear saturation. During this phase, the interface is differentiated into distinct bubble and spike structures (fig. 4.1 d-e), which are accompanied by secondary Kelvin-Helmholtz vortices that form on the sides of the RT plumes. The high Atwood simulations shown in fig. 4.1 exhibit asymmetry at late times ( $\tau \approx 6$ ) between evolving bubbles and spikes, consistent with the extensive [94-98] non-reacting RT literature.

For the reacting simulation (case 13 in figs. 4.1 f-i), ignition occurs at  $\tau \approx 1.9$  following an interval of diffusive broadening at the interface which leads to a combustible mixture. As discussed in chapter 3, localized combustion waves [92] impart a weak and rapidly decaying variable acceleration on the interface, so that the flame rapidly recovers to evolve under the influence of the imposed background acceleration. For RT flames with  $A_{f-a} > 0.5$  discussed here, the cross-stream density varies monotonically without the formation of the stable third layer. Accordingly, the evolution (figures 4.1 f-i) of such a high Atwood flame is qualitatively similar to its non-reacting counterpart.

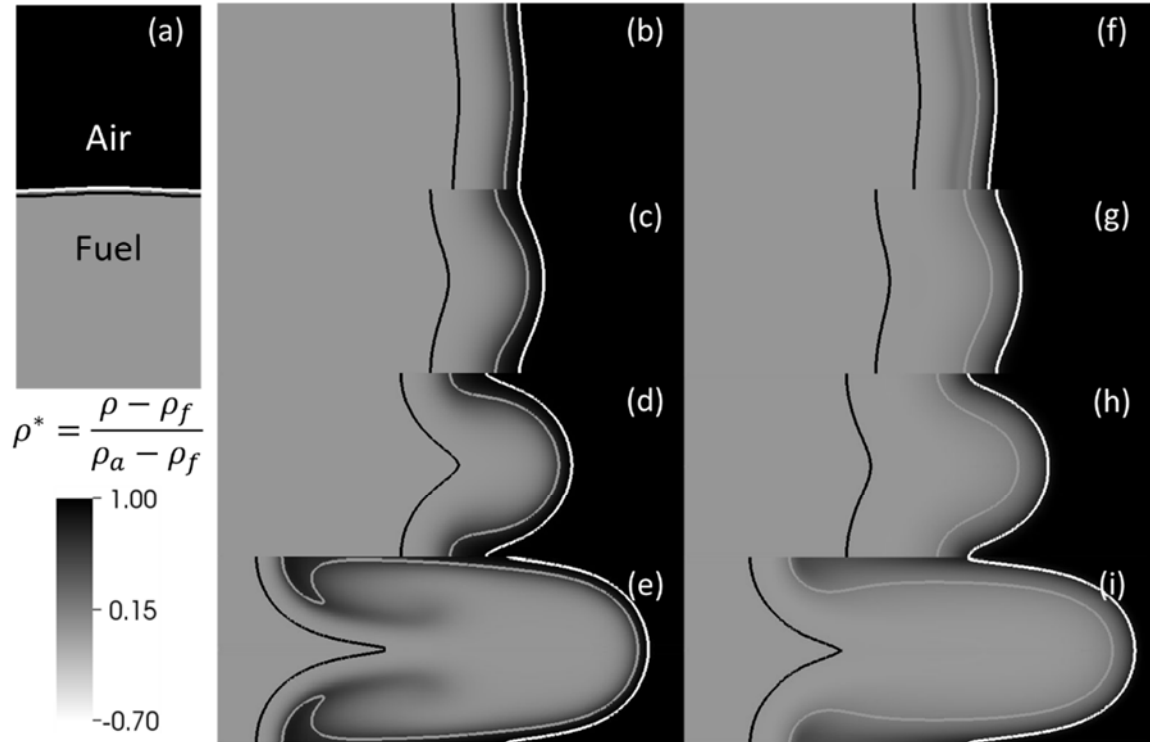


FIGURE 4.1: High A interface evolution represented by scaled density in (b-e) inert (case 12) and (f-i) reacting (without 3<sup>rd</sup> layer) RT unstable interfaces (case 13) realized at scaled times  $\tau = 2, 4, 6$  and  $10$  respectively. The initial interface is shown in figure (a) while iso-contours of fuel(black), flame-sheet(gray) and air(white) surfaces are overlaid on scaled density.

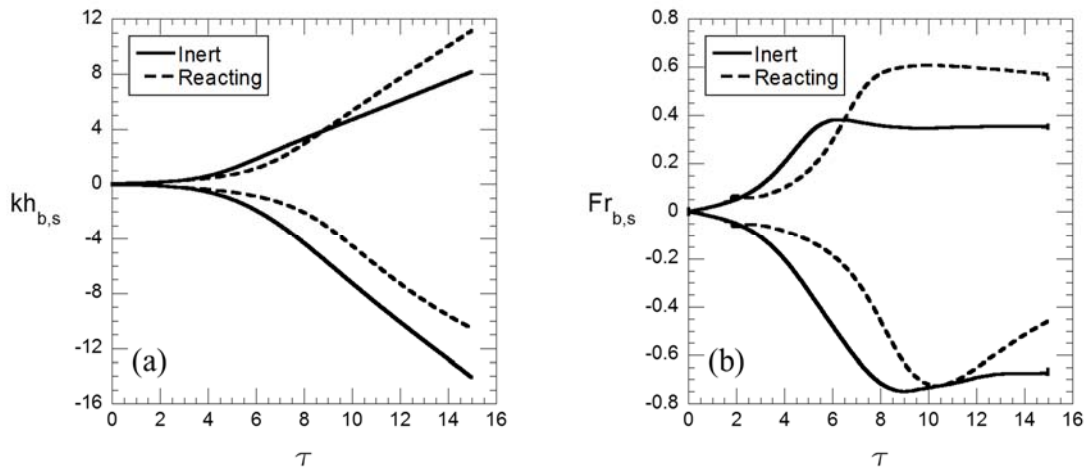


FIGURE 4.2: (a) Scaled bubble and spike amplitudes and corresponding (b) Froude numbers for reacting and non-reacting single mode interfaces ( $A = 0.6$ ) against scaled time ( $\tau = t\sqrt{Agk}$ ).

For single-mode RT, we quantify the interpenetration of fuel-air streams by evaluating the bubble (fuel into air) and spike (air into fuel) amplitudes according to,

$$h_b = \max(x|_{Z=0.5}) - x_{unperturbed}|_{Z=0.5} \text{ and} \quad (4.1)$$

$$h_s = \min(x|_{Z=0.5}) - x_{unperturbed}|_{Z=0.5}. \quad (4.2)$$

In the above equations,  $\max(x|_{Z=0.5})$  signifies the location of the bubble tip along the  $Z=0.5$  iso-contour while the spikes are identified by the corresponding minimum locations. Both bubble and spike amplitudes are measured with respect to  $x_{unperturbed}|_{Z=0.5}$ , the corresponding x-location in an independent unperturbed interface simulation. Such a definition accounts for the drift in the location of  $Z_{50}$  due to diffusive or combustion wave effects. In figure 4.2(a), we plot the scaled bubble ( $kh_b$ ) and spike ( $kh_s$ ) amplitudes against the scaled time ( $\tau = t\sqrt{Agk}$ ) for the inert and reacting interfaces (cases 12 and 13). For  $kh \ll 1$ , perturbation amplitudes at first grow exponentially and symmetrically followed by a prolonged phase of nonlinear saturation where the spikes outpace bubbles. During the linear stage, reacting RT perturbation growth is affected by increased diffusion following ignition ( $\tau_{ign} \approx 1.87$ ), although the late time non-linear growth appears to be indifferent to this effect.

In fig. 4.2(b), we plot the Froude numbers associated with the bubble ( $Fr_b$ ) and spike ( $Fr_s$ ) tips

$$Fr_{b,s} = \frac{|V_{b,s}|}{\sqrt{\frac{Ag\lambda}{1+A}}}, \quad (4.3)$$

where  $V_{b,s}$  refers to the corresponding bubble/spike terminal velocities. The initial exponential growth of the interface during the linear stages gives way to the asymptotic saturation of the Froude number as the flow becomes nonlinear (figure 4.2 (b)). Eventually,

at late times ( $\tau > 5$ ), the diffusive broadening ( $\sim 8\sqrt{Dt}$ ) of the interfaces asymptotes (see figs. 4.1 g-i) such that the RT growth ( $\sim t\sqrt{Agk}$ ) is no longer affected by the enhanced diffusion in high temperature flames. During the non-linear stage of growth, potential flow models suggest bubbles and spikes grow with a constant Froude number given by [29,99],

$$Fr_b = \frac{1}{\sqrt{C_d/2}} \quad (4.4)$$

$$Fr_s = \frac{1}{\sqrt{C_d/2}} \sqrt{\frac{1+A}{1-A}} \quad (4.5)$$

where  $C_d$  is the drag coefficient ( $C_d = 6\pi$  for 2D flows). At late times, the inert bubbles and spikes attain a constant Froude number within 7% of equations (4.4) and (4.5). In contrast, the observed Froude number associated with reacting bubbles in figure 4.2 (b) are under predicted by equation (4.4).

The observed increase in bubble terminal velocities may be understood in terms of the effect of burning on the flow properties of RT interfaces. Consider a parcel containing a stoichiometric mixture of unburnt fuel and air moving through the flame region with a velocity  $U_{Z_{st_{unburnt}}}$  and density  $\rho_{Z_{st_{unburnt}}}$ . Ignition and subsequent combustion of such a mixture would modify the local density to  $\rho_{Z_{st_{burnt}}} = \rho_{fl}$  (where  $\rho_{fl}$  can be evaluated from equation 3.15), while the post-combustion velocity  $U_{Z_{st_{burnt}}}$  will be modified to satisfy mass conservation across the unburnt-burnt interface:

$$U_{Z_{st_{burnt}}} = \frac{\rho_{Z_{st_{unburnt}}}}{\rho_{Z_{st_{burnt}}}} \times U_{Z_{st_{unburnt}}} = \sigma|_{t \rightarrow \infty} U_{Z_{st_{unburnt}}}. \quad (4.6)$$

Thus, from equations 4.3 and 4.6 we anticipate

$$Fr_{b_{react}} \approx \sigma|_{t \rightarrow \infty} Fr_{b_{inert}}. \quad (4.7)$$

In the above equation, the flame expansion ratio  $\sigma|_{t \rightarrow \infty} = \left( \frac{\rho_{Z_{st_{unburnt}}}}{\rho_{Z_{st_{burnt}}}} \right)$  may be determined from the appropriate equation of state and a simplified 1-step reaction model (such as equation 3.13) to obtain

$$\sigma|_{t \rightarrow \infty} = \frac{\rho_{Z_{st_{unburnt}}}}{\rho_{Z_{st_{burnt}}}} = \frac{\left( \frac{P_0 W_{st}}{T_0 R} \right)}{\rho_{fl}} = \left( \frac{W_{st}}{W_{fl}} \times \frac{T_{ad}}{T_0} \right) = \left( \frac{W_{st}}{W_{fl}} \times \frac{\sum_{i=0}^6 a_i A_{f-a}^i}{T_0} \right). \quad (4.8)$$

Here,  $W_{st}$  is the unburnt mixture molecular weight obtained for reactants that appear on LHS of equation 3.13, while  $W_{fl}$  is obtained similarly from the RHS of that equation. Thus, we find combustion enhances the RT terminal velocities/Froude numbers by a factor  $\sigma|_{t \rightarrow \infty}$  that is in turn a function of the fuel-air Atwood number. RT bubbles trapped in the flame region will register a higher effective Froude number compared to similar structures in the non-reacting flow.

We clarify these issues in figure 4.3, where we plot the time evolution of the flame expansion parameter  $\sigma$  for unperturbed flames at low and high  $A_{f-a}$ . Clearly, ignition is followed by a rapid decrease in the flame density and a corresponding increase in  $\sigma$ . Surprisingly, for the low  $A_{f-a}$  (three layer) flame where  $\rho_{fl} < \rho_f < \rho_a$ , the saturation value of the flame expansion ratio is lower than the corresponding high  $A_{f-a}$  (two layer) flame. This is a consequence of more  $H_2$  content ( $\gamma \rightarrow 0$ ) in the fuel stream at high A which results in increased  $T_{ad}$ . In figs. 4.3 (b) we plot asymptotic  $\sigma|_{t \rightarrow \infty}$  values from the simulations at different  $A_{f-a}$ , which are within 10% of eq. 4.8. Furthermore,  $\sigma|_{t \rightarrow \infty}$  rapidly increase with  $A_{f-a}$  while  $A_{f-a} \leq 0.5$  (three layer flames), following which it saturates to  $\sim 2.16 \pm 0.036$  at high A (two-layer), a trend dictated by the saturation of the adiabatic flame temperature (in eq. 4.8). Finally, the asymptotic reacting bubble Froude numbers

from our two-layer RT simulations (fig. 4.2b) are over predicted by 20% using equation 4.7. The comparison of equation 4.7 for a range of  $A_{f-a}$  with our simulations is discussed in chapter 5.

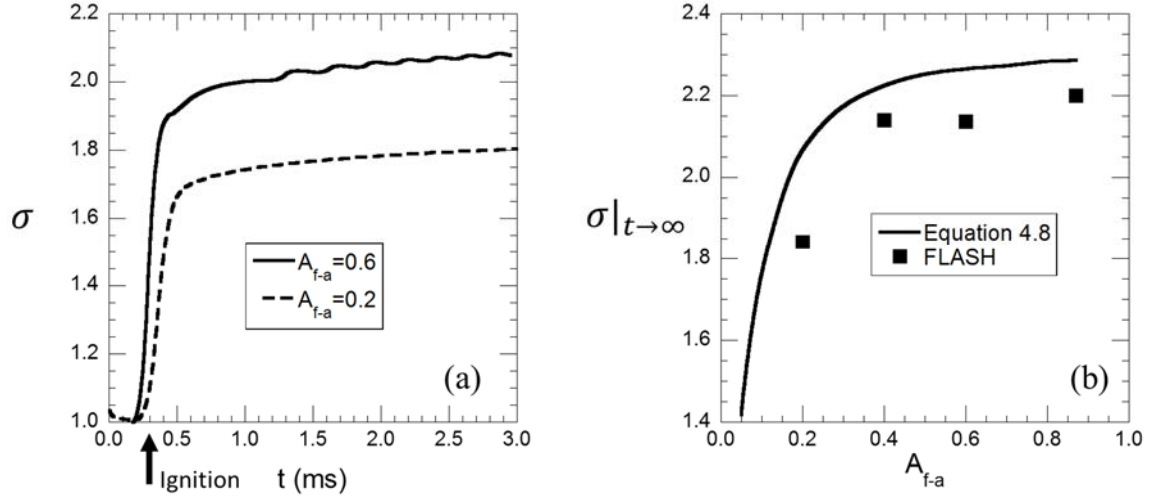


FIGURE 4.3: (a) Evolution of the flame expansion parameter ( $\sigma = \rho_{Z_{st_{unburnt}}} / \rho_{Z_{st_{burnt}}}$ ) for low and high  $A$  unperturbed interfaces and (b) comparison of the asymptotic expansion parameter ( $\sigma |_{t \rightarrow \infty}$ ) with predictions from equilibrium chemistry (equation 4.8).

We also estimate the reacting bubble velocity and Froude number by accounting for the additional buoyancy associated with the flame in a modified drag-buoyancy force balance equation [100-105],

$$(\rho_f + C_m \rho_a) \frac{dv_b}{dt} = g(\rho_a - \rho_f) - \frac{C_d \rho_a v_b^2}{\lambda} + g \Delta \rho_{com}. \quad (4.9)$$

In eq. (4.9),  $C_m = 1(2)$  is the added mass coefficient for 3D (2D) and  $\Delta \rho_{com} \approx \rho_{Z_{st_{unburnt}}} - \rho_{Z_{st_{burnt}}}$  signifies changes in the flame density due to combustion. Asymptotically, we require  $\frac{dv_b}{dt} = 0$ , to obtain a reacting bubble Froude number  $Fr_{b_{react}}$ ,

$$Fr_{b_{react}} = \sqrt{\frac{2}{C_d} \times \left(1 + \frac{\Delta \rho_{com}}{(\rho_a - \rho_f)}\right)} = Fr_{b_{inert}} \times \sqrt{\left(1 + \frac{\Delta \rho_{com}}{(\rho_a - \rho_f)}\right)} \quad (4.10)$$

while the analogous calculation for spikes would result in,

$$Fr_{S_{react}} = Fr_{S_{inert}} \times \sqrt{\left(1 - \frac{\Delta \rho_{com}}{(\rho_a - \rho_f)}\right)}. \quad (4.11)$$

Equations 4.10-4.11 evaluated using ideal gas law and adiabatic flame temperature calculations as discussed in chapter 3, under predicts the bubble Froude number from our simulation by 30% but the agreement is improved at low A (discussed later in chapter 5) whereas for all A equation 4.11 fails to predict the spike Froude number.

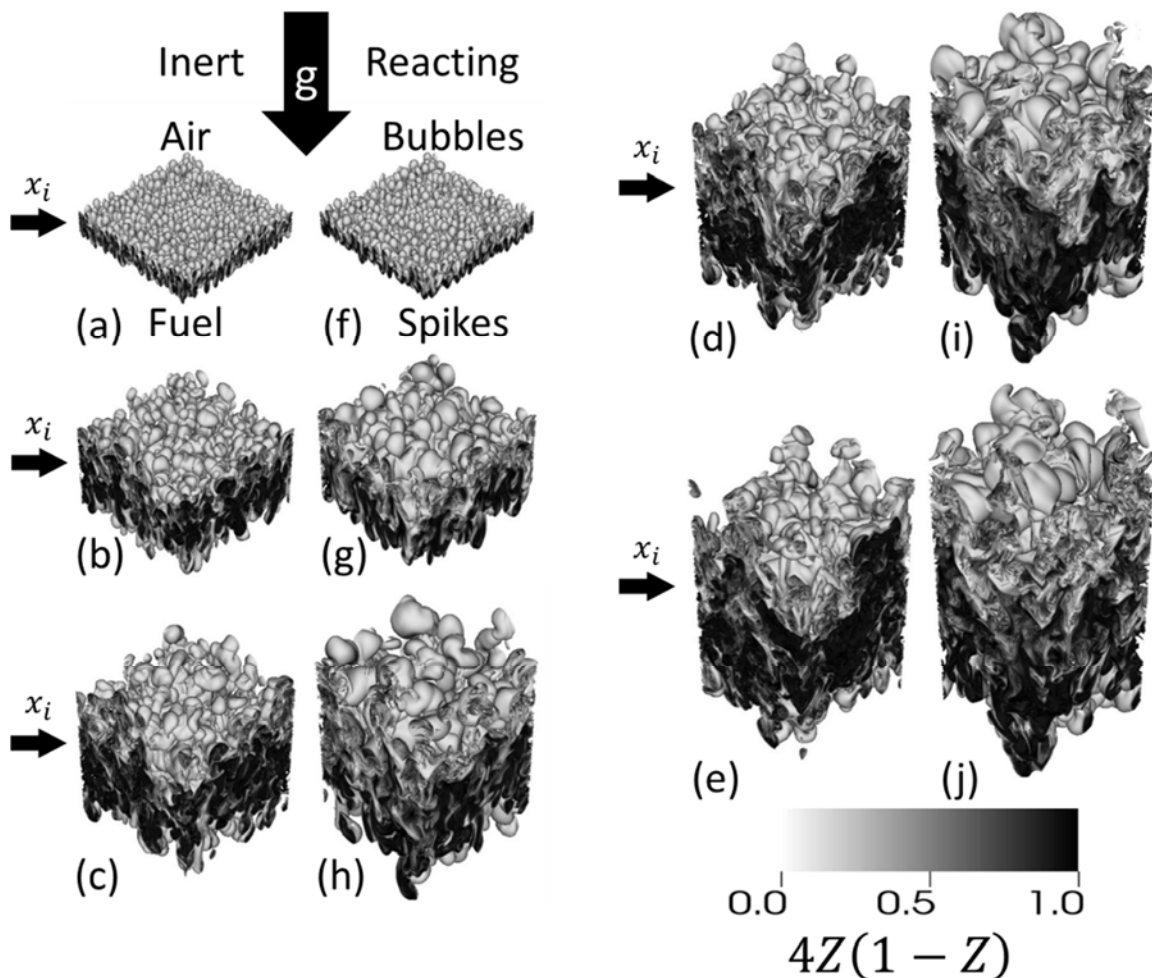


FIGURE 4.4: Evolution of the mixing zone represented through iso-surfaces of  $4Z(1-Z)$  from  $A = 0.6$  inert and reacting RT interfaces. Images shown correspond to scaled times  $\tau =$  (a, f) 1, (b, g) 5, (c, h) 10, (d, i) 15 and (e, j) 20. The initial interface location ( $x_i$ ) is indicated by horizontal arrows in each realization.

## 4.2 Multimode Perturbation

We now extend our analysis to include RT flames at  $A = 0.6$ , and evolving from a non-premixed interface that is perturbed with a multimode function of the form given by eq. (3.8). Once again, we characterize the interface evolution for multimode RT flames by comparison with the baseline non-reacting case. Figures 4.4 a-e (f-j) are plots of isocontours of  $4Z(1-Z)$  which highlight the development of the mixing zone for the non-reacting (reacting cases) at scaled times  $\tau = Agt^2/L = 1, 5, 10, 15$  and  $20$ . Note that  $0 \leq 4Z(1-Z) \leq 1$ , where the lower and upper limits indicate completely unmixed and mixed zones respectively. Initially ( $\tau < 1$ ), prescribed modes grow symmetrically (figs. 4.4 a and f) in the linear stages of the instability without interaction with their neighbours. This is accompanied by diffusion of the mixing zone that results in a combustible mixture across the interface. For the reacting interface, such a mixture autoignites at  $\tau_{ign} \approx 0.035$ , and the subsequent flame formed within the mixing zone (fig. 4.4f) continues to grow similar to the inert case (figs. 4.4 a). This is followed by self-similar growth for ( $\tau \geq 5$ ), where long-wavelength modes ( $\lambda$ ) are formed through mode coupling of higher harmonics (figs. 4.4 b-e and g-j). During this phase, longer modes ( $\lambda$ ) are visible for the reacting interface than the inert case, suggesting the mode coupling proceeds with a higher merger rate in the presence of a flame enhanced bubble Froude number. The horizontal arrow in fig. 4.4 indicate the location of the unperturbed interface ( $x_i$ ), and serves to illustrate the asymmetry of the mixing layer for this high  $A$  flow. As expected for a high  $A$  RT unstable interface [88,106,107], spikes outpace bubble growth in our non-reacting simulation (figs. 4.4 c-e). In contrast, the reacting RT appears to retain a higher degree of symmetry

(bubbles $\approx$ spikes) well in to the self-similar turbulent stage visible in fig. 4.4 j, a consequence of (a) higher reacting bubble Froude number and (b) preferential travel of positively buoyant flame against imposed acceleration to enhance the bubble growth . Furthermore, the width of the reacting mixing layer is larger than the corresponding non-reacting case throughout the self-similar growth regime. We suspect this is a consequence of the additional buoyancy experienced by the flame region, an effect that is expected to dominate at late times, through the buoyancy-driven flame expansion mechanism discussed earlier for the single-mode interface (§4.1).

The approach to self-similarity in reacting and non-reacting RT is illustrated in figs.4.5. We plot cross-stream profiles of the (y-z) planar-averaged mixture fraction ( $\langle Z \rangle$ ) and scaled density ( $\langle \rho^* \rangle$ ) at different times from cases 26 and 27. These profiles are plotted as functions of the similarity variable ( $\xi$ ),

$$\xi = \frac{x - x_{\langle Z_{50} \rangle}}{x_{\langle Z_{01} \rangle} - x_{\langle Z_{99} \rangle}} \quad (4.12)$$

for the inert (a-b) and reacting (c-d) interfaces for  $\tau > 5$  with an interval of  $\Delta\tau = 1$ . In eq. (4.12),  $x_{\langle Z_{50} \rangle}$  corresponds to the location of the 50% planar-averaged mixture fraction surface, while  $x_{\langle Z_{01} \rangle}$  and  $x_{\langle Z_{99} \rangle}$  refer to the mean bubble (air stream) and spike (fuel stream) locations. Note that in figs. 4.5 c-d, the 1D unperturbed flame profile is plotted as the thick grey line as a baseline for comparison. From fig. 4.5, the presence of a flame region does not affect the self-similar evolution of the underlying RT flow, so that we can expect eq. (1.3) to still govern the late-time dynamics of the turbulent mixing layer in both cases. Furthermore, the self-similar Z-profiles for the two-layer RT flame exhibits the same behaviour as the unperturbed 1D flames. Slight deviations from the 1D density profile are attributed to the presence of the unburnt mixture within the turbulent mixing zone. This is

a consequence of the entrainment rate of fuel and air into the mixing zone ( $\sim\tau$ ) exceeding the rate of flame formation ( $\sim\tau_{ign} \approx 0.035$ ).

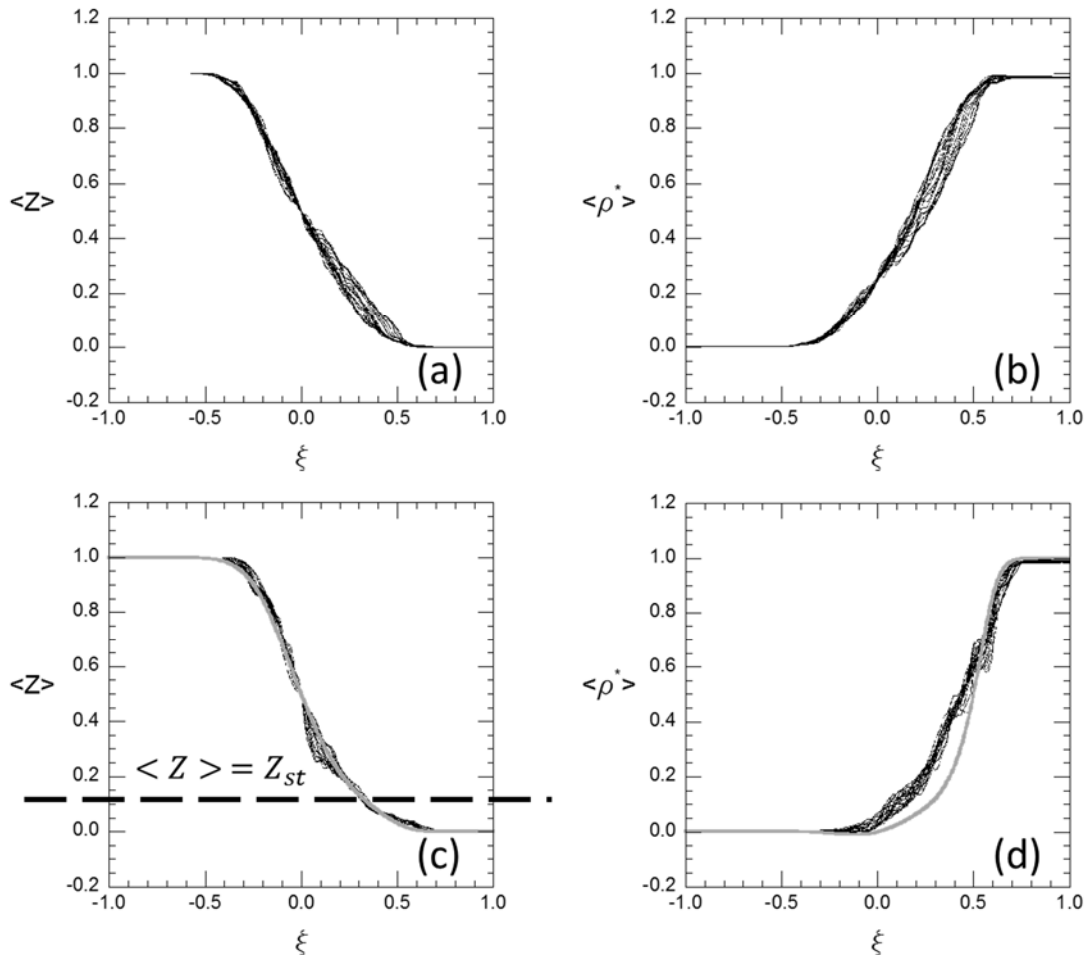


FIGURE 4.5: Scaled profiles of planar-averaged mixture fraction and density from  $A = 0.6$ , multimode (a-b) inert and (c-d) reacting interfaces obtained at intervals of  $\Delta\tau = 1$  in the range  $\tau = 5-22$ . The 1d flame profile (case 3) is shown with a thick grey line for comparison. The profiles are plotted against the coordinate  $\left(\xi = (x - x_{Z_{50}}) / (x_{Z_{01}} - x_{Z_{99}})\right)$ .

Figures 4.4 – 4.5 provide preliminary evidence of the existence of self-similarity in turbulent RT fronts even when a flame is present. We examine this issue in greater detail by tracking the behaviour of bubble and spike fronts for both reacting and non-reacting

flows. Note that simulations [3,30] and experiments [108] of non-reacting RT suggest self-similarity in such flows requires dominant bubbles (and probably spikes) evolve such that

$$\beta_{b,s} = \frac{\langle \lambda_{b,s} \rangle}{\langle h_{b,s} \rangle} \quad (4.13)$$

where  $\langle \lambda_{b,s} \rangle$  indicates the dominant bubble(spoke) wavelength within the bubble(spoke) front and  $\beta_{b,s}$  is the self-similarity parameter. In figures 4.6 (a) – (d), the bubble fronts (identified as the x-heights  $x|_{\langle z \geq 0.01 \rangle}(y, z)$ ) are shown at early ( $\tau = 5$ ) and late times ( $\tau = 20$ ) for the inert (a-b) and reacting (c-d) interfaces. The corresponding spike fronts ( $x|_{\langle z \geq 0.99 \rangle}(y, z)$ ) are plotted in figures 4.7. In both figures, only the leading bubbles/spikes that satisfy  $(x_{z_{0.99}} \geq 0.75(x_{\langle z \rangle_{0.99}} - x_i) = 0.75h_{b,s})$  are visualized[3]. Even at early times ( $\tau = 5$ ), the reacting interface contains about half the number of bubbles as the inert front ( $\sim 50$  as opposed to  $\sim 100$ ). These structures coalesce to  $\sim 12$  (20) at late times ( $\tau = 20$ ), corresponding to  $\log_2 \left( \frac{50}{12} \right) \approx 2.06$  (2.32) generations of reacting (inert) bubble evolution. In contrast, at early times the two interfaces have comparable ( $\sim 120$ ) leading spike structures that evolve through 2.00 (3.38) generations to reduce to  $\sim 30$  ( $\sim 10$ ) for the inert (reacting) interfaces.

We use an autocorrelation analysis of figs. 4.6 – 4.7 [3,30] to compute the evolution of the mean bubble and spike diameters ( $D_{b,s}$ ) as a function of time. The self-similarity parameter ( $\beta_{b,s}$ ) for bubbles and spikes is evaluated here using Daly's suggestion[109]

$$\left( \lambda_{b,s} = D_{b,s} \frac{2}{A+1} \right)$$

to relate mean diameters to the corresponding dominant wavelengths. For both reacting and non-reacting RT, the mean bubble diameters in figure 4.8 (a) grow linearly with  $\tau$ , a behavior that suggests self-similarity. For case 26, the average spike tends to be narrower (fig. 4.8 (b)), consistent with [108] for these high A simulations. We also

show the evolution of the spike front under flame conditions in fig. 4.8 (b), where the enhanced diffusive transport due to burning rapidly increases the mean reacting spike for  $\tau < 12$ . Thereafter, spike diameter growth is steady and follows the trajectory of the non-reacting case, eventually growing to  $\sim 1/3$  the box size by the end of the simulation. The corresponding self-similarity parameters are shown in fig. 4.8 (c), and clearly indicate the presence of the flame does not significantly affect the self-similar nature of turbulent RT. However, burning appears to affect the saturation values of  $\beta_s$  through the increased diffusion mechanism discussed above, leading to a saturation value that is 20 % larger than the non-reacting spike front.

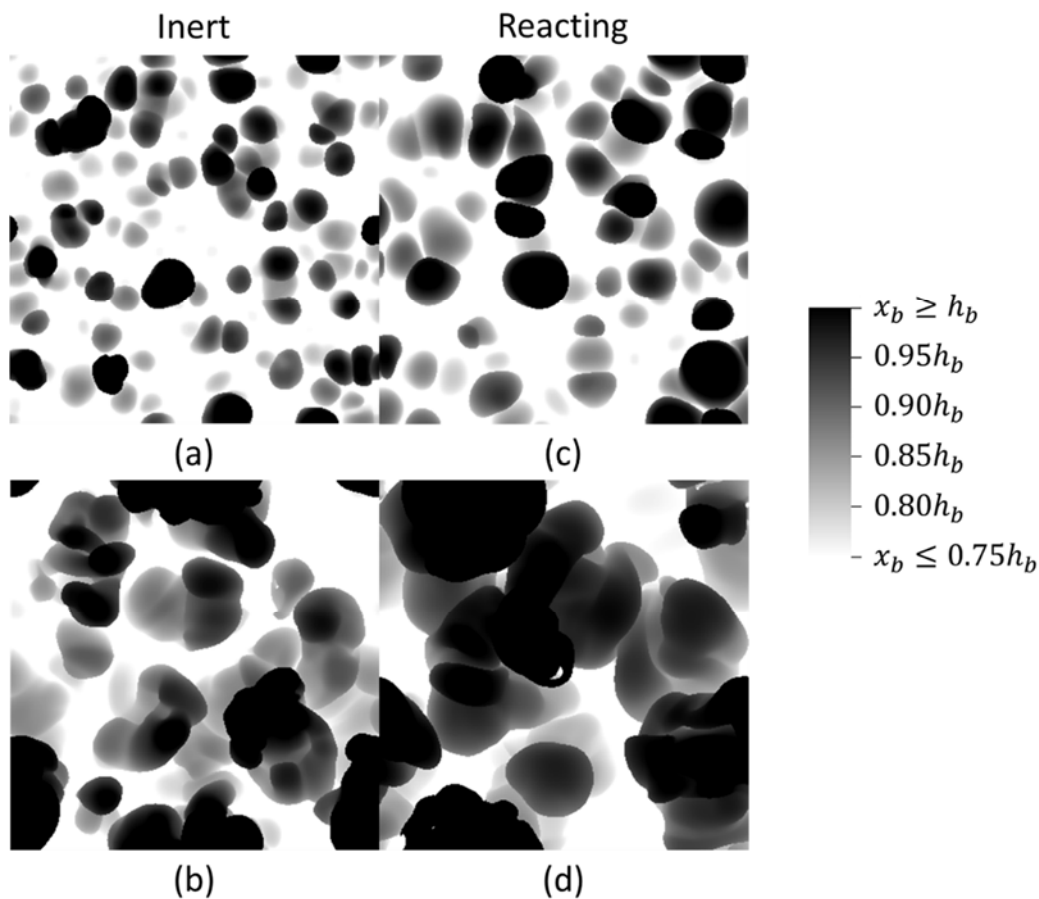


FIGURE 4.6: Bubble fronts for high A (a-b) inert and (c-d) reacting interfaces at early ( $\tau = 5$ ) and late times ( $\tau = 20$ ).

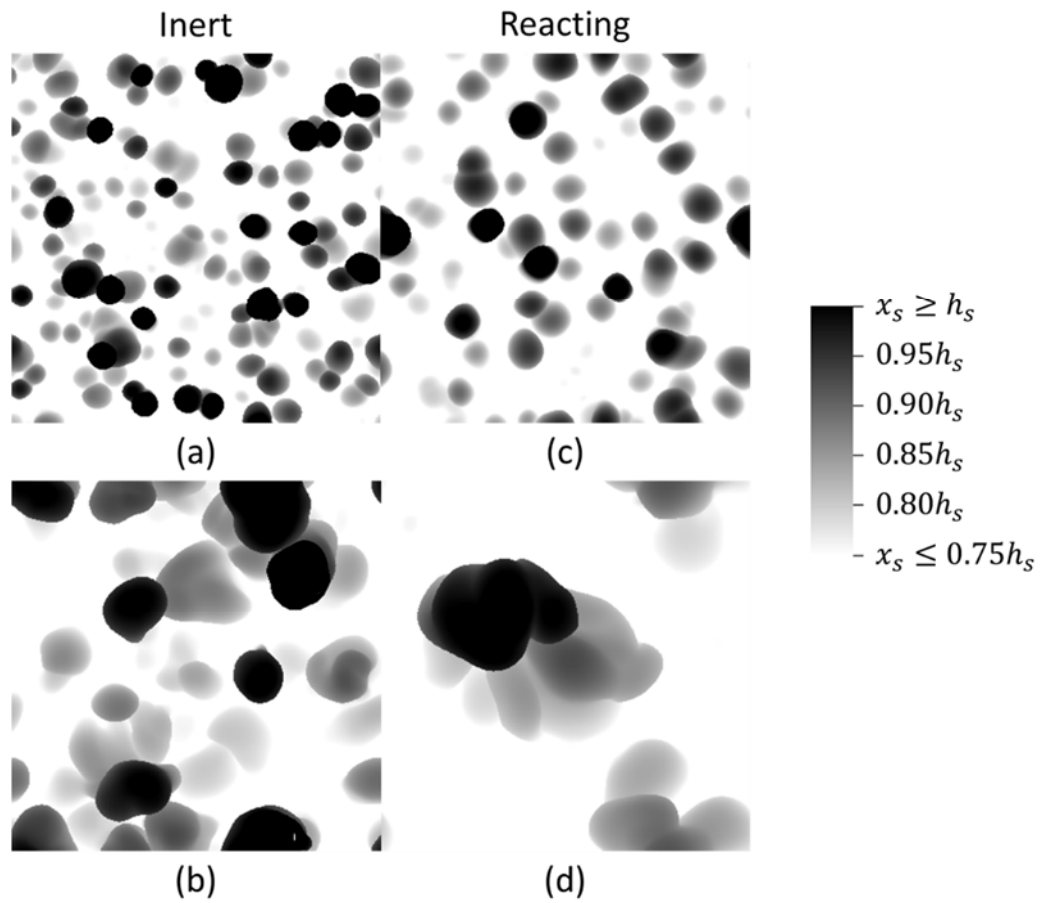


FIGURE 4.7: Spike fronts for high A (a-b) inert and (c-d) reacting interfaces at early ( $\tau = 5$ ) and late times ( $\tau = 20$ ).

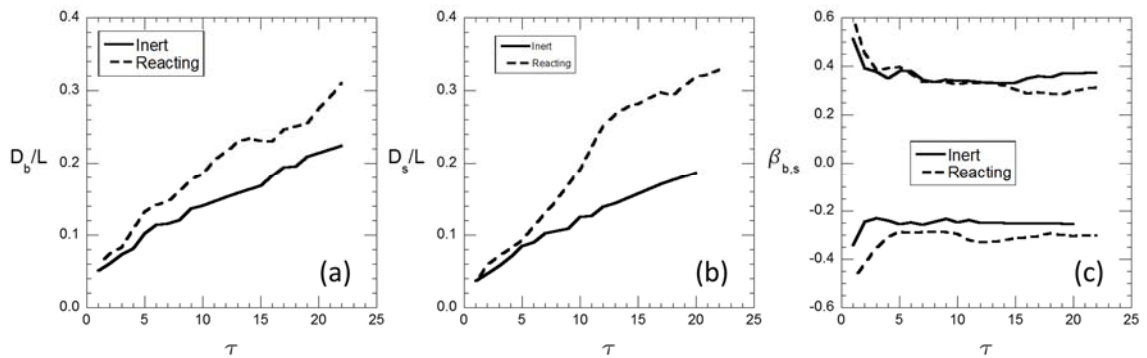


FIGURE 4.8: Evolution of mean (a) bubble and (b) spike diameters obtained from the autocorrelation procedure of [3] and the corresponding (c) self-similarity parameter ( $\beta_{b,s}$ ) plotted against scaled time for  $A = 0.6$ , inert and reacting RT flow.

We quantify the growth of the mixing zone towards the fuel (spike) and air (bubble) streams by tracking the location of planar averaged ( $\langle * \rangle$ ) mixture fraction, so that  $x_{\langle Z \rangle_{01}}$  and  $x_{\langle Z \rangle_{99}}$  correspond to the mean bubble and spike locations respectively. The resulting bubble ( $\langle h_b \rangle$ ) and spike ( $\langle h_s \rangle$ ) amplitudes are scaled with the box width  $L$ , and plotted as a function of  $\tau$  in figure 4.9. Note that we define  $\langle hb \rangle$  and  $\langle hs \rangle$  according to

$$\langle h_{b,s} \rangle = x_{\langle Z \rangle_{01,99}} - x_i. \quad (4.14)$$

The corresponding growth constant ( $\alpha_{b,s} = \frac{1}{L} \frac{d\langle h_{b,s} \rangle}{d\tau}$ ) is plotted in figure 4.9 (b) for both the reacting and non-reacting RT. When combustion is absent (case 26), the flow exhibits a shortened linear growth phase ( $\tau < 5$ ), followed by a terminal self-similar phase characterized by a constant  $\alpha_b \approx 0.027 \pm 0.01$  similar to previously reported values in [3]. However at late times a gradual decline in  $\alpha_b$  is observed as bubbles lose their effective buoyancy by entraining and trapping air (heavy fluid). During the early stage of the reacting interface evolution ( $\tau < 5$ ), the bubble and spike amplitudes (fig. 4.9 a) appear largely unaffected by the presence of flame. However at late times ( $5 < \tau$ ) (see figures 4.4 b-e and g-j), the reacting interface evolves with higher growth rates for both spikes and bubbles. This is attributable to two effects discussed earlier in this work: the preference for modes with larger diameters (than the inert) and the observed increase in the terminal bubble velocity/Froude number due to the additional buoyancy resulting from the flame presence. In light of these effects, we expect the reacting mixing zone ( $\approx |h_b| + |h_s|$ ) to grow faster than inert. Thus, in fig. 4.9 (b), reacting bubbles evolve with a larger growth rate during the self-similar stage  $\alpha_b \approx 0.051 \pm 0.01$ , while spike growth rates ( $\alpha_s \approx 0.064 \pm 0.02$ ) are comparable to the non-reacting case.

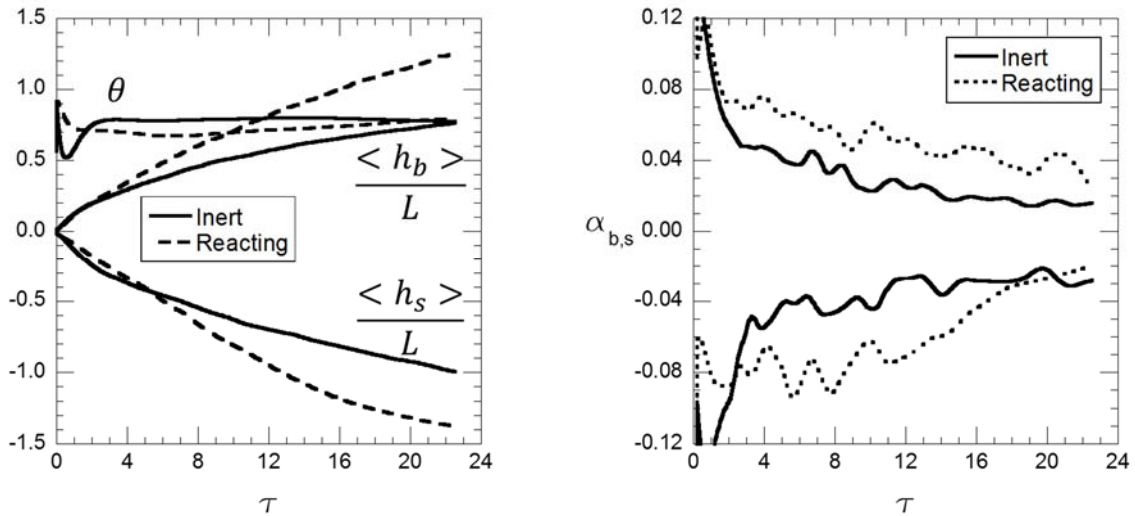


FIGURE 4.9: Evolution of (a) molecular mixing parameter ( $\theta$ ) and scaled bubble and spike amplitude for high A ( $A=0.6$ ) inert and reacting interfaces against scaled time. The corresponding amplitude growth constants ( $\alpha_{b,s}$ ) are shown in (b).

The ratio of small-scale (atomic) mixing to large-scale mixing from entrainment may be characterized through the molecular mixing parameter [110,111],

$$\theta = \frac{\int_{-\infty}^{\infty} \langle Z(1-Z) \rangle dx}{\int_{-\infty}^{\infty} \langle Z \rangle \langle 1-Z \rangle dx}. \quad (4.15)$$

Thus,  $\theta$  can vary between 0 and 1, where the lower limit signifies a perfectly unmixed state, while the upper limit indicates perfect mixing. Note that the initially large values of  $\theta$  are due to the discrete representation of the interface on the finite numerical grid, and not the result of a physical mixing process. At early times, much of the mixing layer growth is driven by linear growth of individual modes, with insignificant transport in the lateral directions. Such a growth pattern does not engender small-scale mixing, thereby rapidly decreasing the mixing parameter from its initially large value. Eventually, as individual modes achieve nonlinear saturation, they engage in a bubble merger process thereby generating small-scale mixing and increasing  $\theta$ . For non-reacting RT, the mixing

parameter asymptotically attains a value  $\approx 0.79 \pm 0.007$  within the range of previously reported values in from experiments [31,106] and simulations[3,111]. The increased diffusive transport resulting from combustion suppresses small-scale mixing slightly in the reacting RT simulations, yielding a value of  $\theta \approx 0.71 \pm 0.007$  for  $5 < \tau < 16$ . However, at late times ( $\tau \geq 18$ ), small-scale mixing recovers in response to aggressive mode-coupling as  $\theta$  eventually approaches the asymptotic value reported from the inert simulations.

## CHAPTER 5: THREE LAYER RAYLEIGH-TAYLOR FLAMES

In this chapter, we discuss the evolution of fuel-air interfaces, which upon ignition form a flame-induced ( $\rho_f < \rho_{fl} < \rho_a$ ) three-layer RT configuration. As previewed in chapter 3, the modification to the density stratification profile is an effect that depends on the Atwood number, and can result in the formation of an active intermediate layer comprised of combustion products when  $A_{f-a} < 0.5$ . When perturbations are present at the interface, the emergence of the intervening layer can profoundly influence the resulting stability of the flow. For reacting interfaces, we classify the flows based on the global stability of the stratification of the outer fuel/air layers (i.e.  $gA_{f-a}$ ). For example, an initially (globally) unstable fuel-air (f-a) interface ( $gA_{f-a} < 0$ ) will be transformed upon ignition into distinct stable (fuel-flame (f-fl),  $gA_{f-fl} > 0$ ) and unstable (flame-air (fl-a),  $gA_{fl-a} < 0$ ) interfaces. Conversely, an initially (globally) stable interface ( $gA_{f-a} > 0$ ), following ignition will deteriorate to unstable ( $gA_{f-fl} < 0$ ) and stable ( $gA_{fl-a} > 0$ ) interfaces. We discuss below the implications of this transformation in each case, when the interfaces are subject to single- and multi-mode perturbations.

### 5.1 Single Mode Perturbation

We repeat the 2D single mode calculations from chapter 4 ( $\lambda = 0.5$ ), but with  $A_{f-a} = 0.2$  and with a constant background acceleration of  $g = \pm 6 \times 10^2 g_0$ . The results from the reacting simulation are compared with a baseline, globally unstable ( $gA_{f-a} < 0$ ), inert RT calculation. Figure 5.1 depicts contours of the scaled density ( $\rho^*$ ) realized at

different non-dimensional times ( $\tau = t\sqrt{|A^*|gk}$ ) for: baseline inert (b-e), globally unstable (f-i), and globally stable (j-m) reacting interfaces. Note that  $A^*$  corresponds to the unstable Atwood number driving the flow so that for the inert interface  $A^* = A_{f-a}$ , while for the reacting cases  $A^* = \begin{cases} A_{f-a}, t < t_{ign} \\ A_{fl-a}, t \geq t_{ign} \end{cases}$  when  $g < 0$  and  $A^* = \begin{cases} A_{f-a}, t < t_{ign} \\ A_{f-fl}, t \geq t_{ign} \end{cases}$  for  $g > 0$ . Once again in all the figures, the fuel ( $Z=0.99$ ), flame sheet ( $Z = Z_{st}$ ) and air ( $Z=0.01$ ) surfaces are indicated by black, gray and white lines respectively. The evolution of the unstable inert interface is analogous to that of the  $A = 0.6$  case discussed earlier, except the bubble and spike structures remain fairly symmetric even at late times for the modest density ratios investigated here (fig. 5.1e). Prior to ignition, the globally-unstable reacting interface exhibits a linear growth phase consistent with classical RT. In contrast, the globally-stable reacting case shows no growth (except for a periodic oscillation [99,112] with a frequency  $\sqrt{Agk}$ ) until ignition modifies the fundamental stratification as described earlier. For both the reacting simulations, ignition occurs at  $\tau \approx 1.3$ , and results in the formation of an intervening third layer which dramatically alters the (post-ignition) RT flame development.

Globally stable ( $gA_{f-a} > 0$ ) flame (figs. 5.1 j-m): At ignition, the interface amplitude undergoes a phase inversion (driven by periodic oscillations for a RT stable interface [99,112]) and is significantly smaller than the corresponding unstable inert interface. Shortly thereafter, the high temperature associated with the flame enhances mass diffusion ( $D_{react} \approx 2D_{inert}$ ), leading to significant broadening of the interface thickness (figs. 5.1 j-l), and an increased separation distance ( $\sim 8\sqrt{D_{react}t}$ ) between the fuel and air streams. In addition to the diffusive broadening, the unstable fuel-flame interface grows asymmetrically towards the fuel stream (figs. 5.1m). Note that the stable air surface is

unaffected by the growth of the unstable fuel-flame interface until at late times when there is a distortion of the stable interface due to inertia (figs. 5.1 m).

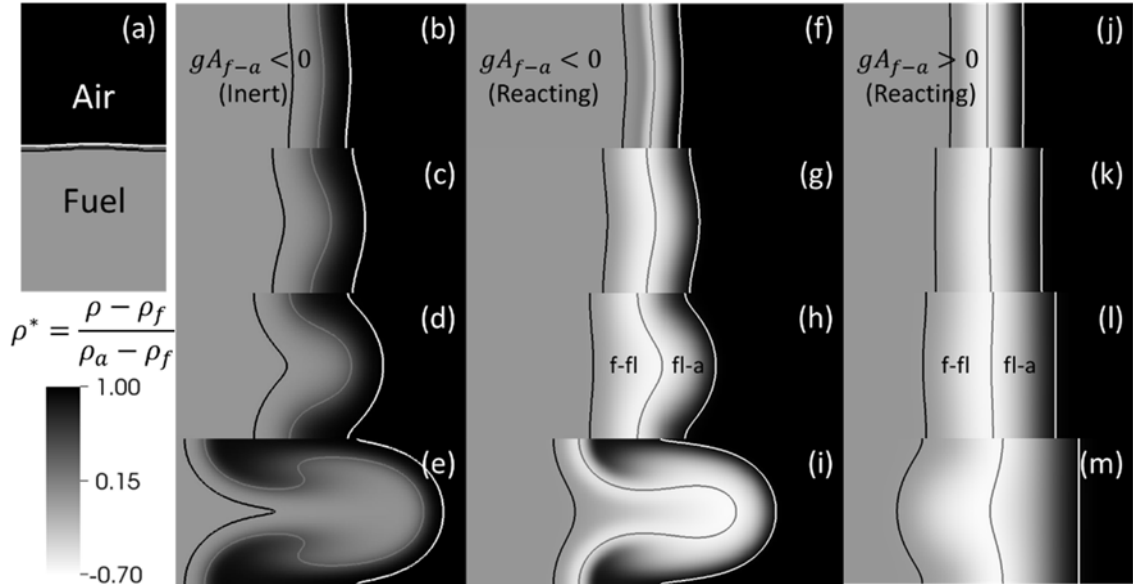


FIGURE 5.1: Low A interface evolution represented by scaled density in (b-e) inert (case 14), globally (f-i) unstable (case 15) and (j-m) stable (case 16) reacting (with 3<sup>rd</sup> layer) RT unstable interfaces realized at scaled times  $\tau = 2, 4, 6$  and  $10$  respectively. The initial interface is shown in figure (a) while iso-contours of fuel(black), flame-sheet(gray) and air(white) surfaces are overlaid on scaled density.

Globally unstable ( $gA_{f-a} < 0$ ) flame (figs. 5.1 f-i): Following ignition, the enhanced diffusive transport is responsible for flame thickening and reduced growth of the unstable flame sheet ( $Z_{st}$ ). Once again, the flame sheet continues to grow asymmetrically but in this case towards the air stream (figures 5.1 g-i) dictated by the growth of the corresponding unstable flame-air ( $A_{fl-a} = 0.38$ ) interface. The growth of the fuel surface (locally stable) is arrested until it is breached by the advancing (figure 5.1 g-h) flame sheet. Thereafter, the fuel surface continues to grow (figure 5.1 i) under the influence of the unstable flame-air interface, and the flow is globally unstable at late times. Thus, the formation of the bilayer renders the fuel surface stable over a timescale

$$\tau_{stable} \propto \frac{s_d}{h_{z_{st}}} \sqrt{A^* g k}, \quad (5.1)$$

where  $s_d$  is the characteristic separation distance between fuel and stoichiometric surfaces that the flame sheet must traverse before interacting with and affecting the fuel surface (discussed below).

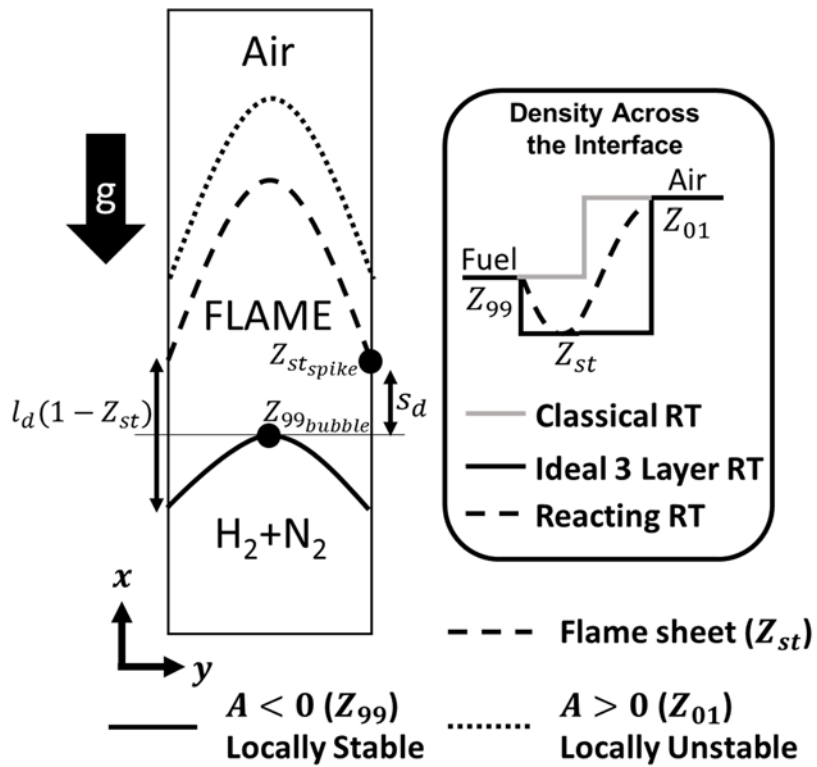


FIGURE 5.2: Schematic representation of the formation of the third layer in a low Atwood number, fuel-air mixture with a locally stable fuel-flame and locally unstable flame-air interfaces.

Stability duration model: In a globally unstable ( $gA_{f-a} < 0$ ) non-premixed flame, the fuel surface remains stable ( $Z_{99}$ ) over a duration  $\tau_{stable}$  given by eq. (5.2). In such a scenario (fig. 5.2), the density varies smoothly across the burning interface with an inflection point at  $Z = Z_{st}$  (flame sheet) where it reaches a local minimum. Thus, the sorting of the density stratification in cases 15-16 are fundamentally different from both non-reacting RT and a classical three-layer problem in which the intermediate layer is occupied by a passive scalar. In figure 5.2, we schematically compare the density ( $\rho$ )

stratification across a low A flame with classical (non-reacting) two-layer and three-layer RT configurations (studied previously by [113]). For the reacting RT, the flame sheet ( $Z_{st}$ ) is located at a distance of  $l_d(1 - Z_{st})$  (fig. 5.2) from the locally stable ( $gA_{f-fl} > 0$ ) fuel surface ( $Z_{99}$ ), where  $l_d$  is distance between the fuel and air streams. Subsequently, the fuel surface will exhibit a period of stability until downward spikes associated with the flame sheet ( $Z_{st_{spike}}$ ) breach the fuel bubble surface ( $Z_{99_{bubble}}$ ). The flame sheet spike front must travel a separation distance  $s_d = x_{Z_{st_{spike}}} - x_{Z_{99_{bubble}}}$  before it can destabilize the fuel surface, following which the fuel surface will grow driven by the inertia of the unstable flame-air interface. Thus, the single-mode globally unstable reacting RT flame will exhibit partial stability of the fuel surface for a duration of

$$\tau_{stable} \approx \frac{s_d}{\dot{h}_{Z_{st}}} \sqrt{Agk} - \tau_{ign}, \quad (5.2)$$

where  $\dot{h}_{Z_{st}} = dh_{Z_{st}}/dt$  is the growth rate of the flame sheet.

In figure 5.3, we plot the scaled fuel and flame sheet amplitudes for the globally unstable interface (case 15) against scaled time. The amplitudes are inferred as the distance between the peaks of the  $Z_{99}$  and  $Z_{st}$  iso-contours respectively. Also plotted is the separation distance ( $s_d$ ) that the unstable spike front associated with the flame sheet must travel before breaching the stable fuel surface. Initially, diffusive broadening ( $\sim\sqrt{t}$ ) dominates over RT growth ( $\sim e^t$ ) so that  $s_d$  increases. The fuel-air interface ignites at  $t_{ign} = 0.34 \text{ ms}$ , ( $\tau_{ign} \approx 1.8$ ) in this diffusion dominated growth phase, and the resulting flame forms an active third layer that renders the fuel surface locally stable. Following this, the growth of the fuel surface ( $Z = Z_{99}$ ) stagnates, while the flame sheet continues to grow under the influence of RT unstable flame-air interface. The spike tip of the flame sheet

advances towards the stable fuel surface thereby countering the diffusive broadening (which is enhanced by flame conditions). The flame formation increases the Atwood number ( $A_{fl-a} \approx 2 A_{f-a}$ ) driving the flow and also contributes to  $s_d$  through the increased mass diffusion. Eventually, ( $\tau \geq 6$ ) RT growth ( $\sim e^t$ ) of flame surface ( $Z_{st}$ ) dominates, thereby rapidly decreasing the separation distance. The spike tip of the advancing flame sheet breach the fuel surface at  $\tau \sim 10$  marked by  $s_d \approx 0$ . Following this ( $s_d < 0$ ) the fuel surface grows, driven by the inertia of the advancing flame sheet spikes.

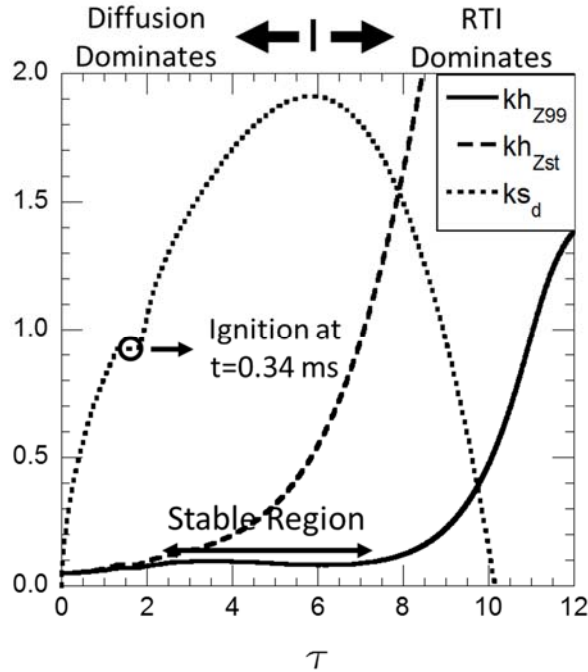


FIGURE 5.3: Scaled separation distance ( $ks_d$ ) and amplitude ( $kh$ ) of the fuel ( $Z_{99}$ ) and flame sheet ( $Z_{st}$ ) surfaces plotted against scaled time ( $\tau = t\sqrt{A^* gk}$ ) obtained from simulations with  $\lambda = 0.5$  cm and  $g = 0.6 \times 10^4 g_0$  for  $A_{f-a} = 0.2$  reacting interface.

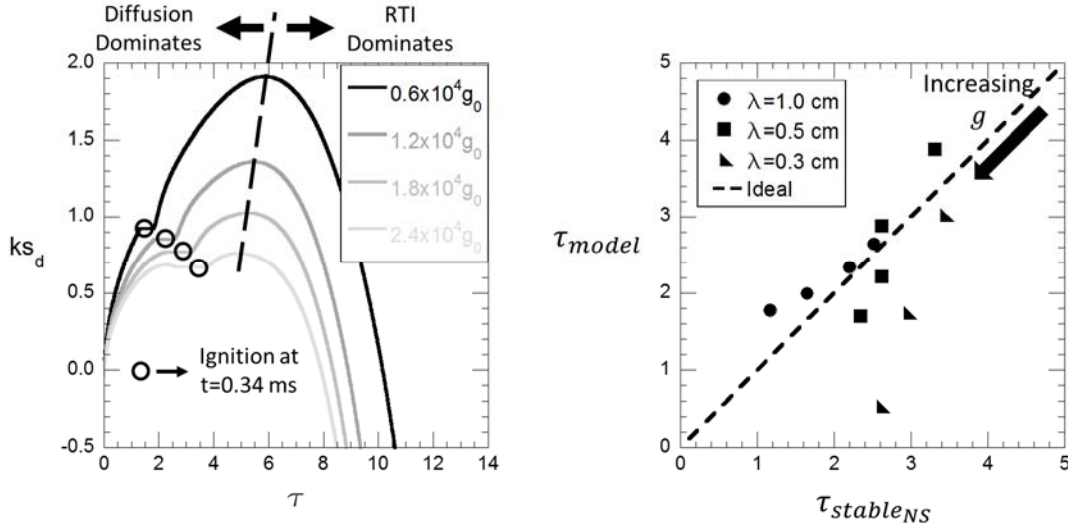


FIGURE 5.4: (a) Effect of imposed acceleration on the scaled separation distance: Plot of  $(ks_d)$  against scaled time  $(\tau = t\sqrt{A^*gk})$ . (b) Fuel surface stability durations as predicted by equation (5.2) and observed in numerical simulations (NS).

The separation distance may be viewed as a measure of the competition between the diffusive thickening (increases  $s_d$ ) and RT growth (decreases  $s_d$ ) of the interface. Thus, by increasing  $g$ , the transition to RT-dominated growth phase can be accelerated. In figure 5.4, we plot the scaled separation distance  $(ks_d)$  against scaled time from simulations with  $\lambda = 0.5$  cm (cases 15, 20-22). For all the single-mode cases presented in figure 5.4(a), the initial perturbation amplitude was specified to be  $h_0 = 0.05/k$ . Note that the higher initial amplitude also results in a faster transition to RT-dominated growth phase. Ignition of the fuel-air mixture is purely a thermo-chemical phenomenon, so that the ignition delay time  $t_{ign}$  is unaffected by the imposed gravity. However, the scaled time at ignition  $\tau_{ign} \approx t_{ign}\sqrt{A^*gk}$  varies quadratically with imposed acceleration ( $g$ ) and is indicated in fig. 5.4(a). As a consequence, with increasing  $g$  the flame and subsequent three-layer formation progressively shift towards the RT-dominated growth regime. The fuel surface ( $Z_{99}$ ) is considered to be stable over a time during which no net increase  $(\frac{d^2h_{z99}}{dt^2} \leq 0)$  in its growth

rate is observed in our simulation. We use the maximum post-ignition separation distance ( $s_d$ ) and the mean growth rate of the flame sheet for  $\tau_{ign} \leq \tau \leq \tau|_{s_d=0}$  in equation (5.2) to estimate the stability duration of the fuel surface. In figure 5.4(b), we compare the estimated duration of stability from eq. (5.2) with results from our numerical simulations for cases 7-10, 15, 20-25. Our simple scaling analysis shows excellent agreement with the simulation results over a wide range of  $g$  and  $\lambda$ . Note that slight disagreement for high  $g$  and smaller wavelength ( $\lambda = 0.3 \text{ cm}$ ) case is a consequence of ignition in RT dominated ( $s_d \rightarrow 0$ ) interface growth phase.

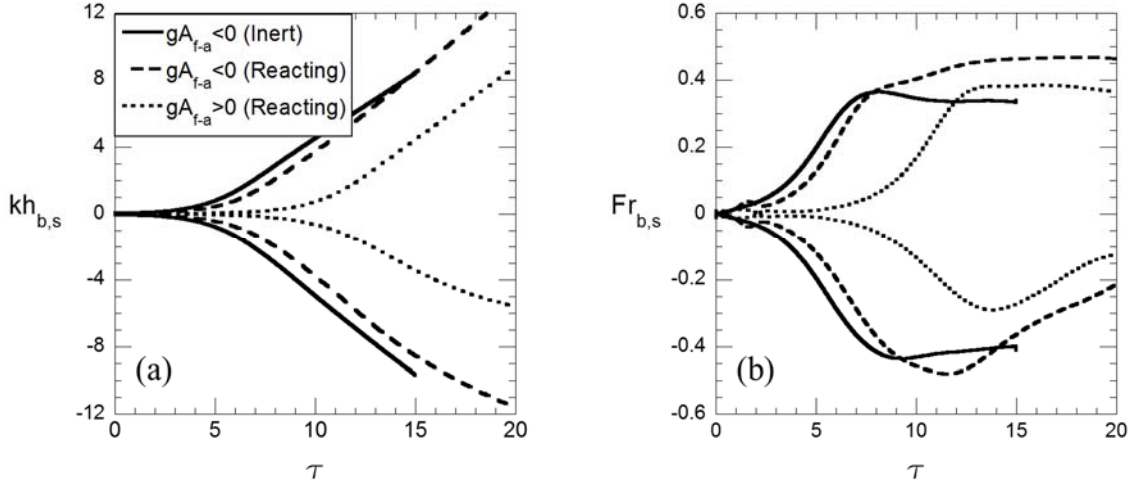


FIGURE 5.5: (a) Scaled bubble and spike amplitudes and corresponding (b) Froude numbers for reacting and non-reacting single mode interfaces ( $A = 0.2$ ) against scaled time ( $\tau = t\sqrt{A^*gk}$ ).

We quantify bubble (spike) amplitudes and corresponding Froude numbers by tracking the peaks and valleys of an isocontour of mixture fraction. The three layer RT flames discussed here are partially stable such that the change in stability (going from  $Z_f = Z_{99}$  to  $Z_a = Z_{01}$ ) occurs at  $Z = Z_{st} \approx 0.45$ . The iso-contour of  $Z_{50}$  (tracked earlier for two-layer RT) may lie in a locally stable density stratification, and hence may no longer be a suitable metric for instability growth in the corresponding three-layer problem. The

rationale behind the use of the  $Z_{50}$  level for the two-layer RT was based on tracking an iso-contour that is centrally located over the range corresponding to unstable density stratification in  $Z$ -space. For the three layer reacting interface, the unstable density stratification spans either  $Z_{st} \geq Z_a \approx Z_{01}$  (flame-air for globally unstable,  $gA_{f-a} < 0$ ) or  $Z_{st} \leq Z_f \approx Z_{99}$  (fuel-flame for globally stable,  $gA_{f-a} > 0$ ). As a result, we track the iso-contour of  $Z_{unstable} = \frac{Z_{st} + Z_{a(f)}}{2} \approx Z_{23}(Z_{73})$ , centrally located in unstable  $Z$ -space for globally unstable (stable) RT flames. Note that for the inert interface we track  $Z_{unstable} = Z_{50}$ . In figure 5.5 (a) we plot the evolution of scaled bubble ( $kh_b$ ) and spike amplitudes ( $kh_s$ ) for inert and reacting interfaces from cases 15-16 and based on the  $Z_{unstable}$  level. The corresponding Froude numbers are plotted in figure 5.5 (b). Following a short linear growth (symmetric and exponential in time), the inert interface undergoes nonlinear saturation (constant terminal bubble velocity). At late times ( $\tau \geq 8$ ), the low A bubbles and spikes attain a terminal velocity marked by a constant Froude number (see figure 5.5b) that is within 7% of eqs. 4.4-4.5. For the globally unstable flame, enhanced diffusion resulting in ignition and subsequent flame formation is responsible for a slight reduction of growth rates during the linear regime. The reacting bubbles attain larger terminal velocities much later ( $\tau \geq 12$ ) than the inert counterparts. The observed bubble Froude number is within 6% of the modified drag-buoyancy model for a positively buoyant flame (eq. 4.10), while underpredicting the flame expansion model (eq. 4.7) by  $\sim 30\%$ . For the globally stable RT flame (case 16), following ignition the Atwood number driving the flow is  $A_{f-fl} = \frac{\rho_{fl} - \rho_f}{\rho_{fl} + \rho_f} \approx 0.2$ , while diffusion enhancement following ignition is unchanged from the globally unstable case. As a result, the growth of the globally stable RT flame in fig. 5.5 is

significantly suppressed initially resulting in a prolonged ( $\tau_{ign} < \tau < 10$ ) linear regime ( $kh \approx 1$ ). Eventually ( $\tau \geq 13$ ), through the nonlinear saturation of the growing RT flame, the globally stable bubbles once again attain a constant Froude number but  $\sim 10\%$  smaller than corresponding globally unstable flame.

The local stability of the globally stable/unstable RT flames complicates the evolution of unstable spikes in each case. At late times, the spikes for the two reacting interfaces advance towards a locally stable surface. For the globally unstable (stable) flame, the Atwood number corresponding to the stable surface is half (twice) of the advancing spike. Thus the resistance to advancing spikes in globally unstable (stable) flame by locally stable surface is weak (strong). As a consequence, the peak spike growth for globally stable flame is  $\sim 35\%$  smaller than the globally unstable flame, following which  $Fr_s$  decays for the two flames. The late-time decay in spike growth is attributed to the loss of momentum associated with the interaction with the locally stable surface (fuel/air for globally unstable/stable interface).

## 5.2 Multimode Perturbation

We now discuss the implication of flame-generated three-layer density stratification on an interface initialized with multimode perturbations. The RT flame dynamics is schematically presented in fig. 5.6 for globally (a) unstable and (b) stable fuel-air interfaces alongside the (c) scaled density ( $\rho^*$ ) stratification across an unperturbed burning interface from our 1D calculations. The behaviour of the RT flame depicted schematically in fig. 5.6 may be understood in terms of a corresponding three-layer, non-reacting RT system [113]. For instance, [113] investigated through detailed experiments the dynamics of globally-stable ( $A_{bottom-top}g > 0$ ) and -unstable ( $A_{bottom-top}g < 0$ ),

non-reacting three-layer systems, with a constant, intermediate layer thickness of  $s_d$ . Note that for all these experiments,  $g < 0$  and  $A_{bottom-top}$  was varied such that  $\rho_{middle} < \rho_{bottom}$ . For either configuration, the early-time amplitude of the unstable interface is small compared to the layer thickness  $s_d$ , so that the stable interface is unaffected by the evolution of the corresponding unstable interface above it. However, at late times, when the amplitude of perturbations at the unstable interface approaches  $s_d$ , the evolution of the stable interface is affected by the development of the unstable interface and the global stability of the system, i.e.  $sgn(A_{bottom-top}g) < 0$ . For a globally stable or neutral system ( $A_{bottom-top}g \geq 0$ ), the stable interface resists the growth of the unstable interface in its direction, thereby partially penetrating/eroding the bottom fluid. Furthermore, the degree of erosion/penetration decreases as the density contrast between the bottom and top layer was increased ( $|A_{bottom-top}|$ ) [113]. In contrast, for a globally unstable system ( $A_{bottom-top}g < 0$ ), the mixing from the unstable interface eventually increases the density of the intermediate layer above that of the lower fluid, which renders the initially stable interface, RT unstable. Subsequently, the flow problem may be represented by the classical two-layer, single-interface RT growth. In the case of the reacting RT, the flame region exhibits behaviour similar to the corresponding non-reacting three layer problems described above, but with two important distinctions: (a) The intermediate layer (reaction zone) density is not uniform but varies smoothly across the f-a interface (fig. 5.6 c) and (b) the thickness of the flame ( $s_d$ ) is not constant and grows over time. Since the flame region is continuously replenished, the three-layer configuration is sustained such that a reacting, globally unstable system exhibits characteristics of a non-reacting globally stable system (discussed below).

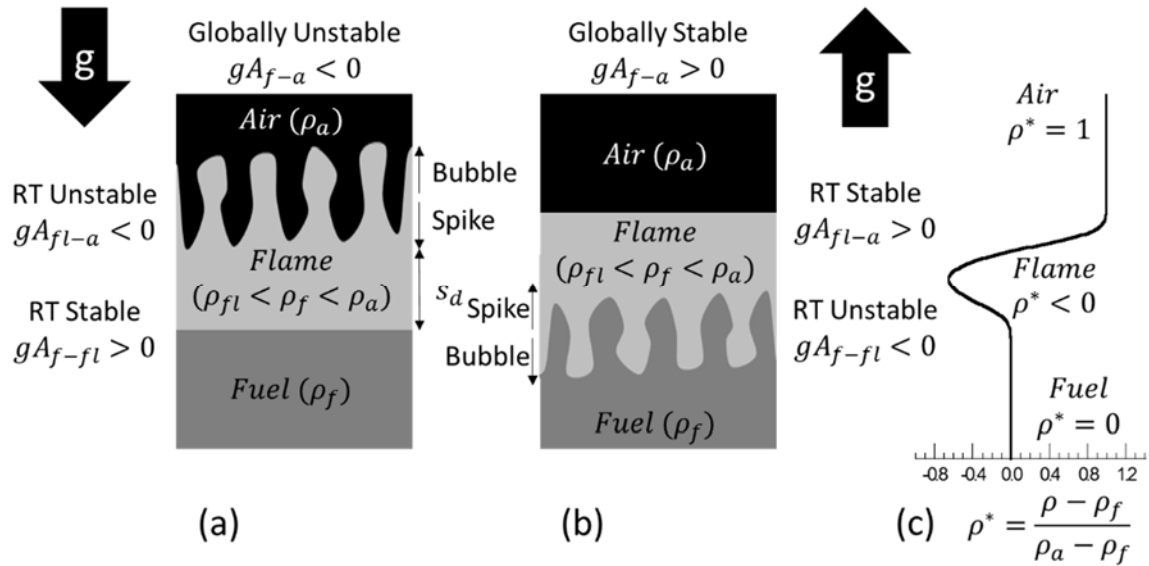


FIGURE 5.6: Schematic of a (a) globally unstable ( $gA_{f-a} < 0$ ) and (b) globally stable ( $gA_{f-a} > 0$ ) three layer RT configuration induced by the flame for  $A_{f-a} = 0.2$ . (c) The scaled density profile ( $\rho^*$ ) obtained from an unperturbed 1D simulation.

Globally Unstable Flame ( $A_{f-a}g < 0$ ): For  $A_{f-a}g < 0$ , the initial  $f$ - $a$  interface is RT unstable (we refer to this configuration as globally unstable). The prescribed modes on the interface grow linearly accompanied by diffusive broadening of the interface resulting in a combustible mixture that lines the perturbed interface. Such a perturbed  $f$ - $a$  interface auto-ignites at  $t = t_{ign}$  and subsequently forms a 3-layer configuration (fig. 5.6 a). Thus, the  $f$ - $fl$  interface is locally RT stable while the  $fl$ - $a$  interface is RT unstable. The modes on the  $fl$ - $a$  interface continue to grow such that positively buoyant bubbles associated with the flame rise against gravity, while spikes descend towards the stable fuel-flame interface. Eventually, downward spikes encounter the stable interface, which they will displace due to inertia.

Globally Stable Flame ( $A_{f-a}g > 0$ ): When the imposed acceleration is reversed ( $A_{f-a}g > 0$ ), the original  $f-a$  interface is RT stable. Thus, initial perturbations at this stable interface are gradually consumed by diffusive broadening, followed by ignition at  $t = t_{ign}$ . The resulting combustible mixture and flame region reconfigure the initial bilayer problem into a globally stable three-layer stratification (fig. 5.6 b). The  $fl-a$  interface is RT stable, while the presence of the intervening layer of lower density within the flame renders the  $f-fl$  interface RT unstable. Thus, imposed modes on the  $f-fl$  interface will grow so that flame bubbles descend against gravity and towards the fuel stream, while spikes of the fuel ascend towards the stable air stream through the flame region.

In figure 5.7, we present qualitative features from three simulations involving a perturbed interface separating fuel-air streams: Case 28 refers to a non-reacting (RT unstable,  $A_{f-a}g < 0$ )  $f-a$  interface and serves as a baseline, while cases 29 and 30 correspond to configurations that are globally unstable and stable for  $t > t_{ign}$  respectively. We describe the growth of the reacting and non-reacting interfaces at scaled times  $\tau = |A^*gt^2 / L|$ , where  $A^*$  is the effective unstable Atwood number driving the flow.

For non-reacting RT,  $A^* = A_{f-a}$ , while for the reacting flow  $A^* = \begin{cases} A_{f-a}, t \leq t_{ign} \\ A_{fl-a}, t > t_{ign} \end{cases}$  for  $A_{f-a}g < 0$  and

$A^* = \begin{cases} A_{f-a}, t \leq t_{ign} \\ A_{f-fl}, t > t_{ign} \end{cases}$  for  $A_{f-a}g > 0$ , and is thus modified to represent the post-ignition ( $t \geq t_{ign}$ )

density contrast.

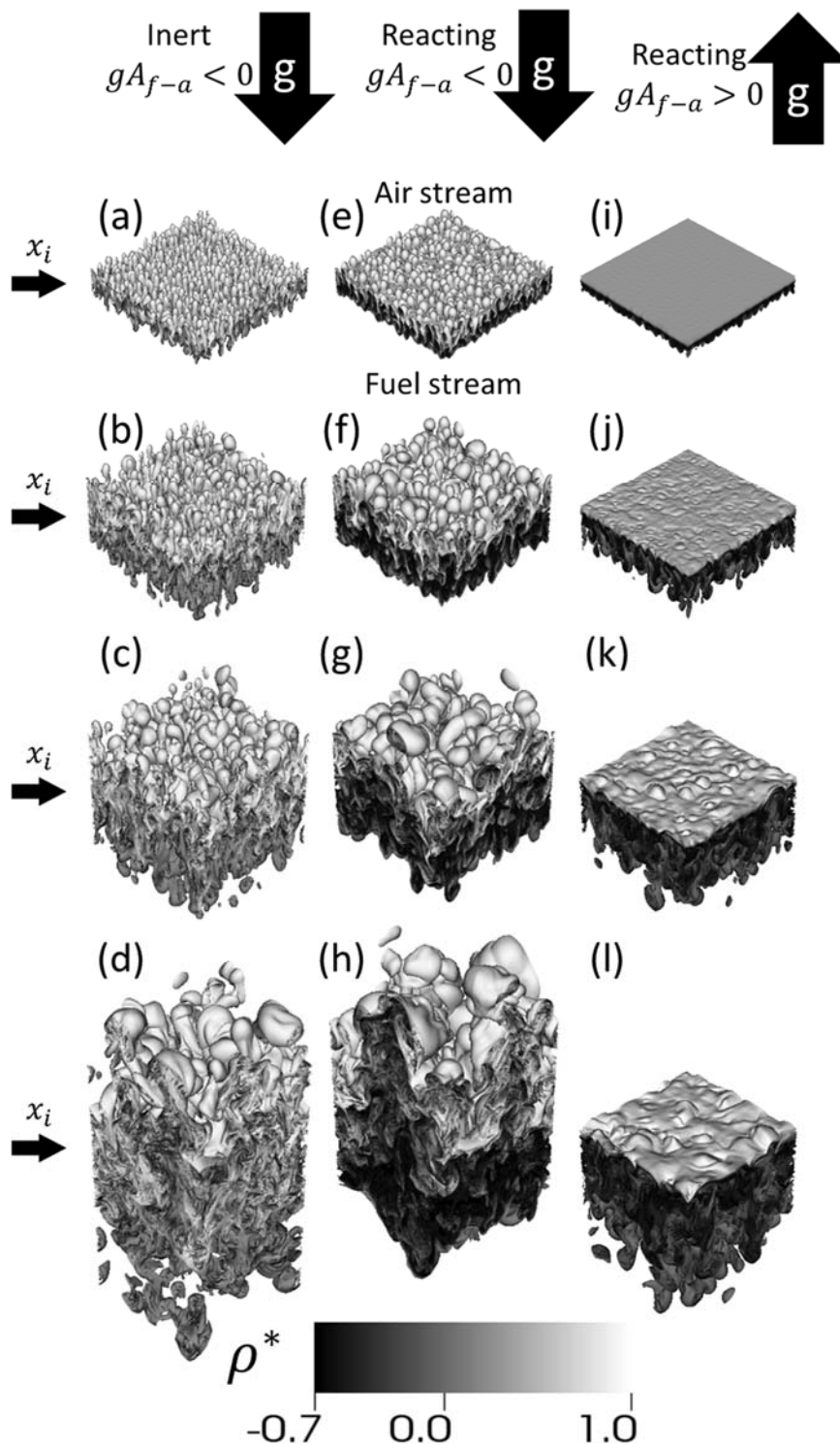


FIGURE 5.7: Isosurfaces of scaled density  $\rho^* = (\rho - \rho_f) / (\rho_a - \rho_f)$  from inert (left), and reacting interfaces with  $A_{f-a}g < 0$  (middle) and  $A_{f-a}g > 0$  (right column) at scaled times  $\tau = 1.6$  (a, e, i), 5.0 (b, f, j), 10.0 (c, g, k) and 19.0 (d, h, l). The initial interface location ( $x_i$ ) is indicated by horizontal arrows for each realization.

Non-reacting  $f-a$  interface (Case 28): At early times (fig. 5.7 a), prescribed modes grow linearly without interaction with their neighbors. During the subsequent self-similar growth regime ( $\tau > 5$ ), long-wavelength modes ( $\lambda$ ) are visible and have been formed through mode coupling of higher harmonics (figs. 5.7 b-d). Consistent with low Atwood number RT unstable interfaces [3], the bubble and spike fronts from this  $A^* = 0.2$  simulation exhibit symmetry well in to the self-similar turbulent stage (figs. 5.7 d).

Globally Unstable Flames (Case 29): Mass diffusion across the initial interface produces a fuel-air mixture that auto-ignites (at  $t = t_{ign} = 0.34$  ms), early in the linear stage ( $\tau \approx 0.02$ ) of instability growth. By  $\tau \approx 1.6$  (fig. 5.7 e), a hot ( $T \sim 2000\text{K}$ ), low-density flame ( $\rho^* < 0$ ) is formed and lines the interface. At this stage, the separation distance ( $d_s$ ) is of the order of perturbation wavelengths ( $\lambda$ ), so that the growth of the unstable interface is affected by the presence of the stable interface  $f-fl$ . Spikes from the unstable  $fl-a$  interface traverse the flame region and eventually breach the stable fuel surface (fig. 5.7(f)) at  $\tau = 5$ . The momentum transfer as a result of this collision with the stable surface results in a purely inertial growth/displacement of the low density fuel surface ( $\rho^*=0$ ). Through this mechanism, the descending spikes continue to transport air towards the fuel surface ( $\rho^*=0$ ), which mixes with the fuel stream to increase  $s_d$  upon combustion. In the self-similar regime (fig. 5.7 f-h), long wavelength modes are formed while the separation distance between the layers continues to increase. As a result, asymmetric interpenetration of fuel and air streams is observed at late times (fig. 5.7 h).

Globally Stable Flames (Case 30): When the direction of acceleration is reversed, an initially RT-stable  $f-a$  interface upon combustion (fig 5.7 i) will render the fuel surface unstable ( $A_{f-fl}g < 0$ ). Similar to case 29, the flame surface lines the pre-ignition  $f-a$

interface, but then grows in the direction of the fuel stream. The subsequent growth of the  $f-fl$  interface transports fuel towards the stable  $fl-a$  interface, thereby increasing the thickness  $s_d$  of the inner layer (fig. 5.7 j-k) upon penetration into the air stream. The momentum transferred on collision by the ascending unstable spike growth in the linear stage (fig. 5.7 i-j) is insignificant to the displacement of the stable air surface ( $\rho^* = 0$ ) since  $\rho_a > \rho_f$ . In the self-similar regime, long wavelength modes formed through mode coupling eventually gain enough momentum to breach the mixing zone ( $\sim 2d_s$ ) and deform/displace (fig. 5.7 k-l) the air surface.

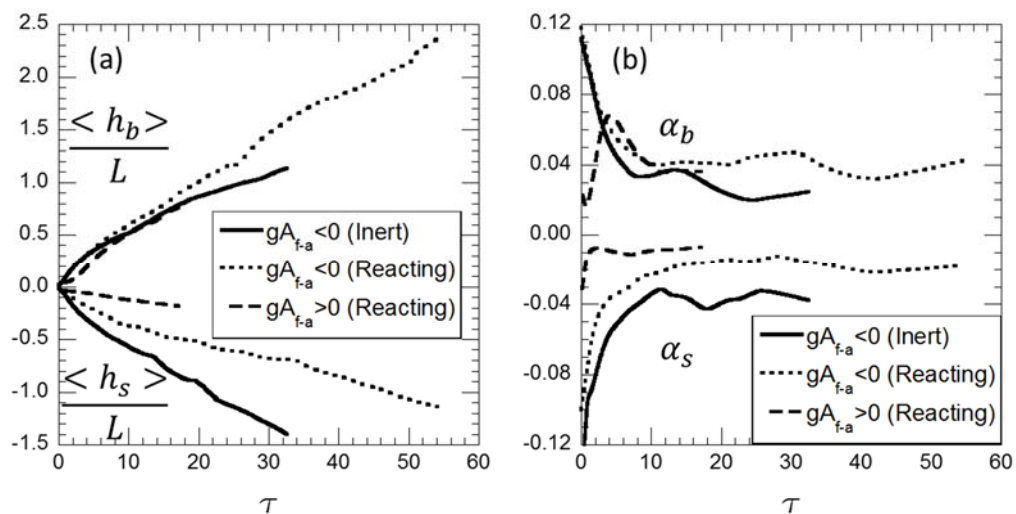


FIGURE 5.8: (a) Amplitudes of bubble and spike fronts scaled by box width ( $L$ ) and (b) corresponding mix growth rate ( $\alpha_{b,s}$ ) plotted against scaled time ( $\tau$ ) for cases 28-30.

We quantify the extent of bubble and spike penetration by tracking in time the x-location of the 1% (air) and 99% (fuel) planar-averaged ( $y$ - $z$ ) surfaces of mixture fraction ( $Z$ ). Note that for case 29 (30) the *global* bubble and spike fronts correspond to air (fuel) and fuel (air) surfaces respectively. In fig. 5.8 (a), we plot the non-dimensional global bubble and spike amplitudes ( $\langle h_{b(s)} \rangle / L$ ) against the scaled time ( $\tau$ ) from the reacting

and non-reacting simulations. The corresponding self-similar growth rates for bubble/spike fronts are obtained from  $\alpha_{b,s} = \frac{1}{L} \frac{d \langle h_{b,s} \rangle}{d\tau}$ , and shown in fig. 5.8 (b). For the non-reacting interface, following a short linear growth phase ( $0 < \tau < 5$ ), the flow achieves self-similarity characterized by a constant  $\alpha_b \approx 0.028 \pm 0.009$  consistent with previously reported values in [3]. For the globally unstable reacting interface ( $A_{f-a}g < 0$ ), bubble growth is enhanced to yield  $\alpha_b \approx 0.04 \pm 0.004$ , since the bubble front is driven by the increased density contrast (and  $A_{f-a}$ ) between the air stream and the newly formed flame region. Furthermore, the amplitude (fig. 5.8 (a)) and growth rates (fig. 5.8 (b)) of the spike front show relative stability in contrast to the corresponding inert case – thus  $\alpha_s$  displays a gradual decrease through the self-similar evolution. This is attributed to the stabilization mechanism discussed earlier where the descent of long-wavelength modes through the mixing layer experiences mechanical/turbulent stirring (turbulent diffusion) and subsequent breakdown before interacting with the stable fuel (spike) surface where their advance is arrested. Furthermore, modes with  $\lambda_b > s_d$  will successfully traverse the reaction zone, following which they eventually interact with the fuel (spike) surface. Thus, the duration of stability of the spike front will depend on  $s_d$  and the terminal velocity of the long wavelength structures ( $\sim \sqrt{\lambda_b} \sim \sqrt{h_b} \sim \sqrt{L}$ ), which eventually breach the turbulent mixing zone and dominate over a time scale of  $\tau \sim 1/\alpha_b \approx 25$ . This is followed by additional spike growth for  $\tau > 25$  (fig. 5.8 b) driven by inertia imparted by long wavelength structures ( $\sim L$ ) upon interaction with the stable surface. For the globally stable flame, the growth of modes associated with the unstable *f-fl* interface contribute towards

the global bubble (fuel surface) amplitude growth, albeit with a lower growth rate than cases 28 and 29. However, spikes remain stable through late times, so that the air (spike) surface displacement/growth is weak and dominated by diffusive broadening.

To quantify the effect of RT mixing on combustion, we describe the dynamics of the flame sheet, defined as the iso-surface of the stoichiometric mixture fraction ( $Z = Z_{st} = 0.45$ ). Since the flame sheet represents the most reactive surface within a diffusion flame, its surface area correlates with key combustion quantities [89,114-116] including the energy deposition rate and combustion efficiency. For an inert interface, the area of this surface (fig. 5.9) rapidly increases to  $\sim 9 L^2$  by the end of the linear stage, followed by a self-similar growth phase during which it evolves according to  $S_{Z_{st}} \approx \tau^{0.67}$ . Owing to spike-side stability, surface area growth of a globally unstable flame lags its non-reacting counterpart during the linear and the self-similar stage during which we observe  $S_{Z_{st}} \approx \tau^{0.41}$  (fig. 5.9). For case 30 (globally stable), the post-ignition flame sheet attains a significantly lower peak surface area ( $\sim 2L^2$ ), followed by negligible growth during the self-similar regime and is attributed to sustained late time stability of spikes for case 30. Thus, such a configuration may be exploited in high ‘g’ devices to attain a controlled and stable combustion process such that the flame surface area (hence heat release rate) is statistically independent of time.

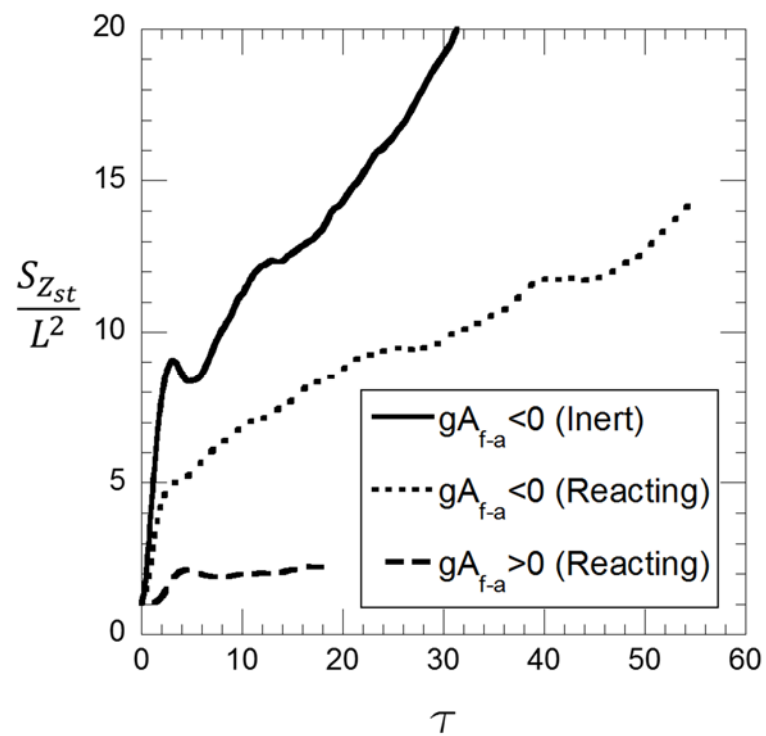


FIGURE 5.9: Plot of surface area of the flame sheet ( $Z_{st}$ ) scaled by the area of box cross section against scaled time ( $\tau$ ) for cases 28-30.

## CHAPTER 6: RICHTMYER-MESHKOV FLAMES

In this chapter we report on high-resolution, numerical simulations of a single-mode, chemically reacting, Richtmyer-Meshkov (RM) instability, at different interface thicknesses. The interface thickness was systematically varied in the simulations to study the effect of the total mass of fuel burnt and heat added on the hydrodynamic instability growth rates. The rest of the chapter is organized as follows: The numerical method and problem setup are described in section 6.1. The results are summarized in subsequent sections, and include description of shocked and unshocked 1D reacting fronts (no perturbation) in section 6.2, a 2D (perturbed) non-reacting RMI front with different interface thicknesses (section 6.3), a 2D (perturbed) unshocked reacting front (section 6.4), a 2D (perturbed) reacting, RMI front in section 6.5 and a 2D (perturbed) reacting RMI under reshock condition in section 6.6.

### 6.1 Problem Setup and Numerical Method

We consider the interaction of a Mach 1.2 shock with a sinusoidally perturbed  $H_2$  -  $O_2$  interface. The problem configuration is represented schematically in figure 6.1 (a) where the shock, initially located at  $x = x_s$ , travels to the right from  $H_2$  to  $O_2$ . We track the evolution of the mixture fraction  $Z$  defined as

$$Z \equiv \frac{sY_F - Y_O + Y_O^0}{sY_F^0 + Y_O^0} \quad (6.1)$$

where  $s$  is the mass stoichiometric ratio of the mixture,  $Y_F$  and  $Y_O$  are the mass fractions of the fuel and oxidizer respectively, and  $Y_F^0$  and  $Y_O^0$  are the fuel and oxidizer mass fractions in the corresponding pure streams. Thus, a mixture fraction of  $Z = 1$  corresponds to the presence of pure fuel and vice versa (figure 6.1 (b)). Note that for the  $H_2 - O_2$  configuration considered here,  $s = 8$ ,  $Y_F^0 = 1$  and  $Y_O^0 = 1$ , indicating that the mass fractions of  $H_2$  and  $O_2$  on the fuel and oxidizer streams are free from any dilution due to inert molecules ( $N_2, Ar$  etc). Furthermore, for a stoichiometric mixture,  $\frac{Y_{H_2}}{Y_{O_2}} = s = 8$ , hence  $Z = Z_{st} = 0.11$ . We also track the evolution of the surface  $Z_{50}$ , defined as the mixture fraction surface corresponding to  $Z = 0.5$ . Across the burning interface, the mixture fraction varies smoothly (and often monotonically), making it a reliable metric for comparing the non-reacting and reacting RM flows (for reacting flows, the consumption of fuel and oxidizer to produce products of combustion can cause localized discontinuities in the mass fraction profiles across the interface, making it difficult to track).

The material interface is initially at  $x_i$  (figure 6.1 (a)), and specified by an amplitude ( $h_0$ ) and thickness ( $\Delta$ ) through the mixture fraction  $Z$  according to:

$$Z(x) = 0.5(1 - \text{erf}[(x - x_i) \frac{W}{\Delta}]). \quad (6.2)$$

In Eq. 6.2,  $W$  is a scaling factor that ensures  $Z$  varies from a threshold value of  $\varepsilon$  to  $1 - \varepsilon$  over a width  $\Delta$ . Thus,

$$W = 2 |\text{erf}^{-1}(1 - 2\varepsilon)|. \quad (6.3)$$

For all the simulations reported here, we choose  $\varepsilon = 10^{-5}$ , corresponding to  $W \sim 6 \times 10^{-2} m$ . Note that [43] defined the thickness of the interface as the maximum slope thickness ( $\delta$ ) of the density profile, which corresponds in our framework to  $\approx \Delta / W$ . We prefer to use  $\Delta$  as the characteristic length scale in the specification of  $Z$  (rather than  $\delta$ ), since it represents the entire reaction zone including the extremities of the  $Z$  profile where burning can still occur.

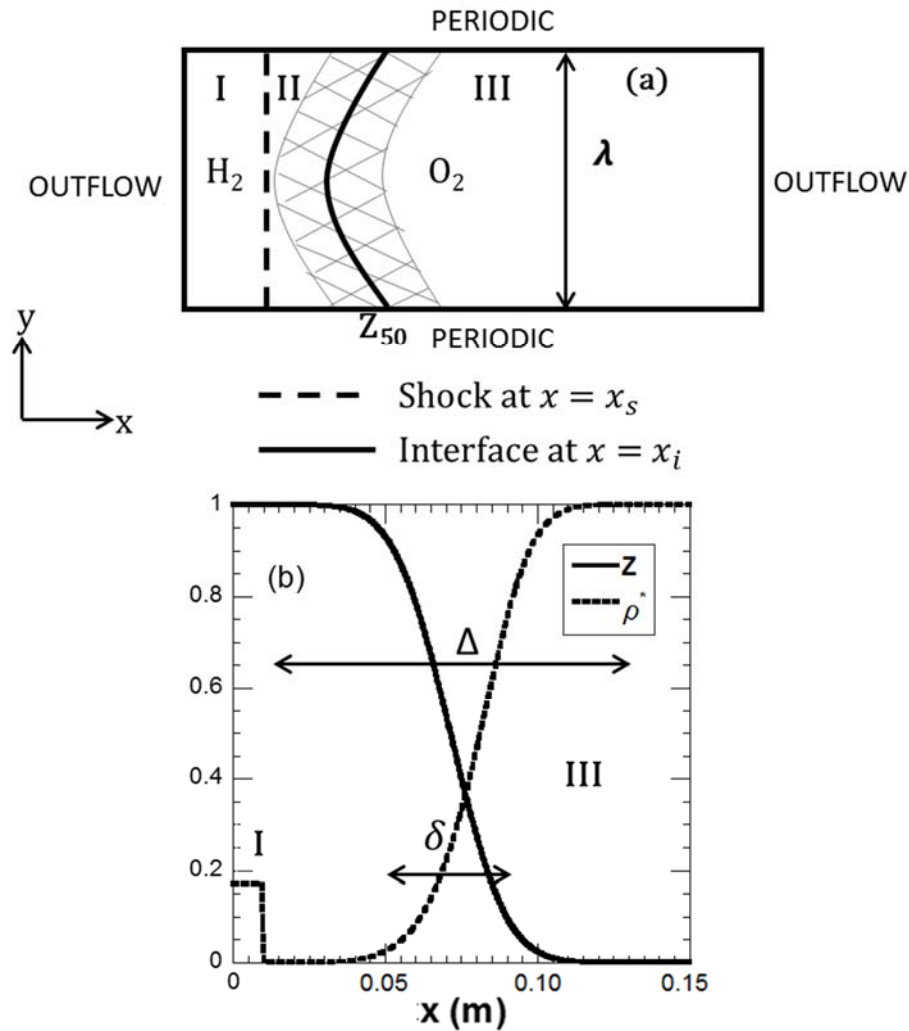


FIGURE 6.1: (a) Schematic of the problem setup and (b) x-profiles of the scaled initial density  $\rho^* = (\rho - \rho_{H_2}) / (\rho_{O_2} - \rho_{H_2})$  and mixture fraction ( $Z$ ) from 1D simulation with  $\Delta = 0.12$  m.

Perturbations at the interface are imposed according to

$$x_i = x_s + \frac{\Delta}{2} + h_0 \left\{ 1 - \cos\left(\frac{2\pi y}{\lambda}\right) \right\}, \quad (6.4)$$

where  $\lambda$  is the wavelength and  $x_s$  is the initial shock location. Thus, at  $t = 0$  the shock is positioned slightly ahead of the interface (figure 6.1 (a)), with which it interacts shortly thereafter. The initial gas densities were chosen to be  $\rho_l = \rho_{H_2} = 0.08 \text{ kg/m}^3$  and  $\rho_h = \rho_{O_2} = 0.24 \text{ kg/m}^3$ , so that  $A_i \approx 0.5$ , while a uniform pressure of 1 atm in regions II and III in figure 6.1 (a) was used. The initial temperatures in regions II and III were  $\approx 300\text{K}$  and  $\approx 1625\text{K}$  respectively, while the temperature in the interfacial region at atmospheric pressure is determined from the mixture density distribution  $\left( \rho_{mix} = \left( \frac{Y_{H_2}}{\rho_{H_2}} + \frac{Y_{O_2}}{\rho_{O_2}} \right)^{-1} \right)$  through the equation of state. The computations were performed in 2D, in a numerical shock tube with an aspect ratio of 12, employing a uniform grid of resolution  $\left( \frac{256}{\lambda} \right)$  in x and y directions, with  $\lambda = 6 \times 10^{-2} \text{ m}$ . The time step is restricted by a CFL condition, with  $\text{CFL} = 0.5$  for all the simulations reported herein. Outflow and periodic boundary conditions were enforced in x- and y-directions respectively, and no explicit diffusion was employed.

The simulations described in sections 6.2-6.6 were performed using the directionally split Piecewise Parabolic Method[56] in FLASH to solve the compressible Euler equations, while the temperature dependence of the specific heat of each species is represented as a polynomial function [66]. The  $H_2 - O_2$  chemical kinetics is modeled through the 9-species, 19-step reversible reaction mechanism of Billet[76] reduced from the detailed acetylene combustion mechanism of [77]. Billet[76] used this mechanism to

study the interaction of acoustic waves with circular and spherical hydrogen diffusion flames and for simulations of reactive shock-bubble interactions. The nine coupled species evolution equations were numerically integrated in time, using a variable order Bader-Deuffhard [64] method to handle the inherent stiffness of the ODE system.

While FLASH is capable of describing mass transport through a Flux-based method (where diffusive fluxes are updated at every timestep), or an Implicit solution of the diffusion equation, the simulations in this work were performed without any explicit treatment of mass diffusion. Note that even when the mass diffusion modules are turned off in FLASH, cell-averaged numerical mixing is present, leading to numerical diffusion of the above physical quantities. The resulting numerical diffusion is well-behaved, with properties that closely track the behavior of the physical counterpart [54,58,117,118]. Such simulations are categorized as Implicit Large Eddy Simulations (ILES), and are particularly suited to flows in which shocks and interfaces are present [2-4,25,35,119-122] (such as the flow studied here), since these methods preserve the monotonicity of the variables through flux limiting, preventing spurious overshoots and undershoots. We justify this omission by noting RM growth rates develop over the shock timescale, which is several orders of magnitude smaller than the diffusive timescales [82]. We performed numerical simulations with and without mass diffusion, and found large scale qualitative features as well as quantitative data (cross-profiles of species mass fractions, mixture fraction, and mix width) from both cases in close agreement. A detailed convergence study was performed, where the number of grid points spanning a single perturbation wavelength  $\lambda$  was varied as (64, 128, 256, and 512). For simulations with zoning in excess of  $128 / \lambda$ , we found the results are converged in terms of the gross features (perturbation amplitudes,

growth rates and mix widths), while the small-scale features retain some grid dependence as expected.

The interaction of a shock with a material interface with burning is complicated by several factors including the (i) shape of the interface ( $h_0, \lambda, \Delta$ ), (ii) physical and thermodynamic properties of the gases on either side of the interface, (iii) incident shock properties and (iv) thermo-chemical properties of the mixture across the interface. We have attempted to study these coupled phenomena through a series of increasingly complex numerical simulations. The objective is to understand the properties of the reacting RM front in the linear regime. To this end, we have performed simulations of the 1D (unperturbed) non-reacting, and reacting fronts (section 6.2), 2D (perturbed) non-reacting, RM flow with different  $\Delta / h_0$  (section 6.3), 2D (perturbed) reacting, unshocked, front with different  $\Delta / h_0$  (section 6.4), and a 2D (perturbed), reacting RM (shocked) ( section 6.5) and reshocked (section 6.6) fronts. For clarity, we summarize in table 6.1 the simulations performed in this work.

TABLE 6.1: Summary of simulations performed to characterize RM flames.

Sections	Case	$Ma_i$	$kh_0$	Burn	Reshock	$\Delta$
6.2	31-32	-	0.0	Yes	No	$3.8 \times 10^{-3}, 0.12 m$
	33	1.2	0.0	No	No	$3.8 \times 10^{-3} m$
	34-35	1.2	0.0	Yes	No	$3.8 \times 10^{-3}, 0.12 m$
6.3	36-41	1.2	0.2	No	No	$2 - 64h_0$
6.4	42-48	-	0.2	Yes	No	$2 - 80h_0$
6.5	49-54	1.2	0.2	Yes	No	$2 - 64h_0$
6.6	55	1.2	0.2	Yes	Yes	$2h_0$

## 6.2 Unperturbed Interfaces (cases 31-35)

In this section, results are presented from two sets of simulations with an unperturbed interface. The first set describes the burning of a sharp and a diffuse interface in the absence of an incident shock (cases 31-32), while the second set involves an incident

shock traversing an interface where burning occurs (cases 34-35). The simple configurations involving flat interfaces described herein are useful in interpreting the perturbed interface simulations described in sections 6.3 – 6.6. The sharp and diffuse interfaces are initialized with thicknesses of  $3.8 \times 10^{-3}$  m and 0.12 m respectively, and are specified according to Eq. 6.4 with  $h_0 = 0$ . The fuel/oxidizer mixture across the interface is consumed according to the reaction kinetics dictated by Billet[76], while products are formed across the interface. The chemical reactions are accompanied by heat addition at the interface, resulting in a spontaneous pressure rise, with the maximum pressure observed at the location where  $Z \approx 0.04$  in our simulations. Note that in our simulations, the temperature towards the (lean) oxygen side is higher and thus ignition first occurs in this region ( $Z \approx 0.01$ ), followed by burning along the rest of the interface. In the unshocked simulation, this initial pressure rise subsequently divides into two combustion waves, one of which moves towards the fuel ( $H_2$ ) side of the interface and the other towards the oxidizer ( $O_2$ ). The leftward wave moving towards the fuel imparts a net negative velocity to the interface, defined as the coordinate position ( $x$ ) where the mixture fraction crosses 50%. The  $x - t$  diagrams of the sharp and diffuse unshocked interfaces are shown in figure 6.2 (a), while the corresponding velocities ( $dx / dt$ ) are plotted in figure 6.2 (b). For a sharp interface, the amount of fuel and thus the heat addition across the interface is small, resulting in a peak negative interface velocity  $\approx -40$  m/s, following which the flame achieves steady state by  $t \approx 0.1$  ms. In contrast, with a significant amount of fuel across the diffuse interface, the substantial heat addition during burning results in significant pressure rise accelerating the interface to a peak negative velocity  $\approx -280$  m/s while the flame achieves steady state by  $t \approx 1.0$  ms.

For the diffuse flame, we plot cross-stream profiles of the scaled pressure

$$p^* = \frac{p - p_0}{p_s - p_0}, \text{ density } \rho^* = \frac{\rho - \rho_l}{\rho_h - \rho_l}, \text{ temperature } T^* = \frac{T - T_l}{T_h - T_l}, \text{ and mixture fraction (Z)}$$

in figures 6.3 (a) - (d) respectively at different times. Note that we use for  $p_s \approx 0.16$  MPa, the maximum pressure across the interface observed in our simulation at  $t = 15 \mu\text{s}$ . The Mach number corresponding to this pressure rise was estimated to be  $\approx 1.23$  from

$$Ma = \sqrt{1 + \left(\frac{p}{p_0} - 1\right) \left(\frac{\gamma + 1}{2\gamma}\right)}. \quad (6.5)$$

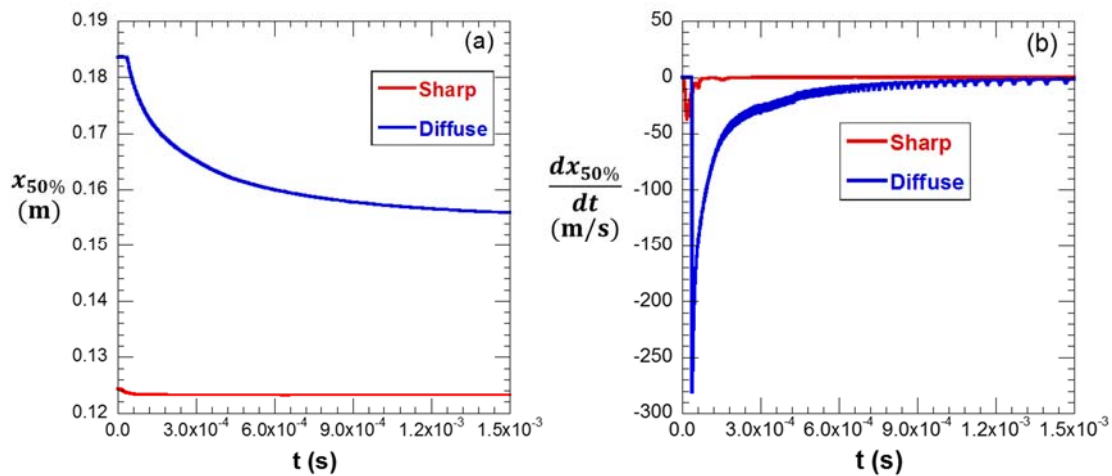


FIGURE 6.2: (a) Interface position and (b) the corresponding velocity as a function of time from 1D simulations of a reacting front without an incident shock. Results are shown for both a sharp ( $\Delta = 3.8 \times 10^{-3}$  m) and diffuse ( $\Delta = 0.12$  m) front.

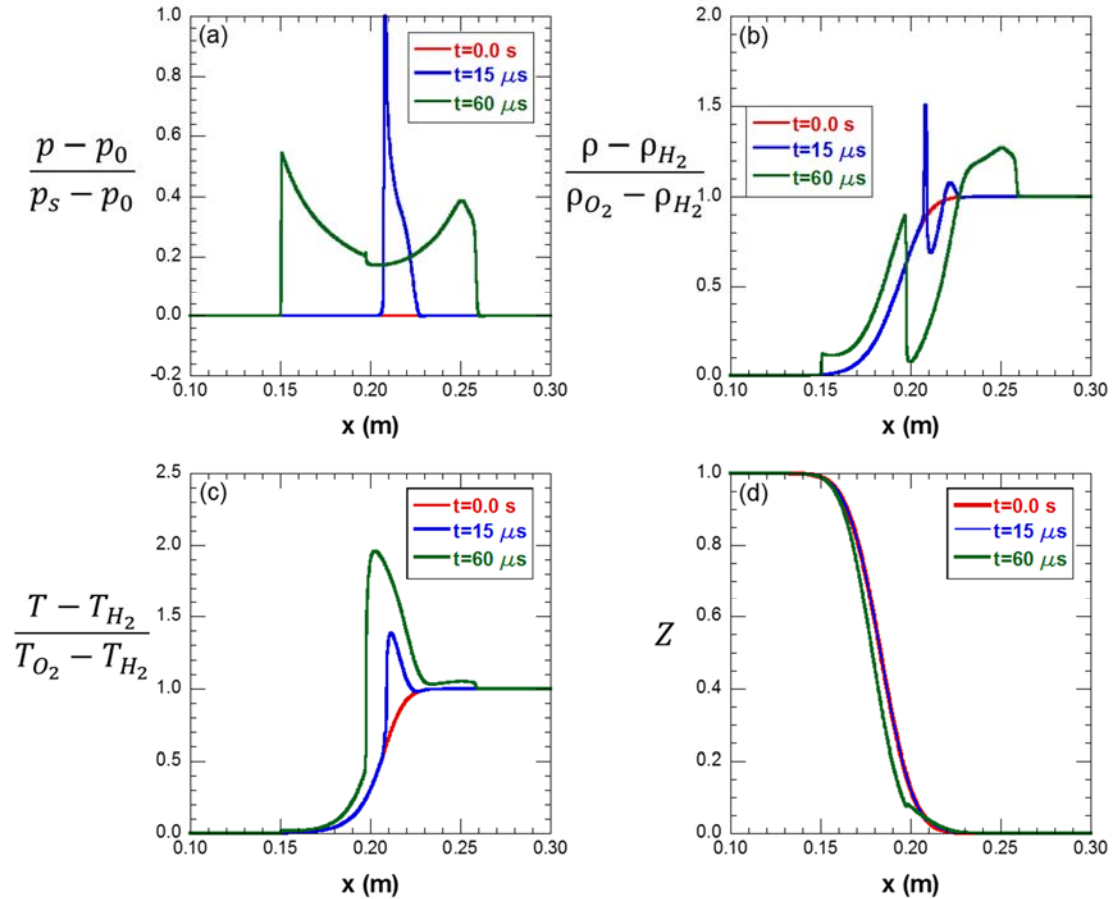


FIGURE 6.3: Axial profiles of the scaled (a) pressure, (b) density, (c) temperature, and (d) mixture fraction at times 0 s, 15  $\mu\text{s}$ , and 60  $\mu\text{s}$  from 1D simulations of a reacting front without an incident shock, and with  $\Delta = 0.12$  m.

At  $t = 60 \mu\text{s}$  (figure 6.3 (a)), the splintering of the combustion wave into two waves traveling in opposite directions can be observed. The leftward (towards  $H_2$ ) and rightward waves (towards  $O_2$ ) were observed to have Mach numbers of  $\approx 1.13$  and  $\approx 1.09$  respectively (based on the pressure jump across each front seen in figure 6.3 (a)). The maximum temperature achieved by the flame is  $\approx 3050$  K (at  $x|_{Z_{st}=0.11}$ ) in good agreement with [93] for an initial stoichiometric mixture at  $\approx 780$  K. The two combustion waves moving in opposite directions result in localized stretching of the interface in the heat release zone ( $\approx 0.19 - 0.23$  m), where the profile of the mixture fraction no longer

resembles the initial error function. Furthermore, the density within this region decreases due to heat addition, eventually falling below the density of the light fluid ( $H_2$ ) at late time ( $t \approx 1.5$  ms), while pressure in the domain relaxes to atmospheric ( $p_0$ ).

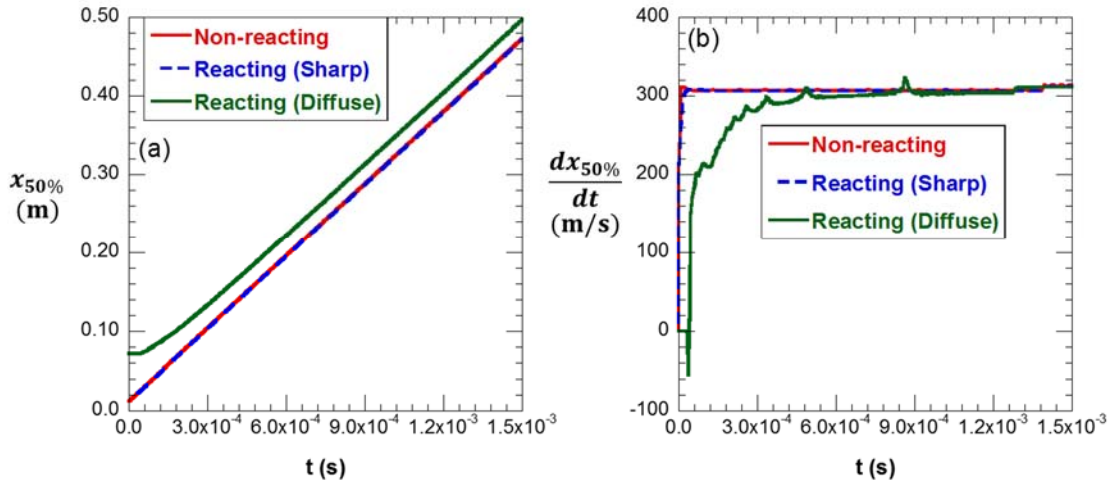


FIGURE 6.4: (a) Interface position based on  $Z_{50}$  and (b) the corresponding velocity as a function of time from 1D simulations of a reacting front with a Mach 1.2 incident shock. Results are shown for both a sharp ( $\Delta = 3.8 \times 10^{-3}$  m) and diffuse ( $\Delta = 0.12$  m) front, as well as for the baseline non-reacting (*cold*) front.

We now describe the development of such sharp and diffuse reacting interfaces when subjected to shock impingement. To establish a baseline for comparison, we show as the red line in figure 6.4, the trajectory of an *unperturbed, non-reacting* interface that is accelerated by an incident shock. Also shown in figure 6.4 are results from simulations with a *shocked reacting front*, with both sharp and diffuse initial interfaces. The  $x$ - $t$  diagrams of the non-reacting and reacting shocked interfaces are shown in figure 6.4 (a), while the corresponding interface velocities ( $dx/dt$ ) are plotted in figure 6.4 (b). For a sharp interface, the behavior of the reacting 1D shocked front is indistinguishable from its cold flow counterpart, and shows the interface is rapidly accelerated (over a shock-interaction timescale) to a constant velocity of  $\sim 300$  m/s (figure 6.4 (b)), in agreement with the solution of the Rankine-Hugoniot equations [34]. For the diffuse interface, there

is significant burning across the interface in this non-premixed flame, resulting in transients that delay the approach to the asymptotic interface velocity (figure 6.4 (b)). We attribute this time delay to the combustion waves that form in response to the rise in temperature in the reaction zone (and described above), producing a net negative particle velocity across the interface.

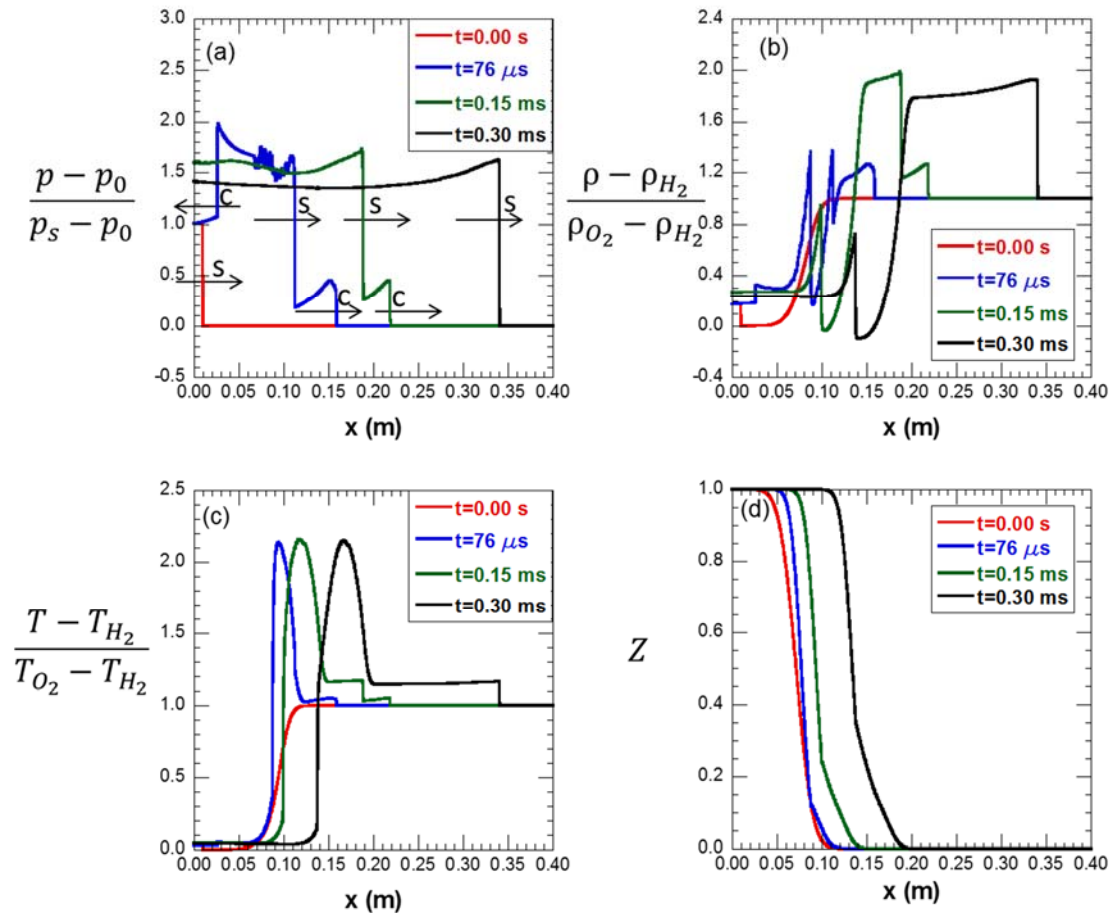


FIGURE 6.5: Axial profiles of the scaled (a) pressure, (b) density, (c) temperature, and (d) mixture fraction at times 0 s, 76  $\mu\text{s}$ , 0.15 ms and 0.3 ms from 1D simulations of a reacting, diffuse ( $\Delta = 0.12$  m) front with a Mach 1.2 incident shock.

The cross-stream profiles of the scaled pressure, density, temperature, and mixture fraction ( $Z$ ) are shown in figures 6.5 (a) - (d) for the shocked, diffuse flame at  $t = 0$  s, 76  $\mu\text{s}$ , 0.15 ms, and 0.30 ms respectively. For the highly diffuse interface considered here,

there is significant pressure rise resulting from burning at the interface, and is marked in figure 6.5 (a) as the combustion wave ‘c’. In the same figure, the label ‘s’ indicates the location of the incident shock, along with arrows denoting the direction of travel of each wave. Initially, the combustion waves travel away from the interface moving towards the  $H_2$  and  $O_2$  sides of the interface, resulting in local stretching of the interface. The corresponding pressure pulse moving towards the fuel pushes the location of  $Z = 0.5$  surface further towards the pure fuel, and shortly thereafter interacts with the incident shock. At  $76 \mu s$ , the incident shock has moved past the combustion zone (located at  $x \sim 0.09$  m), inferred from the maximum temperature location on the scaled temperature plot (figure 6.5 (c)). Finally, by 0.30 ms, the incident shock has overtaken the rightward combustion wave, while the maximum temperature across the interface is  $\approx 3140$  K in agreement with the predicted adiabatic flame temperature [93].

### 6.3 Non-Reacting RM (CASES 36-41)

To establish a baseline for comparison, we performed simulations of an inert, perturbed front accelerated by a shock, resulting in the classical Richtmyer-Meshkov instability. The simulations were performed with varying values of the interface thickness ( $\Delta$ ), and thus bear relevance to the diffusion flame studies presented in sections 6.4-6.5. The non-reacting, single-mode RMI with a sharp interface has been studied extensively [9,35,36], and the growth rates for such interfaces are well predicted by the so-called impulsive model. For a diffuse interface, Brouillette and Sturtevant [43] extended the model of Duff et al. [87], to include impulsive accelerations, and obtained an eigenvalue solution for the linear growth rate that is a function of the initial interface thicknesses  $\delta$ .

Furthermore, the coefficient  $C$  contained in the growth rate reduction factor  $\psi$  in Eq. 1.5(b) can depend on Atwood number [43].

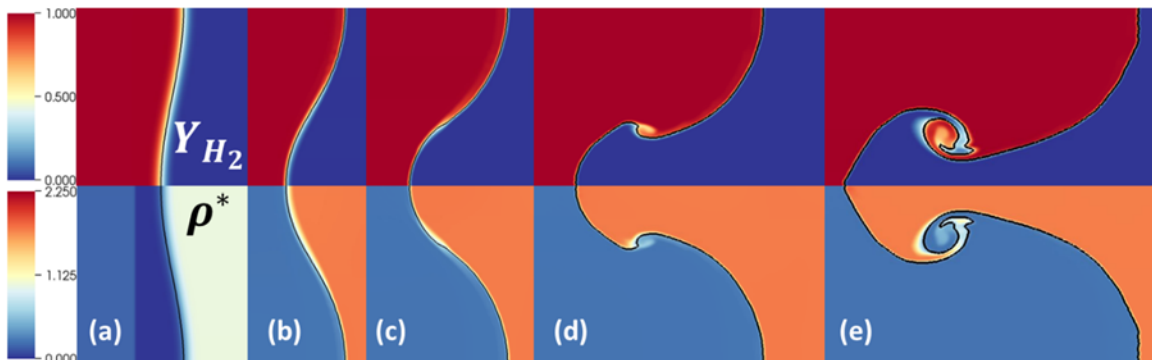


FIGURE 6.6: Contours of  $H_2$  mass fraction (top) and scaled density  $\rho^*$  (bottom) from 2D simulations of a perturbed, non-reacting interface with  $\Delta/h_0 = 4$ , and driven by a Mach 1.2 incident shock. The images are shown at  $kV_0^+(t-t_0) =$  (a)  $-1.4 \times 10^{-2}$ , (b) 0.38, (c) 0.77, (d) 1.96, and (e) 3.93.

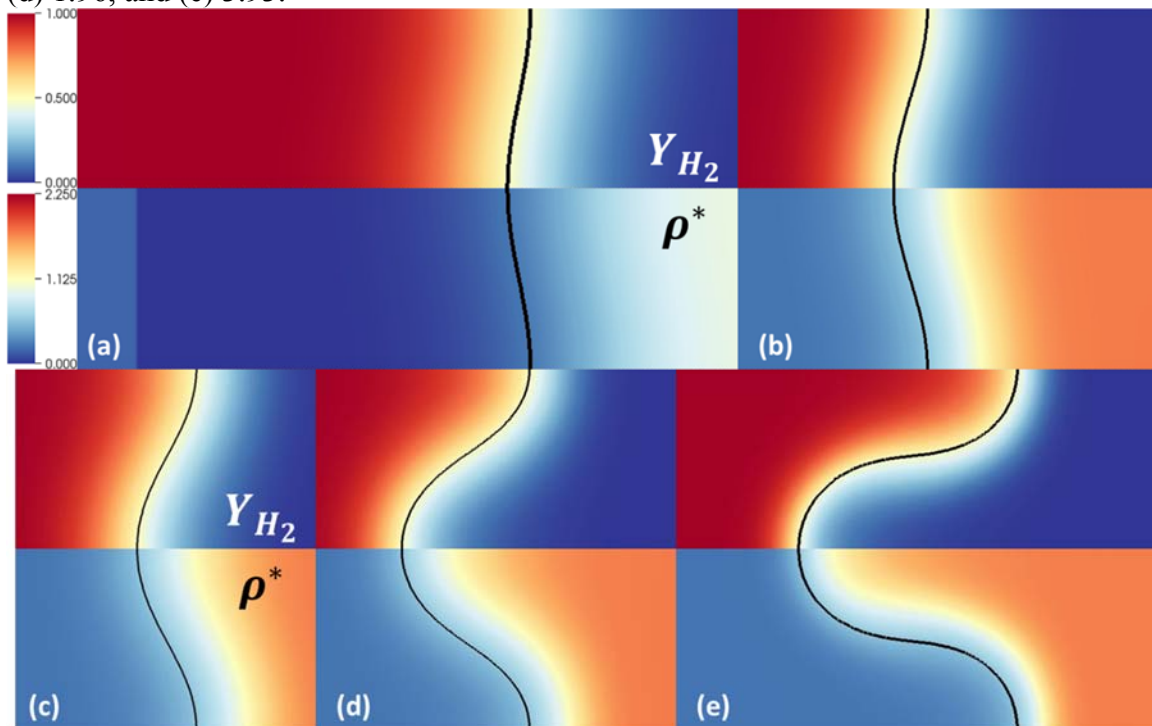


FIGURE 6.7: Contours of  $H_2$  mass fraction (top) and scaled density  $\rho^*$  (bottom) from 2D simulations of a perturbed, non-reacting interface with  $\Delta/h_0 = 64$ , and driven by a Mach 1.2 incident shock. The images are shown at  $kV_0^+(t-t_0) =$  (a) -0.11, (b) 0.27, (c) 0.65, (d) 1.79, and (e) 3.69.

For cases 36-41, the initial interface thickness ( $\Delta$ ) was progressively varied with  $\Delta/h_0 = 2, 4, 8, 16, 32$  and  $64$ , where  $h_0$  was chosen so that  $kh_0 = 0.2$ , as described in section 6.1. Figure 6.6 is a plot of contours of the mass fraction of  $H_2$  (top row), and the scaled density  $\rho^*$  (bottom row) from the simulation with  $\Delta/h_0 = 4$ , with the location of 50% mixture fraction indicated by the solid line. The images are shown at scaled times  $kV_0^+(t-t_0)$  of (a)  $-1.4 \times 10^{-2}$ , (b) 0.38, (c) 0.77, (d) 1.96, and (e) 3.93, where  $V_0^+$  is obtained from Eq. 1.4(post-shock values). Note that  $t_0$  corresponds to the time at which the interface is compressed to its post-shock amplitude  $h_0^+$ . Figure 6.7 shows the corresponding contours from the simulation with  $\Delta/h_0 = 64$ , presented at  $kV_0^+(t-t_0) =$  (a) -0.11, (b) 0.27, (c) 0.65, (d) 1.79, and (e) 3.69. For the sharp interface, by  $kV_0^+(t-t_0) = 0.77$  (figure 6.6 (c)), the fundamental mode has saturated, as higher harmonics now play a pronounced role in the non-linear evolution of the interface. This is followed by the growth and saturation of secondary features, particularly due to the Kelvin-Helmholtz instability leading to the appearance of the classical ‘mushroom’ shapes at  $kV_0^+(t-t_0) = 1.96$  in figure 6.6 (d). The nonlinear stage is also marked by asymmetry between bubbles and spikes at these moderate Atwood numbers. In contrast, for the diffuse interface, the instability growth appears muted consistent with Eq.1.5, as the flow approaches nonlinear saturation only by  $kV_0^+(t-t_0) = 1.79$ . The finite thickness of the interface also mitigates Kelvin-Helmholtz instability growth, and as a result the interface shapes in figure 6.7 remain smooth even at late times without the appearance of secondary features.

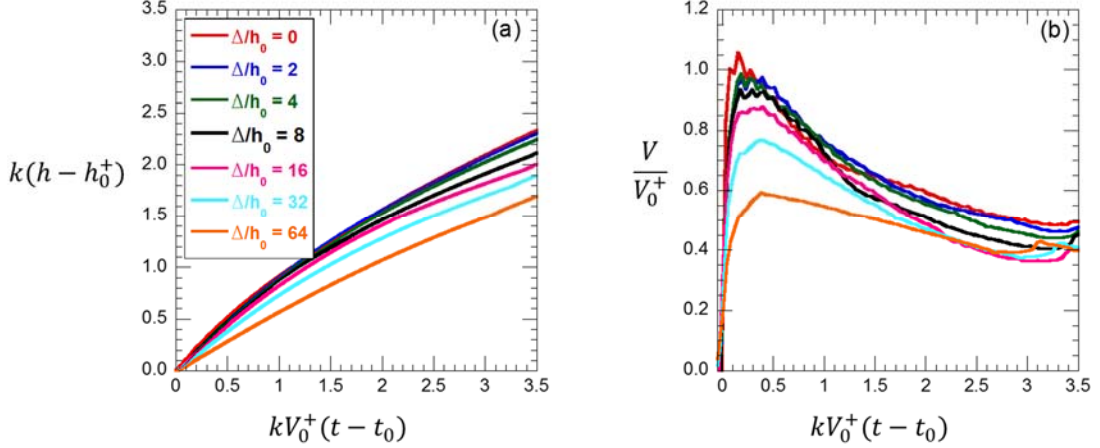


FIGURE 6.8: Evolution of (a) scaled perturbation amplitudes based on distance from peak-to-peak of  $Z_{50}$  and (b) the corresponding growth rates as a function of scaled time from 2D simulations of a non-reacting front with a Mach 1.2 incident shock. Results shown are from simulations with varying  $\Delta/h_0$ .

In figure 6.8 (a), we plot the scaled amplitude  $k(h - h_0^+)$  against the scaled time  $kV_0^+(t - t_0)$  from our RM simulations with varying interface thicknesses ( $\Delta/h_0 = 0 - 64$ ). The corresponding growth rates are shown in figure 6.8 (b), and are scaled by the classical RM growth rate for a sharp discontinuity from Eq. 1.4 assuming post-shock values. The amplitudes in figure 6.8 are inferred from the separation between the peak and the trough of the  $Z_{50}$  interface. From figures 6.8 (a) - (b), it is clear that there is a reduction in the linear (peak) growth rate as the interface thickness is increased, consistent with the model of [43], with the most diffuse interface achieving only 60% of the classical RM growth rate. At late times, with decreasing  $\Delta/h(t)$ , the nonlinear growth rates all collapse indicating the absence of secondary instabilities in the diffuse simulations does not significantly modify the growth of the fundamental RM mode.

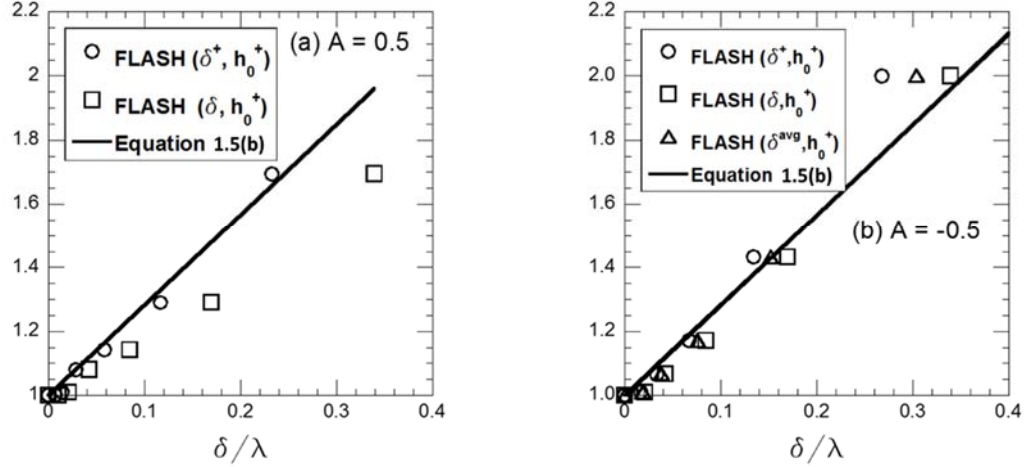


FIGURE 6.9: Growth rate reduction factor ( $\psi = V_0^+ / V$ ) from the 2D non-reacting, RM simulations with (a)  $A = 0.5$  and (b)  $A = -0.5$ , plotted against scaled thickness ( $\delta / \lambda$ ). The squares indicate  $\psi$  calculated from pre-shock quantities, while circles indicate the use of post-shock quantities. The prediction of Eq. 1.5(b) with  $C = 2.83$  is shown as the solid line.

In figure 6.9 (a), we plot the reduction factor ( $\psi$ ) (deduced from the peak growth rates in figure 6.8 (b) as a function of the scaled thickness ( $\delta / \lambda$ ). Eq. 1.5(b) is shown in figure 6.9 as the solid line, and corresponds to a value of  $C = 2.83$  for an Atwood number of 0.5 as suggested by [43] from their experimental verification of Eq. (1.5). The calculations of the reduction factors for our simulations were performed using the pre-(squares) and post-shock (circles) interface thicknesses and post-shock perturbation amplitudes in Eq. (1.5). The post-shock density profile from the numerical simulations were compared to the initial profile used by [43], and reveal a compression to 68.5% of the initial interface thickness ( $\delta^+ \approx 0.68\delta$ ) by the shock. For small interface thicknesses ( $\Delta / h_0 \leq 8$  i.e.  $\delta / \lambda \leq 4.24 \times 10^{-2}$ ), the growth rate reduction factor from our simulations is  $\sim 1$ , as the interface growth approximates that of a sharp front. As the thickness is further increased, there is significant growth rate reduction observed in the simulations, and compares well with the model [43], but only when the post-shock quantities ( $h_0^+, \delta^+$ ) are

used in calculating Eq. 1.5(b). The corresponding data for our non-reacting simulations with  $A < 0$  are displayed in figure 6.9 (b). We find that Eq. 1.5 is valid even for negative, Atwood numbers, with  $C = 2.83$ . We use these findings in sections 6.4-6.6 to interpret results from our simulations of reacting RMI at a perturbed surface separating fuel and oxidizer.

#### 6.4 Unshocked Perturbed Flames (CASES 42-48)

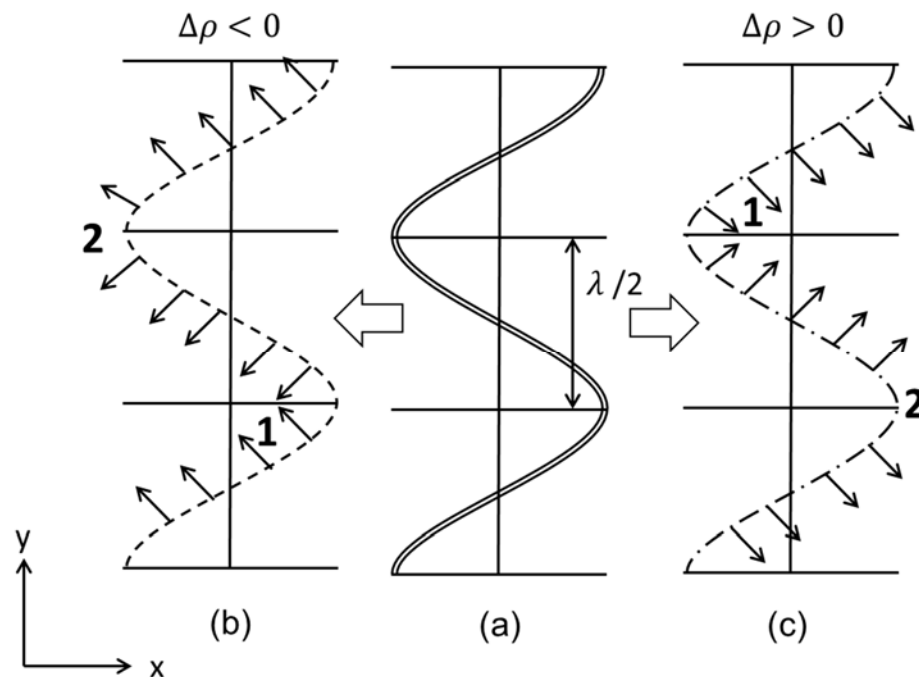


FIGURE 6.10: Schematic of the pressure waves from burning at a 2D front (a) and the resulting combustion waves (b) and (c).

The dynamics of an unshocked, perturbed flame front is important to our understanding of the reacting RMI counterpart, and is explored in detail here. As discussed in section 6.2, combustion of fuel close to the stoichiometric surface will result in a spontaneous pressure rise all along a perturbed interface (figure 6.10 (a)). Subsequently, the pressure pulse splinters into two non-planar combustion waves traveling in opposite directions towards the fuel and oxidizer (figures 6.10 (b) and (c) respectively). Note that

the pure fuel ( $Z = 1$ ) and pure oxidizer ( $Z = 0$ ) isosurfaces experience combustion waves propagating from light-to-heavy and heavy-to-light media respectively. In the latter case, the RM instability of that material line leads to a negative growth rate, including a phase inversion of the initial perturbation. We find the interface acceleration associated with the passage of the combustion wave is given in our simulations by  $g(t) \propto (t/t_0)^a$ , with  $a = -1.8$  reminiscent of a blast wave. In the following, we use the term blast wave to describe the combustion waves observed in our simulations, but caution the reader that the analogy may not be exact. Furthermore, this pressure variation is modulated in the  $y$ -direction by the imposed sinusoidal perturbation resulting in a distinct non-planarity of the pressure waves. The non-planarity (in  $y$ ) of the waves stems from the corresponding distortion of the burning surface, and plays an important role in their propagation through the fuel/ $O_2$  media and the interaction with material interfaces.

In figure 6.10 (b), the single arrows represent the surface normal to each wave in the direction of its propagation. Region 1 (2) indicates the converging (diverging) portions of the non-planar waves (figures 6.10 (b) and (c)), where the local pressure is higher (lower). The increased pressure in region 1 of each wave imparts to that segment a greater velocity than region 2 where the pressure is lower, resulting in localized stretching (compression) of the waves. By this mechanism, the waves lose their curvature over time (i.e. distance traveled) and are eventually rendered planar. The deviation from planarity of the pressure wave at the instant of interaction with the material surface depends in turn on the thickness of the interface: For large  $\Delta/h_0$ , since the pressure front travels a greater distance before impinging on the interface, any imposed perturbations are flattened through the process depicted in figure 6.10. Conversely, for modest values of  $\Delta/h_0$ , the  $Z_{50}$  surface

is located in close proximity to  $Z_{st}$  where the pressure front originates, so that non-planar distortions on the pressure front have not been allowed sufficient time to even out, before interacting with the interface.

In the following, we describe the complex evolution of a material interface when it is impacted by a non-planar (perturbed) blast wave type profile, and draw distinctions from the corresponding planar interaction. For instance, the interface corresponding to  $Z_{50}$  is accelerated by a time-dependent acceleration similar to a blast wave in a heavy  $\rightarrow$  light interaction, but the subsequent development is dictated by the strength of the pressure pulse ( $p_s / p_0$  in figure 6.11) and the extent of its non-planarity.

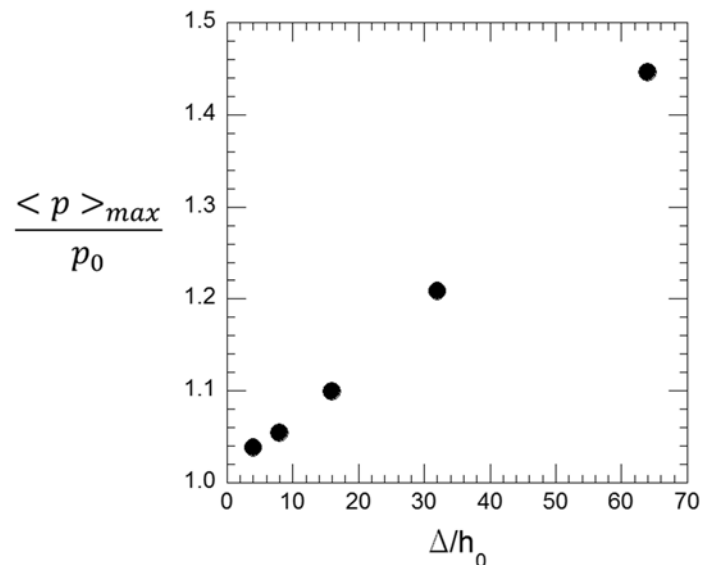


FIGURE 6.11: Scaled peak pressure ( $\langle p \rangle_{max} / p_0$ ) associated with the combustion waves plotted against the scaled interface thickness ( $\Delta / h_0$ ) for the simulations described in section 6.4.

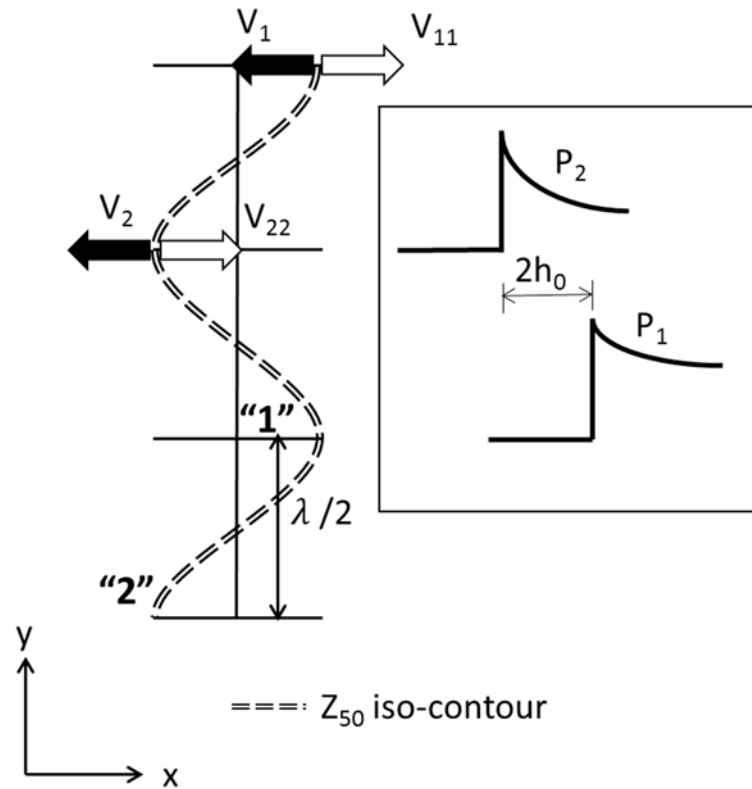


FIGURE 6.12: A schematic of the interaction of a combustion wave (figure 6.10 (b)) with the interface ( $Z_{50}$ ). Inset shows incident pressure pulses with a separation distance of  $2h_0$ . Such a modulated combustion wave can lead to decompression-driven growth of the interface.

The thickness of the interface influences the strength of the combustion wave, since the mass of fuel available for burning scales with  $\Delta / h_0$ . Figure 6.11 shows the variation of the peak planar-averaged (indicated by the operator  $\langle \bullet \rangle$ ) pressure associated with the combustion-driven blast wave, and scaled by the initial pressure ( $p_0$ ) plotted against the scaled initial thicknesses ( $\Delta / h_0$ ). The peak values in pressure were obtained in each case at the end of the spontaneous ignition phase of combustion (and prior to the splintering of the combustion wave). Perhaps unsurprisingly, the peak pressure (and the Mach number of the combustion wave) is linearly dependent on the interface thickness, and hence on the mass of fuel available for burning.

When such a complex combustion wave crosses the interface ( $Z = 50\%$ ), the growth of the interface is highly transient featuring multiple stages of positive and negative growth. For instance, the passage of the initial shock front (figure 6.12) across a heavy  $\rightarrow$  light interface ( $Z_{50}$ ), renders the interface unstable to RMI. This is due to the deposition of baroclinic vorticity at the interface ( $\nabla p \otimes \nabla \rho$ ), while the fast  $\rightarrow$  slow interaction ensures a negative growth rate with a phase reversal. However, the time-dependent pressure variation behind the shock front drives a (variable  $g$ ) Rayleigh-Taylor (RT) instability, since at the interface  $\nabla p \cdot \nabla \rho < 0$ . Thus, during the expansion phase, the RT growth is seeded by the perturbation amplitude at the end of the RM growth phase. Note that during this late stage, the interface grows due to the variable-drive RT and the RMI (since the interface retains the baroclinic vorticity and continues to grow from the velocity induced from it), although the growth rates do not reinforce linearly as pointed out by [123]. Thus, the nonlinear decay of the RMI (commonly observed for  $kh(t) > 1$ ) is moderated by growth due to RT instability during this stage.

The expansion phase of interfacial evolution could also be complicated by multiple decompression-driven instabilities described here. For example at any instant, points corresponding to the crest and the trough of the interface (points '1' and '2' in figure 6.12) are driven by portions of the blast wave that correspond to different values of pressure gradients. Similarly, the non-planarity of the pressure wave results in pressure variation across  $y$ -direction and hence a variation in the corresponding interface velocities imparted to points '1' and '2'. These effects combine to produce a net decompression-driven growth of the interface that is positive (figure 6.15), thereby opposing the negative growth due to the combined RT/RM instabilities. Thus, the late-time evolution of the interface is

complicated involving growth due to multiple hydrodynamic instabilities (RT/RM) as well as instabilities due to decompression effects. Miles et al [124] observe similar phenomena in their experimental/numerical study of laser-energized targets on the OMEGA laser facility. The blast waves generated from strong laser pulses trigger an initial RM phase immediately followed by a variable acceleration RT phase. However, the nonlinear evolution of perturbations at the interface of a two-layer target in their study is affected by growth due to decompression according to the mechanism described above. Accordingly, [124,125] suggest a correction to the growth of the interface due to decompression to isolate the growth due to the hydrodynamic instabilities. We have evaluated this correction for the blast wave-type combustion wave profiles generated in our simulations and find that the contribution due to expansion is less than 5% of  $V_0$ , where  $V_0$  is the RM growth rate from the passage of the shock front. In contrast we expect the contribution due to non-planarity to be more significant, while also noting that obtaining an estimate of such effect is non-trivial.

To describe this transient and complex behavior, we first delineate the velocities associated with the interface corresponding to different stages of shock/expansion wave passage. In the schematic represented in figure 6.12,  $V_1(V_2)$  is the constant jump velocity associated with the planar shock interaction with region 1 (2), while  $V_{11}(V_{22})$  represents the time-dependent interface velocity resulting from the passage of the expansion region behind the shock front. For classical RM,  $V_{11} = V_{22} = 0$  so that the interface growth may be represented according to,

$$\frac{dh}{dt} = \frac{V_2 - V_1}{2}. \quad (6.6)$$

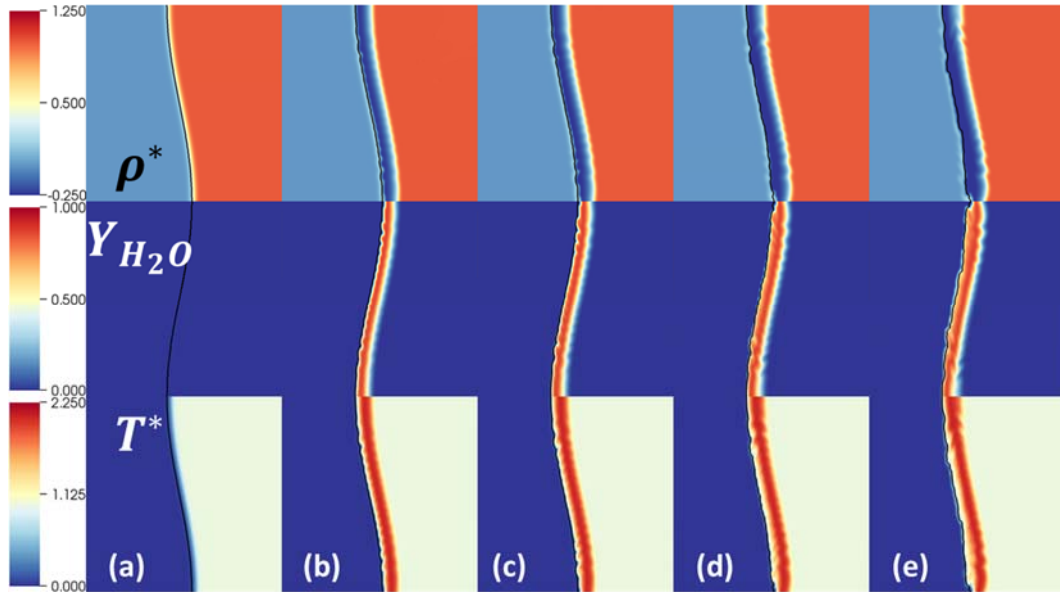


FIGURE 6.13: Contours of (top to bottom) the scaled density  $\rho^*$ ,  $H_2O$  mass fraction and the scaled temperature  $T^*$  from 2D simulations of a perturbed, reacting interface with  $\Delta / h_0 = 2$ , with no incident shock. The images are shown at  $kV_0^+(t - t_0) =$  (a)  $-1.6 \times 10^{-4}$ , (b)  $3.4 \times 10^{-2}$ , (c)  $6.8 \times 10^{-2}$ , (d) 0.17, and (e) 0.34.

When accelerated by a (non-planar) combustion wave, the interface initially attains the velocities  $V_1$  and  $V_2$ , but the subsequent development is governed by time-dependent velocities  $V_{11}(t)$  and  $V_{22}(t)$ . Note that when the blast wave suffers from significant non-planarity,  $V_{11}(t) \neq V_{22}(t)$ , and will result in a net (positive in this case) growth rate of the interface. Under such circumstances, the interface will grow according to,

$$\frac{dh}{dt} = \frac{(V_2 - V_{22}(t)) - (V_1 - V_{11}(t))}{2}. \quad (6.7)$$

For large thicknesses, there exists a significant interval of time between the generation of the combustion wave and its interaction with the interface that the pressure wave will flatten (along  $y$ ) before crossing the  $Z_{50}$  surface. The pressure profile behind the wave has relaxed sufficiently ( $V_{11} \sim V_{22} \ll V_1$  or  $V_2$ ), and such an interaction would be more RM-like.

Figure 6.13 shows contours of the scaled density  $\rho^*$ , temperature  $T^*$  and the mass fraction of  $H_2O$  for a sharp interface ( $\Delta / h_0 = 2$ ) at scaled times ( $kV_0^+(t - t_0)$ ) (a)  $-1.6 \times 10^{-4}$  (b)  $3.4 \times 10^{-2}$  (c)  $6.8 \times 10^{-2}$  (d) 0.17 and (e) 0.34 respectively. Note that the solid line in figure 6.13 represents  $Z_{50}$ , the 50% mixture fraction level. To enable direct comparison with the reacting RMI, we scale pressure with  $p_s \approx 0.15$  MPa, the pressure behind the combustion wave bound for the fuel stream. For the unshocked front shown in figure 6.13, the pressure across the interface rises to  $\sim 0.11$  MPa ( $p^* = 0.08$ ) at early times, which is not sufficient to significantly distort the interface. By  $kV_0^+(t - t_0) = 3.4 \times 10^{-2}$ , the pressure across the interface has returned to atmospheric and remains so through the end of the simulation. As the interface burns, and products of combustion are added, the associated temperature increase causes the density across the interface to drop to  $\sim 4.11 \times 10^{-2} \text{ kg/m}^3$  ( $\rho^* = -0.24$ ) at  $kV_0^+(t - t_0) = 3.4 \times 10^{-2}$  (figure 6.13 (b)), and eventually reaching an asymptotic value of  $\sim 3.6 \times 10^{-2} \text{ kg/m}^3$  ( $\rho^* = -0.27$ ) at  $kV_0^+(t - t_0) = 0.34$ . Throughout this process, the amplitude of the interface does not vary significantly, while the maximum product mass fraction ( $Y_{H_2O}$ ) approaches  $\sim 0.87$  close to the value obtained for the unperturbed flame. Finally, the flame achieves a maximum temperature of  $T = 3050$  ( $T^* \sim 2.08$ ) at  $kV_0^+(t - t_0) = 0.34$  (similar to the unperturbed case), consistent with the stoichiometric adiabatic flame temperature ( $\sim 3130$  K) prediction from [93]. Even at late times ( $kV_0^+(t - t_0) = 0.34$ ), flame corrugation and curvature effects are minimal (figure 6.13 (e)) when the initial interface is sharp.

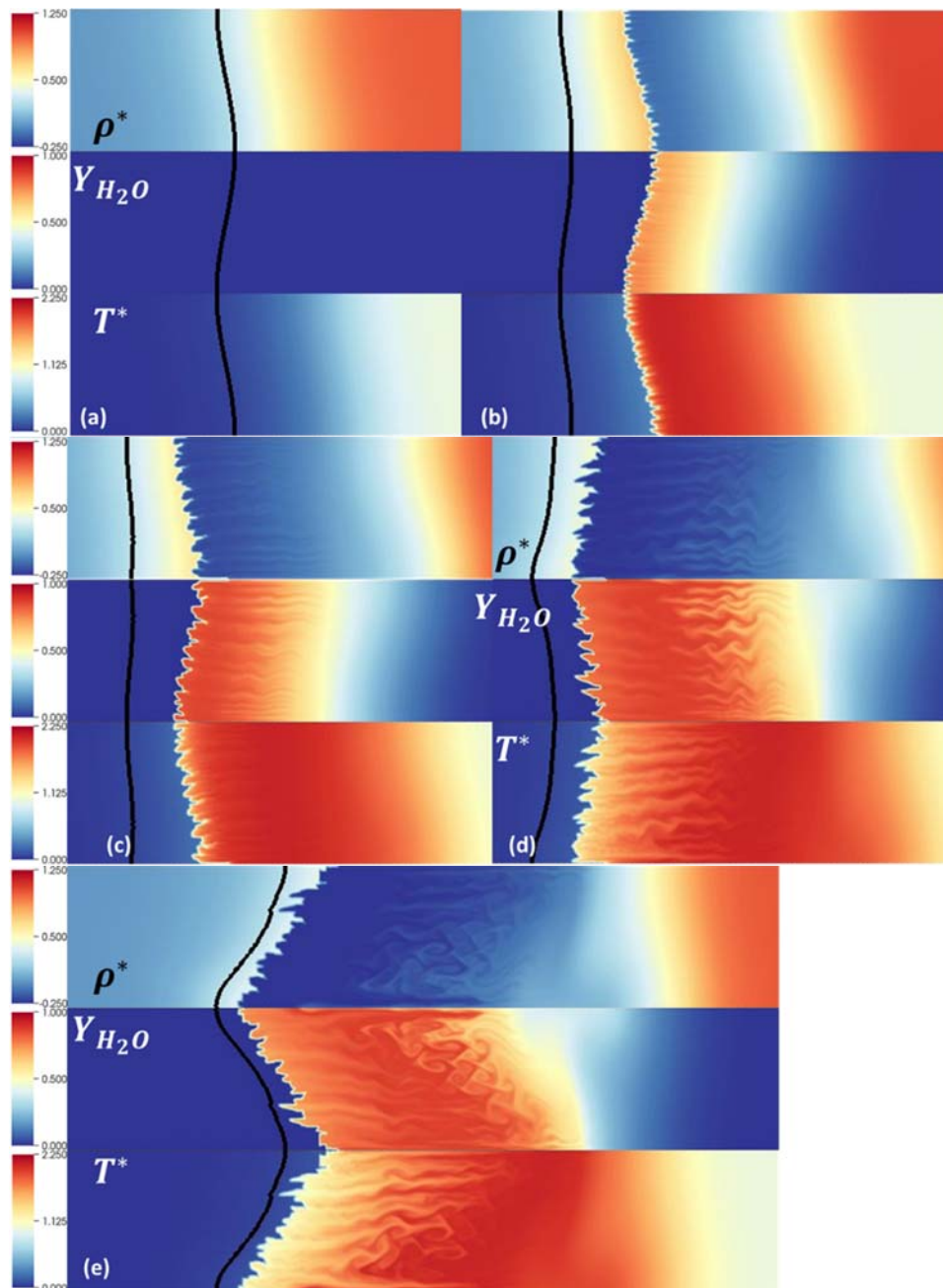


FIGURE 6.14: Contours of (top to bottom) the scaled density  $\rho^*$ ,  $H_2O$  mass fraction and the scaled temperature  $T^*$  from 2D simulations of a perturbed, reacting interface with  $\Delta/h_0 = 64$ , with no incident shock. The images are shown at  $kV_0^+(t-t_0) =$  (a)  $-9.6 \times 10^{-2}$ , (b) 0.19, (c) 0.48, (d) 1.34, and (e) 2.77.

The flow and flame features described above are modified profoundly when burning occurs at a diffuse interface. Figure 6.14 is a plot of contours of the scaled density

$\rho^*$ , temperature  $T^*$  and the mass fraction of  $H_2O$  from our simulation with  $\Delta / h_0 = 64$ , presented at scaled times ( $kV_0^+(t - t_0)$ ) (a)  $-9.6 \times 10^{-2}$ , (b) 0.19, (c) 0.48, (d) 1.34, and (e) 2.77 respectively. The pressure across the interface rises to 0.16 MPa ( $p^* = 1.22$ ) at time  $kV_0^+(t - t_0) = -7.7 \times 10^{-2}$ , corresponding to a Mach number of 1.24 according to equation (6.5). Note that we independently computed the wave speed associated with the combustion wave directly from our simulations (by tracking the location of the peak planar-averaged pressure gradient), and found this to be within 20% of the prediction of Eq. (6.5). Subsequently, the pressure pulse splinters into two combustion waves travelling in opposite directions as described earlier, with the dominant wave ( $Ma \approx 1.18$ ) moving towards  $H_2$ , and imparting a net negative velocity to the interface. Since the combustion wave has a finite curvature described above, the acceleration imparted to the interface is not uniform along y-direction leading to further distortion of the interface. By  $kV_0^+(t - t_0) = 0.19$ , the combustion waves have receded from the interface, leaving in their wake complex, localized pressure gradients in the vicinity of the interface. Thus, the interface ( $Z = 0.5$ ) is accelerated by the pressure waves which originate at  $Z \sim 1.45 \times 10^{-2}$  (lean  $Z$ ), and appears to grow through the complex sequence of instabilities in figures 6.14 (c) - (e). For the  $Z = 0.5$  material line (which we track in our perturbation amplitude calculation), the 'shock' travels from the heavy to light gas (with  $A = -0.5$ ), and thus initiates a complete phase reversal by figure 6.14 (d) ( $kV_0^+(t - t_0) = 1.34$ ). In contrast, a material line within the pure  $O_2$  stream would experience a 'shock' traveling from the light to heavy gases, and thus would experience no phase reversal. Thus, strong burning at a diffuse interface appears to initiate interface distortion through RMI growth, due to the spontaneous generation of

strong combustion waves. This is of course complicated by many factors including secondary instabilities (figures 6.14 (c) - (e)), and variations in fluid properties such as the adiabatic index, density and temperature across the interface. Note that the flame strands observed in figure 6.14 are likely seeded by the grid, and are observed to appear at a finer scale when the calculation is repeated at twice the resolution ( $512/\lambda$ ).

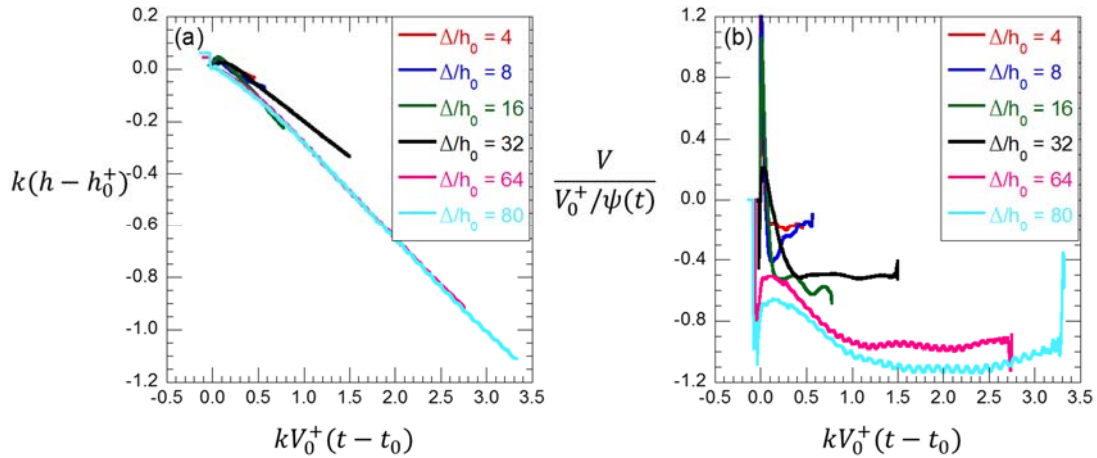


FIGURE 6.15: Evolution of (a) scaled perturbation amplitudes based on distance from peak-to-peak of  $Z_{50}$  and (b) the corresponding growth rates as a function of scaled time from 2D simulations of a reacting front with no incident shock. Results are shown from simulations with varying  $\Delta/h_0$ .

Figure 6.15 is a plot of (a) the scaled amplitude based on  $Z_{50}$  and the corresponding (b) growth rates against scaled time ( $kV_0^+(t - t_0)$ ) from our simulations with  $\Delta/h_0 = 4 - 80$ . Note that the thickness of the interface  $\Delta$  increases significantly for these cases due to burning and subsequent expansion by the blast wave. Thus, the growth rate reduction factor  $\psi$  defined by Eq. 1.5 will itself be time-dependent, as evident in (figure 6.16). The initial reduction in the interface amplitude observed in figure 6.15 (a) for all cases can be attributed to the compression of the interface by the shock front. For all the simulations with moderate values of interface thicknesses ( $\Delta/h_0 = 4 - 32$ ), following shock

compression, the  $Z_{50}$  surface undergoes a net initial positive growth phase. The combustion waves for these cases have not flattened out ( $V_1 \sim V_2$ ), while the pressure gradient behind the wave, as experienced by the interface in region 1 and 2 (figure 6.12) varies so that ( $V_{11} > V_{22}$ ). Thus, even though a net negative velocity is imparted by the shock wave ( $V_1 \sim V_2 < 0$ ) to the interface, the y-variation of the pressure gradient in the expansion region of the wave results in a counterintuitive, net positive growth for these heavy-to-light cases. The interface then continues to grow according to this time-varying pressure gradient. Following these initial transients, the pressure gradient across the interface becomes negligible (as the blast wave leaves the  $Z_{50}$  line). Accordingly, the interface now resumes its negative RM growth under the influence of the baroclinic vorticity deposited initially by the leading shock front. The interface continues to grow with this net negative velocity until late times (eventually undergoing phase inversion).

In contrast, for large thicknesses, the  $Z_{50}$  iso-contour is sufficiently removed from the initial pressure rise, that the combustion wave has flattened (thus,  $V_1 > V_2$ ) before reaching the interface ( $Z_{50}$ ). Furthermore, the pressure profile behind the blast wave has relaxed, leading to lower gradients across the interface ( $V_{11} \sim V_{22}, V_1 \gg V_{11}$  and  $V_2 \gg V_{22}$ ). Thus, for our simulations with large thicknesses ( $\Delta / h_0 = 64, 80$ ), the perturbation growth is largely reminiscent of RM with no positive growth observed in figure 6.15. The evolution of perturbation growth rates scaled by  $V_0^+ / \psi(t)$  is shown in figure 6.15 (b) as a function of the scaled time  $kV_0^+(t - t_0)$ . Again, the differences between the growth of narrow ( $\Delta / h_0 \leq 32$ ) and wide ( $\Delta / h_0 > 32$ ) interfaces is evident. In the former case, the RM growth appears to be significantly modified by non-planar effects, leading to an initial

stage of positive growth rate, followed by a late-time evolution during which the RM growth rate continues to be modified by the decompression effects detailed earlier (the peak growth rates for these cases are lower than the theoretical values expected for RM growth). For large interface thickness values in the absence of non-planar effects, the growth rate hews closely to RM instability growth expected for  $A < 0$ , leading to negative growth rates in good agreement with Eq. 1.5.

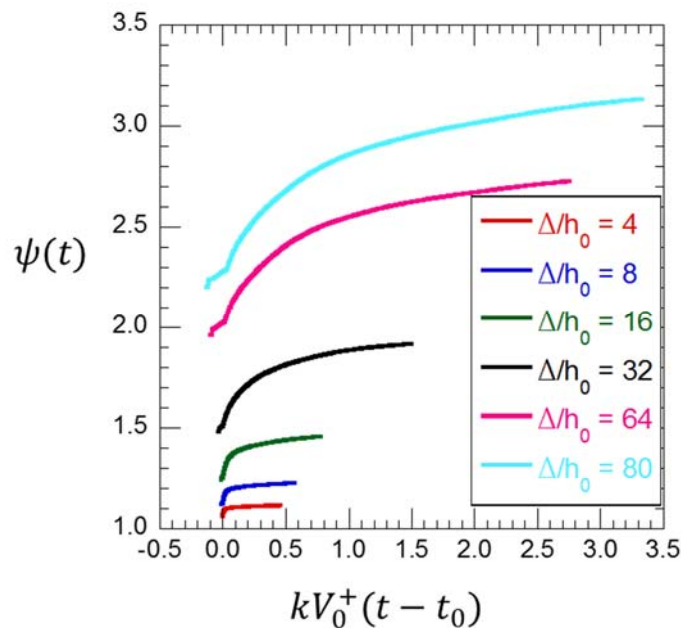


FIGURE 6.16: Time varying reduction factor  $\psi(t)$  from simulations of an unshocked, reacting flame with different initial values of  $\Delta/h_0$ .

### 6.5 A Perturbed Flame Accelerated by an Incident Shock (CASES 49-54)

We now describe the evolution of the interfaces and the flame, when accelerated by an incident shock of Mach 1.2 specified at  $x_s = 0.01$  m and traveling from the light to heavy gases. The passage of the incident shock initiates RMI at the material interfaces, but this is complicated by the combustion waves originating at the flame front, which interact both with the interface and the incident shock. Thus, any of the interfaces described in sections 6.3 – 6.4 now evolve under the influence of multiple shocks, with overlapping regions of transient growth. As in section 6.4, our study included 2D simulations with

thickness to amplitude ratios of  $\Delta/h_0 = 2 - 64$ . We first describe the detailed phenomenology before discussing growth rates from the flames.

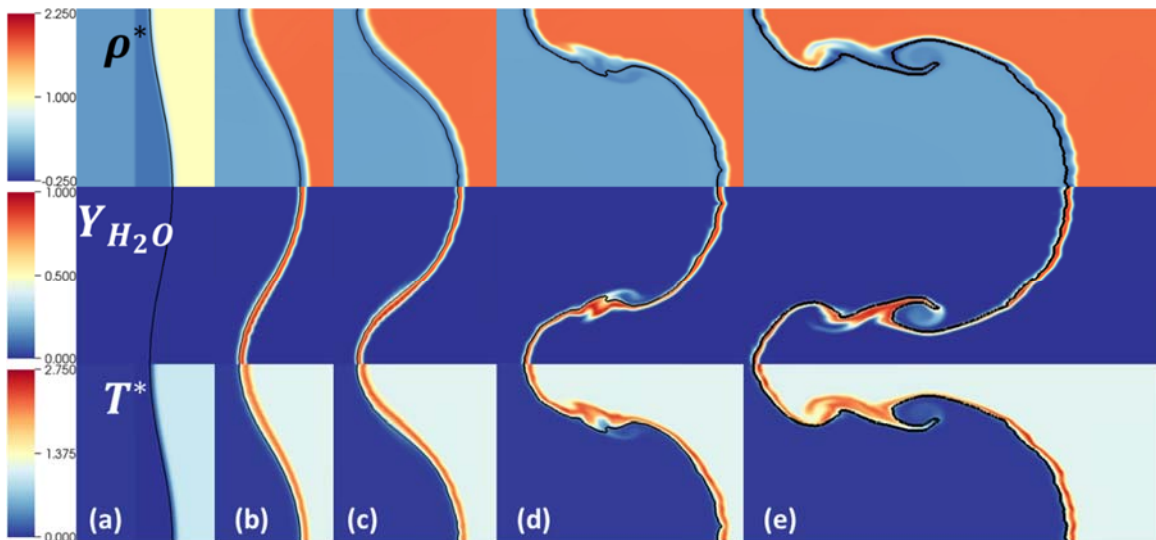


FIGURE 6.17: Contours of (top to bottom) the scaled density  $\rho^*$ ,  $H_2O$  mass fraction and the scaled temperature  $T^*$  from 2D simulations of a perturbed, reacting interface with  $\Delta/h_0 = 2$ , and driven by a Mach 1.2 incident shock. The images are shown at  $kV_0^+(t-t_0) =$  (a)  $-1.2 \times 10^{-2}$ , (b) 0.39, (c) 0.79, (d) 1.99, and (e) 3.99.

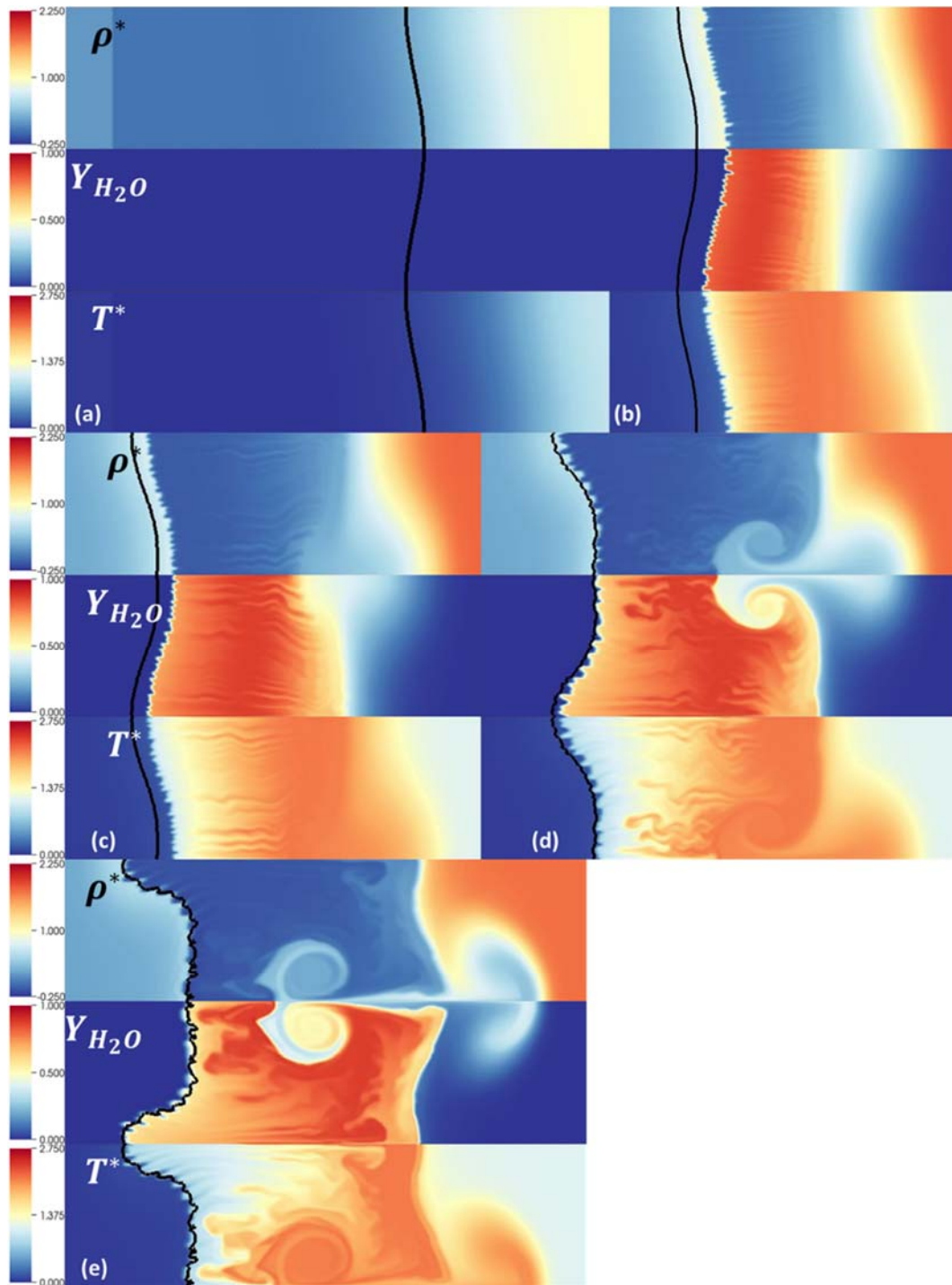


FIGURE 6.18: Contours of (top to bottom) the scaled density  $\rho^*$ ,  $H_2O$  mass fraction and the scaled temperature  $T^*$  from 2D simulations of a perturbed, reacting interface with  $\Delta/h_0 = 64$ , and driven by a Mach 1.2 incident shock. The images are shown at  $kV_0^+(t-t_0) =$  (a)  $-9.5 \times 10^{-2}$ , (b) 0.21, (c) 0.51, (d) 1.41, and (e) 2.92.

Figure 6.17 is a plot of mass fraction contours of  $H_2O$ , scaled density  $\rho^*$  and temperature  $T^*$  from our simulation with  $\Delta/h_0 = 2$ , and shown at scaled times ( $kV_0^+(t-t_0)$ ) of (a)  $-1.2 \times 10^{-2}$ , (b) 0.39, (c) 0.79, (d) 1.99, and (e) 3.99. Once again, the solid line in the figure represents the iso-contour of 50% of the mixture fraction ( $Z_{50}$ ). Figure 6.18 shows these scaled quantities for the corresponding diffuse ( $\Delta/h_0 = 64$ ) interface. The incident shock compresses the sharp and diffuse interfaces to post-shock amplitudes (based on  $Z_{50}$ )  $\sim 0.80 h_0$  and  $\sim 0.60 h_0$  respectively. The maximum temperature across the interface is  $\sim 3250$  K ( $T^* \sim 2.23$ ) and  $3167$  K ( $T^* \sim 2.17$ ) for the sharp and diffuse interfaces at scaled times  $kV_0^+(t-t_0) \approx 3.99$  and  $\approx 2.92$  respectively, compared to the stoichiometric adiabatic flame temperature of  $\sim 3200$  K ( $T^* \sim 2.19$ ). The compression of the interface due to the incident shock reduces the flame thickness, but appears to increase the mass flow rate of fuel into the flame resulting in greater heat addition. We believe this explains the higher flame temperatures observed for the sharp interface compared to the diffuse counterpart. Within the diffuse interface, secondary instabilities form flame strands seen in figures 6.18 (b) - (c). Note that these instabilities were also observed for the corresponding unshocked cases, where pronounced flame strands were observed at late times (for instance, figure 6.14 (c)). At  $kV_0^+(t-t_0) = 0.79$  (figure 6.17 (c)), the bubble and spike fronts appear to be asymmetric, with the bubbles forming a flat surface, while spikes are long and pointed. For the diffuse front (figure 6.18 (c)), the flame strands continue to grow within the interface, while secondary modes develop towards the oxygen side of the interface (near the bubble). Subsequently, the diffuse interface exhibits a broadening of the already flat bubble surface (due to the saturation of higher harmonics in the flow), causing the interface

shape to deviate from the initial sinusoidal form. Furthermore, by  $kV_0^+(t-t_0) = 1.41$ , the appearance of secondary modes in the form of mushroom-shaped rollups is evident within the oxidizer. Finally, at late times ( $kV_0^+(t-t_0) = 3.99$ ), for a sharp interface, the interface burning appears to elongate the mushroom shaped structures, not seen in the non-reacting counterpart.

As described in section 6.4, burning of fuel near the stoichiometric surface generates blast waves that interact with the  $Z_{50}$  surface, but in the direction of heavy  $\rightarrow$  light fluids. When an incident shock is also present, the combustion waves pass through the incident shock, thus temporarily modifying its structure (figure 6.5). In contrast to the simulations described in section 6.4, the subsequent interfacial dynamics is predominantly governed by the incident shock which rapidly recovers from its interaction with the combustion wave and returns to its initial configuration. However, the combustion process affects the RM growth rate indirectly through the decompression-driven broadening of the interface thickness observed for large values of  $\Delta/h_0$ . This trend is evident in figure 6.19, where we have plotted the reduction factor  $\psi$  used in Eq. 1.5(b) against the scaled time  $kV_0^+(t-t_0)$ . At moderate values of  $\Delta/h_0$  ( $\leq 16$ ), following an initial decrease due to shock compression, the factor  $\psi$  is nearly constant and in good agreement with the theoretical values predicted by Eq.(1.5). For these cases, the combustion wave crosses the interface first, followed by shock passage. However, for  $\Delta/h_0 > 16$  the burning occurs at a site far removed from the  $Z_{50}$  surface. This causes the shock to cross the interface first, followed by a gradual expansion due to passage of the blast wave. As a result, we observe in figure

6.19, the reduction factor  $\psi$  for the diffuse cases increases gradually in response to decompression due to the slowly moving blast wave.

Figure 6.20 is a plot of (a) the perturbation amplitude (based on extrema of the  $Z_{50}$  line) and (b) the corresponding growth rates against scaled time ( $kV_0^+(t - t_0)$ ) for interfaces with varying  $\Delta/h_0$ . Note that  $V_0^+$  is the growth rate corresponding to the post-shock amplitude, while  $t_0$  is the time by which the incident shock compresses the interface to its post-shock amplitude. Consistent with the qualitative description outlined above, the evolution of the perturbation amplitudes and growth rates in figure 6.20 is suggestive of dynamics where the incident shock dominates the blast wave. We expect simulations with large values of  $\Delta/h_0$  to report lower values of the peak perturbation growth rate, and hence have introduced the time-dependent thickness reduction factor  $\psi$  to collapse our data (figure 6.20 (b)). When scaled with  $(V_0^+ / \psi(t))$ , the growth rates from our simulations with  $\Delta/h_0 \leq 32$  display peak values  $\sim 1$ , followed by a nonlinear decay during which the curves collapse. Unfortunately, when  $\Delta/h_0 = 64$  the peak growth rate achieved is only 60% of the prediction from the modified impulsive model Eq.1.5, followed by a weak decay phase.

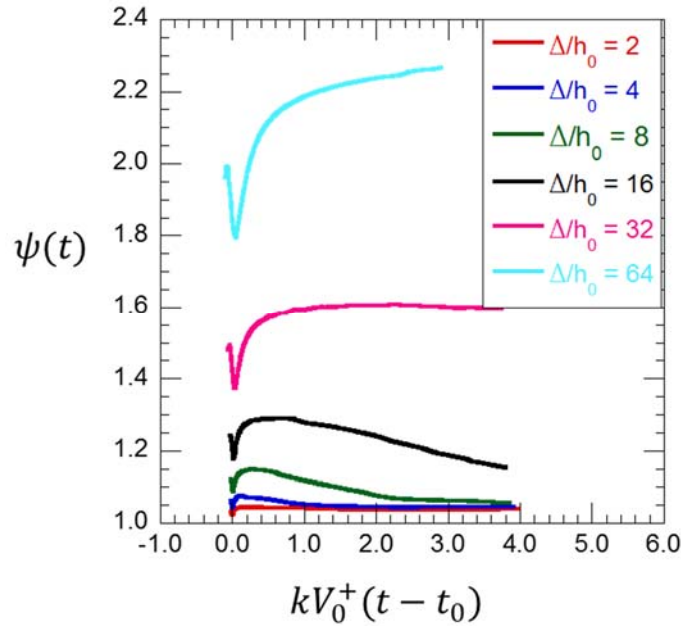


FIGURE 6.19: Time varying reduction factor  $\psi(t)$  from simulations of a shocked, reacting flame with different initial values of  $\Delta/h_0$ .

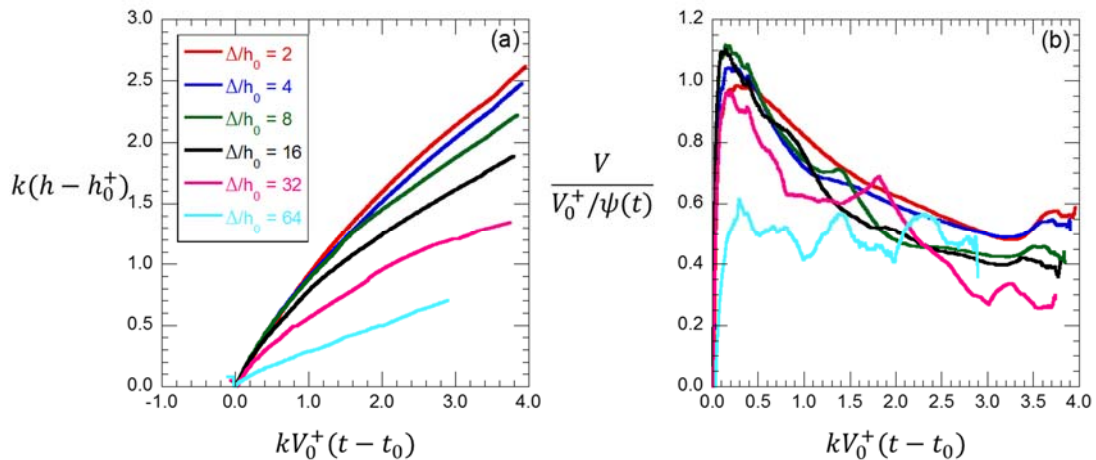


FIGURE 6.20: Evolution of (a) scaled perturbation amplitudes based on distance from peak-to-peak of  $Z_{50}$  (b) and the corresponding growth rates as a function of scaled time from 2D simulations of a reacting front with a Mach 1.2 incident shock. Results shown are from simulations with varying  $\Delta/h_0$ .

### 6.6 Reshocked Flames (CASE 55)

A separate simulation in which the boundary surface at  $x = 6 \lambda$  is treated as a reflecting wall was also performed to study the dynamics of the interface and the flame

surface when subjected to a second compression by the reflected 'reshock' (this allows an investigation of the reacting RM instability in the limit of a finite-amplitude initialization). However, during reshock, the shock passage is from heavy to light media ( $A < 0$ ), while the interface has already reached nonlinearity. Such a situation involving multiple shock-interface interactions is of more than academic interest, and occurs in many applications including scramjets, Inertial Confinement Fusion and supernovae detonations.

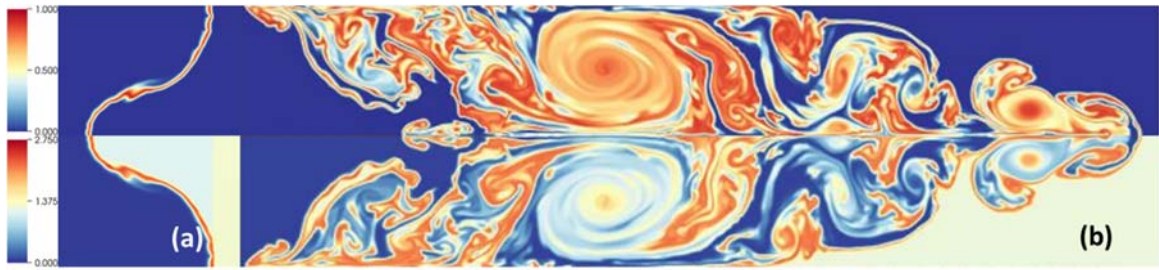


FIGURE 6.21: Contours of  $H_2O$  mass fraction (top) and scaled temperature  $T^*$  (bottom) from 2D simulations of a perturbed, reacting interface with  $\Delta/h_0 = 2.0$ , and driven by a Mach 1.2 incident shock. The images are shown at (a)  $kV_0^+(t-t_0) = 1.59$  just before reshock and (b)  $kV_0^+(t-t_0) = 7.99$  at late time after reshock.

The problem configuration was as described in section 6.1, but with an aspect ratio of 6 and an initial interface with thickness,  $\Delta/h_0 = 2$ . In our simulations, the reshock occurred when the perturbed interface had already matured to nonlinearity, and at a scaled time,  $kV_0^+(t-t_0) = 1.59$ , where  $V_0^+$  is obtained from Eq. 1.4. Following reshock, a complete phase reversal of the original sinusoidal perturbation is observed (figure 6.21), while significant mixing is evident at late times due to the aggressive growth of RMI at an already nonlinear interface. Figure 6.21 is a plot of the scaled temperature  $T^*$  and product mass fraction at scaled non-dimensional times (a)  $kV_0^+(t-t_0) = 1.59$ , just before reshock and (b) at late times  $kV_0^+(t-t_0) = 7.99$ . The reshock event greatly enhances mixing at the

interface due to significant nonlinear growth of already saturated modes, and is followed by a significant increase in the energy release rate.

Following [126], the combustion efficiency may be computed based on the mass fractions of species using:

$$\eta_c = 100 \times x_{H_2O} Y_{H_2O} / (x_{H_2O} Y_{H_2O} + x_{H_2} Y_{H_2} + x_{HO_2} Y_{HO_2} + x_{H_2O_2} Y_{H_2O_2} + x_{OH} Y_{OH} + x_H Y_H) \quad (6.8)$$

where,  $x_i$  is the fractional atomic mass component of hydrogen in species  $i$  and  $Y_i$  is the mass fraction of species  $i$ . The time evolution of such a combustion efficiency integrated across the mixing width,

$$\eta_{int} \equiv \frac{1}{W_{mix}} \int_0^\infty \langle \eta_c \rangle dx, \quad (6.9)$$

is plotted in figure 6.22 and shows marked increases following each shock. Note that within the mixing zone are isolated pockets where  $\eta_c \rightarrow 1$ , co-existing with regions where no reaction has taken place. Thus, an integral along  $x$  reports much lower values seen in figure 6.22. The enhancement in efficiency following reshock is dramatic due to the increased turbulent mixing across the flame surface driven by a re-energized RM instability. The time evolution of the integral mixing width ( $W_{mix}$ ),

$$W_{mix} \equiv \int_0^\infty 4 \langle Z(1-Z) \rangle dx \quad (6.10)$$

is shown alongside the integrated combustion efficiency ( $\eta_{int}$ ) in figure 6.22.

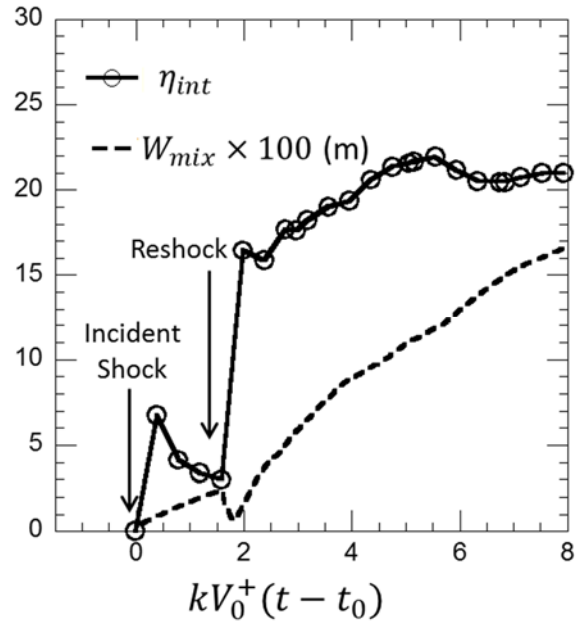


FIGURE 6.22: Growth of the mixing layer width ( $W_{mix}$ ) and the integral planar averaged combustion efficiency ( $\int \langle \eta_c \rangle dx / W_{mix}$ ) plotted against scaled time ( $kV_0^+(t - t_0)$ ), for reacting RM with reshock.

## CHAPTER 7: SUMMARY AND CONCLUSIONS

We have described modifications (chapter 2) to the compressible flow code FLASH that allow for accurate description of chemically reacting flows with heat addition. Our development work includes the addition of a chemistry library with detailed reaction mechanisms to describe  $H_2$ -Air and  $CH_4$ -Air chemistry, extension of the materials database to handle temperature-dependent transport properties, extension of the equation of state module to handle temperature-dependent adiabatic indices of mixtures, extension of the diffusion module to include diffusion of mass and momentum, and modification of existing ODE integrators to solve for Arrhenius reaction rates in a chemical reaction network. The modified FLASH code was used to investigate non-premixed flames driven by Rayleigh-Taylor (chapters 3-5) and Richtmyer-Meshkov (chapter 6) interfacial instabilities. We review some significant results below.

Rayleigh Taylor Flames: From detailed numerical simulations, we report on new pathways to stabilization and destabilization of non-premixed RT flames. A simple model based on equilibrium combustion of a 1-step reaction is used to estimate the flame induced density stratification. Across a burning interface, for  $A_{f-a} \geq 0.5$  the initial two-layer density stratification is retained while at  $A_{f-a} < 0.5$  the flame forms an active three-layer stratification such that  $\rho_{fl} < \rho_f < \rho_a$ . This simplified model is in excellent agreement with our unperturbed simulations. The two- and three-layer RT flames are then characterized by examining the evolution of single wavelength, sinusoidal perturbations in 2D and a

broadband spectrum of multimode perturbations in 3D. The underlying flow/flame configuration is novel, and proposed as a new canonical framework for understanding the broader class of non-premixed flames.

Two-Layer Flames ( $A_{f-a} \geq 0.5$ ,  $\rho_f < \rho_{fl} < \rho_a$ ): When a high- $A$ , fuel-air interface is subject to single-scale perturbations, the two-layer RT flame evolves qualitatively similar to the inert counterpart. The reacting bubbles register a higher terminal velocity explained by (a) flame-induced expansion velocity and (b) modified drag buoyancy model that accounts for the positively buoyant flame. When the flame evolves from a multimode perturbation at the fuel-air interface, the mixing zone is self-similar. The reacting mixing zone outpaces the inert counterpart due to the higher Froude number of individual, positively buoyant flame bubbles.

Three-Layer Flames ( $A_{f-a} < 0.5$ ,  $\rho_{fl} < \rho_f < \rho_a$ ): For both initially unstable ( $gA_{f-a} < 0$ ) and stable ( $gA_{f-a} > 0$ ) configurations, combustion generates an intervening layer of reaction zone products that fundamentally alters the ensuing dynamics – a stable RT-layer is rendered unstable at the fuel-flame interface, while an unstable problem is rendered stable. The globally *unstable* ( $gA_{f-a} < 0$ ) flame with single-mode perturbation, exhibits fuel surface stability due to locally RT stable fuel-flame stratification. The fuel surface does not grow until breached by the advancing spikes of the unstable flame-air interface, and thereafter grows purely due to inertia. The duration of stability observed in our simulation is well predicted by a simple model (equation 5.2). Burning at the globally *stable* interface ( $gA_{f-a} > 0$ ) renders the fuel-flame interface unstable while the stability of the air surface is retained till late times. Under the influence of multimode perturbations, the reacting mixing width grows asymmetrically towards air/fuel stream for a globally

unstable/stable configuration. The three-layer flames also evolve self-similarly with a lower spike growth rate, while the growth of the reacting bubbles is enhanced for the same reasons as two-layer turbulent flame.

The novel configuration investigated here can, if exploited suitably, impact the design of widely used ultra-compact combustors in which RT-driven flames play a central role. During self-similar growth, RT-unstable interfaces aggressively spread as  $\sim t^2$ , and will dominate over mixing and combustion mechanisms predicated on the Kelvin-Helmholtz instability where the flow evolves as  $\sim t$ . This is likely to yield combustor designs with greater thrust-to-weight ratios and higher combustion efficiencies. The enhanced mixing also obviates the need for additional geometric features that trapped vortices in conventional combustors to sustain a threshold level of mixing. At the same time, the partial stability regimes demonstrated here imply access to operating conditions in combustors that can result in greater control of flame properties, in particular the ability to anchor flames. Additionally, RT-driven combustion is sustained by Reynolds number growth given by  $Re \equiv \frac{h\dot{h}}{\nu} \sim t^3$ , ensuring the flow does not undergo relaminarization upon ignition due to the increased diffusivities, a common affliction that impacts several reacting flows. The statistical homogeneity of the flow in the (y-z) plane, suggests planar-averaged quantities may be represented conveniently through 1d, reduced-order turbulence models. Finally, non-premixed RT represents a Level III mixing problem in which the flow and flame dynamics are intertwined, thus allowing a simple, yet fundamental framework to investigate long-standing questions in turbulent combustion.

Richtmyer-Meshkov Flames: We have also described the growth of a single-mode, chemically-reacting RM instability, using high-resolution numerical simulations, and find

the evolution is complex, involving multiple periods of transient growth. We find that RM can be spontaneously initiated within a diffuse interface separating a fuel and an oxidizer at high temperature, even when no incident shock is specified. The burning within the reaction zone generates pressure waves that are sufficiently strong to impulsively accelerate any material line on the interface to grow through RM instability. By estimating the strength of the combustion waves, we are able to predict the observed peak growth rates of the interface for cases with large  $\Delta / h_0$  using a modified impulsive model. Here, the impulsive model must account for the finite thickness of the interface (which can itself vary with time), and for  $A < 0$  (since the pressure wave travels from heavy to light media in our simulations). To ensure the applicability of Eq. 1.5 to both slow-fast and fast-slow interactions, we have performed simulations of non-reacting RMI at a diffuse interface, under both conditions to verify the modified impulsive model. The late time dynamics of the interface is complicated by the formation of secondary instabilities (flame strands and Kelvin-Helmholtz) and density variations across the interface/flame.

The above analysis is complicated by three factors, viz. (i) the non-planar nature of the combustion waves observed for interfaces with small  $\Delta / h_0$  (and large  $kh_0$ ), (ii) decompression effects due to  $y$ -variations in the pressure gradient behind the shock front region of the blast wave, and (iii) a complex, time-varying pressure profile behind the shock front. We expect (i) - (ii) to detract from the RM growth due to a net expansion of the interface in the direction opposite to that of the RM instability growth. From our analysis, we find the growth due to decompression is not significant, and amounts to  $\sim 5\%$  of the RMI growth rate  $V_0^+$ . We expect the expansion due to non-planarity of the blast waves to be more important, however a quantitative estimate of these effects is complicated

and has not been attempted here. Nevertheless, these effects are short-lived and fleeting ( $kV_0^+(t-t_0) < 0.5$ ), and the late-time flow is governed by the baroclinic vorticity deposited by the initial shock front. This phase of growth is also influenced by the time-varying pressure profile behind the shock driving a variable-g RT, but as pointed out by [123] these effects (iii) cannot be linearly superposed. Given these complex features, it is encouraging that our simulations with large  $\Delta/h_0$  report growth rates in good agreement with the modified impulsive model with appropriate accounting for the expansion-driven, time-dependent broadening of the interface. This is likely due to the simple fact that at such large thicknesses, the original combustion reaction zone is at a sufficient remove from the interface of interest. As a result, the generated blast waves are allowed the time to stabilize to a planar configuration by the time of their interaction with the interface, thus producing a perturbation growth similar to the classical RMI. We recognize the time-dependent evolution is vastly more complex and likely involves stages of linear and non-linear RMI, followed by driven growth due to a Rayleigh-Taylor flow with variable acceleration. We defer these interesting issues to future articles, and anticipate the development of more sophisticated linear and nonlinear models to describe such phenomena.

The behavior of the unshocked, reacting flame bears similarity to laser-driven target experiments [127-131], where ablation at the target surface results in the passage of a blast wave through layers of fuel and shell material. Such experiments are used to elucidate turbulent mixing in applications such as Inertial Confinement Fusion and core collapse type Ia supernovae. The dynamics of the unshocked flames described here, point to a promising strategy for combined RT/RM experiments by initiating combustion at a

location removed from the interface, and allowing the ensuing blast waves to accelerate the perturbed interface through a series of instabilities discussed here.

When an incident shock is specified, the interface is subjected to multiple shocks traveling in opposite directions. The timing of the shocks is critical and can determine the dominant stages of growth. For instance, for  $\Delta / h_0 \leq 16$ , the combustion wave crosses the interface first, immediately followed by the passage of the incident shock which dominates the subsequent dynamics resulting in RMI-like growth. For large  $\Delta / h_0$ , the interaction with the incident shock occurs first, and is followed by the passage of a combustion wave that originates at  $\sim Z_{st}$  far away from the interface. For instance, for  $\Delta / h_0 = 64$  we find the interface acceleration to follow  $g(t) \propto (t / t_0)^a$  where  $a = -1.8$ . The 2D experiments on the OMEGA laser by Kuranz et al. [132] report blast wavedriven interface acceleration with  $a = -1.2$ . As a result, the growth at the interface appears to be modulated by the time-dependent pressure profile of a blast wave type acceleration as well as the expansion effects described above. Once again, when the growth rates are scaled with  $V_0^+ / \psi(t)$  rather than  $V_0^+$ , the peak values collapse for all cases with the exception of the simulation initialized with  $\Delta / h_0 = 64$ .

Finally, we have investigated changes to the above phenomena, when the interface and the flame are re-shocked by a shock reflected from the endwall at  $x = 6\lambda$ . Since the interface was allowed to develop to nonlinearity prior to reshock, significant mixing ensues accompanied by aggressive burning of the interface. Our preliminary results (section 6.6) indicate a marked increase in the combustion efficiency immediately following each shock

impact, highlighting the possibility of high-performance combustion devices that can be manipulated by strategically structured shock trains.

Future work: We identify some outstanding issues that we hope will be answered in future investigations of chemically reacting, non-premixed RMI phenomena. Models for blast wave driven interface growth that include the effects of decompression and non-planarity of the waves are essential to improving the applicability of Eq. 1.5 to reacting RMI. Similarly, the effect of the initial interfacial amplitude  $h_0$  (relative to perturbation wavenumber,  $k$ ) on the generation of the combustion waves, and their subsequent interaction with the material interface must be understood. Finally, the above investigation must be extended to study the growth of a multimode interface separating fuel and oxidizer. Such a problem is more representative of the configurations encountered in several applications such as Inertial Confinement Fusion, type Ia supernovae, scramjets etc. The rate limiting step in such an arrangement is the shock-driven turbulent mixing and diffusion, which would dictate the flame dynamics and combustion efficiency.

## REFERENCES

- [1] W. H. Cabot and A. W. Cook, *Nat. Phys.* **2**, 562 (2006).
- [2] P. Ramaprabhu, V. Karkhanis, and A. G. W. Lawrie, *Phys. Fluids* **25**, 115104 (2013).
- [3] G. Dimonte *et al.*, *Phys. Fluids* **16**, 1668 (2004).
- [4] A. A. Gowardhan and F. F. Grinstein, *J. Turbulence* **12**, N43 (2011).
- [5] P. E. Dimotakis, *Annu. Rev. Fluid Mech.* **37**, 329 (2005).
- [6] S. B. Pope, *Turbulent flows* (Cambridge University Press, Cambridge, England, 2000).
- [7] L. Rayleigh, *Scientific Papers II* (Cambridge University Press, Cambridge, England, 1900).
- [8] G. I. Taylor, *Proc. R. Soc. London Ser. A* **201**, 192 (1950).
- [9] R. D. Richtmyer, *Commun. Pure Appl. Math.* **13**, 297 (1960).
- [10] E. E. Meshkov, *Izv. Acad. Sci. USSR Fluid Dynamics* **4**, 101 (1969).
- [11] M. K. Smart, N. E. Hass, and A. Paull, *AIAA J.* **44**, 2366 (2006).
- [12] J. Zelina, D. T. Shouse, and R. D. Hancock, in *ASME Turbo Expo 2004: Power Land, Sea, and Air* (ASME, Vienna, Austria, 2004), pp. 53.
- [13] D. Blunck *et al.*, in *ASME Turbo Expo 2013: Turbine Tech. Conf. Exposition* (ASME, San Antonio, Texas, 2013), pp. V01AT04A026.
- [14] K. R. McManus, U. Vandsburger, and C. T. Bowman, *Combust. Flame* **82**, 75 (1990).
- [15] J. D. Lindl, *Inertial confinement fusion: The Quest for Ignition and Energy Gain Using Indirect Drive* (Springer-Verlag, New York, 1998).
- [16] A. Davaille, *Nature* **402**, 756 (1999).

- [17] M. Zingale, S. E. Woosley, C. A. Rendleman, M. S. Day, and J. B. Bell, *Astrophys. J.* **632**, 1021 (2005).
- [18] M. Herant, W. Benz, W. R. Hix, C. L. Fryer, and S. A. Colgate, *Astrophys. J.* **435**, 339 (1994).
- [19] C.-Y. Wang and R. A. Chevalier, *Astrophys. J.* **549**, 1119 (2001).
- [20] B. D. Marsh and I. S. E. Carmichael, *J. Geophys. Res.* **79**, 1196 (1974).
- [21] S. Zhong and M. T. Zuber, *Earth Planet. Sci. Lett.* **189**, 75 (2001).
- [22] C. S. Huang, M. C. Kelley, and D. L. Hysell, *J. Geophys. Res.* **98**, 15631 (1993).
- [23] W. A. Sirignano, D. Dunn-Rankin, F. Liu, B. Colcord, and S. Puranam, *AIAA J.* **50**, 1645 (2012).
- [24] A. Ghosh, PhD dissertation, University of Maryland, College Park, 2008.
- [25] D. L. Youngs, *Laser Part. Beams* **12**, 725 (1994).
- [26] G. Dimonte and M. Schneider, *Phys. Rev. E* **54**, 3740 (1996).
- [27] S. B. Dalziel, P. F. Linden, and D. L. Youngs, *J. Fluid Mech.* **399**, 1 (1999).
- [28] S. Chandrasekhar, *Hydrodynamic and Hydromagnetic Stability* (Oxford University Press, 1961).
- [29] V. N. Goncharov, *Phys. Rev. Lett.* **88**, 134502 (2002).
- [30] P. Ramaprabhu, G. Dimonte, and M. J. Andrews, *J. Fluid Mech.* **536**, 285 (2005).
- [31] P. Ramaprabhu and M. J. Andrews, *J. Fluid Mech.* **502**, 233 (2004).
- [32] M. Chertkov, V. Lebedev, and N. Vladimirova, *J. Fluid Mech.* **633**, 1 (2009).
- [33] A. Petchenko, V. Bychkov, V. Akkerman, and L.-E. Eriksson, *Phys. Rev. Lett.* **97**, 164501 (2006).
- [34] K. O. Mikaelian, *Phys. Fluids* **6**, 356 (1994).

- [35] G. Dimonte and P. Ramaprabhu, *Phys. Fluids* **22**, 014104 (2010).
- [36] M. Brouillette, *Annu. Rev. Fluid Mech.* **34**, 445 (2002).
- [37] A. M. Khokhlov, E. S. Oran, and G. O. Thomas, *Combust. Flame* **117**, 323 (1999).
- [38] E. S. Oran and V. N. Gamezo, *Combust. Flame* **148**, 4 (2007).
- [39] M. Nishioka and C. K. Law, *Combust. Flame* **108**, 199 (1997).
- [40] K. Takita and T. Niioka, in *Symp. Int. Combust.* (Elsevier, 1996), pp. 2877.
- [41] T. Fujimori, M. Murayama, J. Sato, H. Kobayashi, S. Hasegawa, and T. Niioka, *Int. J. Energ. Mater. Chem. Propul.* **5** (2002).
- [42] K. A. Meyer and P. J. Blewett, *Phys. Fluids* **15**, 753 (1972).
- [43] M. Brouillette and B. Sturtevant, *J. Fluid Mech.* **263**, 271 (1994).
- [44] G. H. Markstein, *Nonsteady flame propagation* (Pergamon, Oxford, 1964).
- [45] J. M. Picone, E. S. Oran, J. P. Boris, and T. R. Young Jr, Theory of vorticity generation by shock wave and flame interactions. NRL, Memo. Rep. 5366, 1984.
- [46] M. Gui, B. Fan, G. Dong, and J. Ye, *Shock Waves* **18**, 487 (2009).
- [47] Y. Ju, A. Shimano, and O. Inoue, in *Symp. (Int.) Combust.* (Elsevier, Boulder, Colorado, USA, 1998), pp. 735.
- [48] G. A. Batley, A. C. McIntosh, and J. Brindley, *Proc. R. Soc. London Ser. A* **452**, 199 (1996).
- [49] H. H. Teng, Z. L. Jiang, and Z. M. Hu, *Acta Mech. Sin.* **23**, 343 (2007).
- [50] N. Haehn, D. Ranjan, C. Weber, J. Oakley, D. Rothamer, and R. Bonazza, *Combust. Flame* **159**, 1339 (2012).
- [51] L. Massa and P. Jha, *Phys. Fluids* **24**, 056101 (2012).

- [52] A. M. Khokhlov, E. S. Oran, A. Y. Chtchelkanova, and J. C. Wheeler, *Combust. Flame* **117**, 99 (1999).
- [53] N. J. Georgiadis, D. P. Rizzetta, and C. Fureby, *AIAA J.* **48**, 1772 (2010).
- [54] F. F. Grinstein, L. G. Margolin, and W. J. Rider, *Implicit Large Eddy Simulation: Computing Turbulent Fluid Dynamics* (Cambridge University Press, New York, 2010).
- [55] B. Fryxell *et al.*, *Astrophys. J. Suppl. Ser.* **131**, 273 (2000).
- [56] P. Colella and P. R. Woodward, *J. Comput. Phys.* **54**, 174 (1984).
- [57] C. Fureby and F. F. Grinstein, *AIAA J.* **37**, 544 (1999).
- [58] B. Thornber, A. Mosedale, and D. Drikakis, *J. Comput. Phys.* **226**, 1902 (2007).
- [59] D. H. Porter, A. Pouquet, and P. R. Woodward, *Phys. Rev. Lett.* **68**, 3156 (1992).
- [60] P. MacNeice, K. M. Olson, C. Mobarrry, R. de Fainchtein, and C. Packer, *Comput. Phys. Commun.* **126**, 330 (2000).
- [61] A. S. C. FLASH, *Flash user's guide* (University of Chicago, Chicago, 2010).
- [62] S. K. Godunov, *Matematicheskii Sbornik* **89**, 271 (1959).
- [63] P. Kaps and P. Rentrop, *Numerische Mathematik* **33**, 55 (1979).
- [64] G. Bader and P. Deuflhard, *Numerische Mathematik* **41**, 373 (1983).
- [65] I. S. Duff, A. M. Erisman, and J. K. Reid, *Direct methods for sparse matrices* (Clarendon Press Oxford, 1986).
- [66] G. P. Smith *et al.*, Retrieved from: [www .me .berkeley .edu /gri\\_mech](http://www.me.berkeley.edu/gri_mech) (1999).
- [67] P. J. Linstrom and W. G. Mallard, *J. Chem. Eng. Data* **46**, 1059 (2001).
- [68] H. Schlichting and K. Gersten, *Boundary-layer theory* (Springer Verlag, Berlin, 2000).
- [69] P. C. Babu and K. Mahesh, *Phys. Fluids* **16**, 3699 (2004).

- [70] H. J. Lugt, *Introduction to vortex theory* (Vortex Flow Press Potomac, Maryland, 1996).
- [71] B. J. McBride, S. Gordon, and M. A. Reno, NASA Tech. Memo. **4513** (1993).
- [72] S. Mathur, P. K. Tondon, and S. C. Saxena, Mol. Phys. **12**, 569 (1967).
- [73] C. R. Wilke, J. Chem. Phys. **18**, 517 (1950).
- [74] B. E. Poling, J. M. Prausnitz, and O. C. John Paul, *The properties of gases and liquids* (McGraw-Hill New York, 2001), Vol. 5.
- [75] A. Burcat and B. Ruscic, *Third millenium ideal gas and condensed phase thermochemical database for combustion with updates from active thermochemical tables* (Argonne National Laboratory Argonne, IL, 2005).
- [76] G. Billet, J. Comput. Phys. **204**, 319 (2005).
- [77] J. A. Miller, R. E. Mitchell, M. D. Smooke, and R. J. Kee, in *Symp. (Int.) Combust.* (Elsevier, Hafia, Israel, 1982), pp. 181.
- [78] M. A. Mueller, T. J. Kim, R. A. Yetter, and F. L. Dryer, Int. J. Chem. Kinet. **31**, 113 (1999).
- [79] J. Doom and K. Mahesh, Combust. Flame **156**, 813 (2009).
- [80] V. Katta and W. Roquemore, Combust. Flame **102**, 21 (1995).
- [81] F. Takahashi, M. Mizomoto, S. Ikai, and T. N. Veziroglu, *Alternative energy sources III: Nuclear energy/synthetic fuels* (McGraw-Hill, New York, 1983), Vol. 5.
- [82] N. Attal, P. Ramaprabhu, J. Hossain, V. Karkhanis, M. Uddin, J. R. Gord, and S. Roy, Comput. Fluids **107**, 59 (2015).
- [83] M. Zingale *et al.*, Astrophys. J. Suppl. Ser. **143**, 539 (2002).

- [84] R. W. Bilger, in *Symp. (Int.) Combust.* (Elsevier, Pittsburgh, Pennsylvania, USA, 1989), pp. 475.
- [85] R. Hilbert, D. Thévenin, and L. Vervisch, in *Direct and Large-Eddy Simulation IV* (Springer Dordrecht, Netherlands, 2001), pp. 121.
- [86] M. Latini, O. Schilling, and W. S. Don, *J. Comput. Phys.* **221**, 805 (2007).
- [87] R. E. Duff, F. H. Harlow, and C. W. Hirt, *Phys. Fluids* **5**, 417 (2004).
- [88] G. Dimonte, P. Ramaprabhu, D. L. Youngs, M. J. Andrews, and R. Rosner, *Phys. Plasmas* **12**, 056301 (2005).
- [89] J. H. Chen, *Proc. Combust. Inst.* **33**, 99 (2011).
- [90] R. Yu, X.-S. Bai, and A. N. Lipatnikov, *J. Fluid Mech.* **772**, 127 (2015).
- [91] E. Giacomazzi, F. R. Picchia, and N. Arcidiacono, *Combust. Theory Modell.* **12**, 135 (2008).
- [92] N. Attal and P. Ramaprabhu, *Shock Waves* **25**, 307 (2015).
- [93] CERFACS, Retrieved from: [elearning.cerfacs.fr/combustion/tools/adiabaticflametemperature/index.php](http://elearning.cerfacs.fr/combustion/tools/adiabaticflametemperature/index.php) (2012).
- [94] G. Dimonte, P. Ramaprabhu, and M. Andrews, *Phys. Rev. E* **76**, 046313 (2007).
- [95] P. Ramaprabhu, V. Karkhanis, R. Banerjee, H. Varshochi, M. Khan, and A. Lawrie, *Phys. Rev. E* **93**, 013118 (2016).
- [96] P. Ramaprabhu and G. Dimonte, *Phys. Rev. E* **71**, 036314 (2005).
- [97] P. Ramaprabhu, G. Dimonte, Y.-N. Young, A. C. Calder, and B. Fryxell, *Phys. Rev. E* **74**, 066308 (2006).
- [98] P. Ramaprabhu, G. Dimonte, P. Woodward, C. Fryer, G. Rockefeller, K. Muthuraman, P.-H. Lin, and J. Jayaraj, *Phys. Fluids* **24**, 074107 (2012).

- [99] D. Layzer, *Astrophys. J.* **122**, 1 (1955).
- [100] D. Shvarts, U. Alon, D. Ofer, R. L. McCrory, and C. P. Verdon, *Phys. Plasmas* **2**, 2465 (1995).
- [101] G. Dimonte, *Phys. Plasmas* **7**, 2255 (2000).
- [102] B. Cheng, J. Glimm, and D. H. Sharp, *Phys. Rev. E* **66**, 036312 (2002).
- [103] Y. G. Cao, W. K. Chow, and N. K. Fong, *Commun. Theor. Phys.* **56**, 751 (2011).
- [104] S. Bouquet, P. Gandeboeuf, and P. Pailhories, *Math. Methods Appl. Sci.* **30**, 2027 (2007).
- [105] Y. Srebro, Y. Elbaz, O. Sadot, L. Arazi, and D. Shvarts, *Laser Part. Beams* **21**, 347 (2003).
- [106] A. Banerjee, W. N. Kraft, and M. J. Andrews, *J. Fluid Mech.* **659**, 127 (2010).
- [107] D. H. Sharp, *Physica D* **12**, 3 (1984).
- [108] G. Dimonte and M. Schneider, *Phys. Fluids* **12**, 304 (2000).
- [109] B. J. Daly, *Phys. Fluids* **10**, 297 (1967).
- [110] P. V. Danckwerts, *Appl. Sci. Res. A* **3**, 279 (1952).
- [111] D. L. Youngs, *Phys. Fluids A* **3**, 1312 (1991).
- [112] N. M. Hoffman, *Hydrodynamic instabilities in inertial confinement fusion. Laser Plasma Interactions 5: Inertial Confinement Fusion* (Institute of Physics Publishing, New York, 1995).
- [113] J. W. Jacobs and S. B. Dalziel, *J. Fluid Mech.* **542**, 251 (2005).
- [114] P.-H. Renard, J. C. Rolon, D. Thévenin, and S. Candel, *Combust. Flame* **117**, 189 (1999).

- [115] P.-H. Renard, D. Thevenin, J.-C. Rolon, and S. Candel, *Prog. Energy Combust. Sci.* **26**, 225 (2000).
- [116] D. O. Lignell, J. H. Chen, P. J. Smith, T. Lu, and C. K. Law, *Combust. Flame* **151**, 2 (2007).
- [117] J. A. Domaradzki, Z. Xiao, and P. K. Smolarkiewicz, *Phys. Fluids* **15**, 3890 (2003).
- [118] A. Aspden, N. Nikiforakis, S. Dalziel, and J. Bell, *Comm App Math Comp Sci* **3**, 103 (2009).
- [119] B. Thornber and D. Drikakis, *AIAA J.* **46**, 2634 (2008).
- [120] B. Thornber, D. Drikakis, D. L. Youngs, and R. J. R. Williams, *J. Fluid Mech.* **654**, 99 (2010).
- [121] Z. A. Rana, B. Thornber, and D. Drikakis, *Phys. Fluids* **23**, 046103 (2011).
- [122] D. Ranjan, J. H. J. Niederhaus, J. G. Oakley, M. H. Anderson, R. Bonazza, and J. A. Greenough, *Phys. Fluids* **20**, 036101 (2008).
- [123] A. R. Miles, *Phys. Plasmas* **11**, 5140 (2004).
- [124] A. R. Miles, D. G. Braun, M. J. Edwards, H. F. Robey, R. P. Drake, and D. R. Leibbrandt, *Phys. Plasmas* **11**, 3631 (2004).
- [125] C. C. Kuranz, PhD dissertation, The University of Michigan, Ann Arbor, 2009.
- [126] E. Bourguignon, M. R. Johnson, and L. W. Kostiuk, *Combust. Flame* **119**, 319 (1999).
- [127] S. G. Glendinning *et al.*, *Phys. Rev. Lett.* **69**, 1201 (1992).
- [128] S. Fujioka *et al.*, *Phys. Rev. Lett.* **92**, 195001 (2004).
- [129] S. Fujioka, H. Shiraga, M. Nishikino, K. Shigemori, A. Sunahara, M. Nakai, H. Azechi, K. Nishihara, and T. Yamanaka, *Phys. Plasmas* **10**, 4784 (2003).

- [130] C. J. Pawley *et al.*, Phys. Plasmas **4**, 1969 (1997).
- [131] A. J. Cole, J. D. Kilkenny, P. T. Rumsby, R. G. Evans, C. J. Hooker, and M. H. Key, Nature **299**, 329 (1982).
- [132] C. C. Kuranz *et al.*, Astrophys. J. **696**, 749 (2009).

## APPENDIX A: FLASH VALIDATION

We present verification of the modifications described in chapter 2 to the FLASH code, not reported in [82].

Verification of EOS:

The EOS unit was verified by computing temperature and adiabatic indices for species at different temperatures, and comparing with data compiled by NIST[67]. The EOS unit is invoked in the *Density–Pressure* ( $\rho, P$ ) and *Density–Internal Energy* ( $\rho, \varepsilon$ ) modes for nitrogen, hydrogen, and oxygen with the computed gas properties compared with highly accurate experimental or quantum mechanics simulation data from various sources[67]. Our simulations were performed with a 1D computational domain with outflow boundaries at the extremities. The computational domain was initialized with one of the above mentioned species ( $N_2$ ,  $O_2$ , or  $H_2$ ) at 1atm pressure and constant density, while the internal energy, temperature and adiabatic index were initialized with the values calculated by the EOS module in *Density–Pressure* ( $\rho, P$ ) mode. Note that since the fluid is at rest, the solution to the Euler equations and the thermodynamic properties are in steady-state. The Hydro unit calls the EOS in *Density–Internal Energy* mode ( $\rho, \varepsilon$ ) after solving the Euler equations.

The above procedure was repeated for different values of density for each species ( $N_2$ ,  $O_2$ , and  $H_2$ ). Figures A.1 (a), (b) and (c) are plots of the temperature, and the adiabatic index ( $\gamma$ ) each plotted against the input densities for hydrogen, oxygen, and nitrogen respectively. The results from FLASH are in good agreement with NIST data, for all values of the input density. Figures A.1(a) - (c) verify the implementation of the multi-species

EOS unit, as well as the implementation of the Newton-Raphson method for the solution of temperature in equation (2.18).

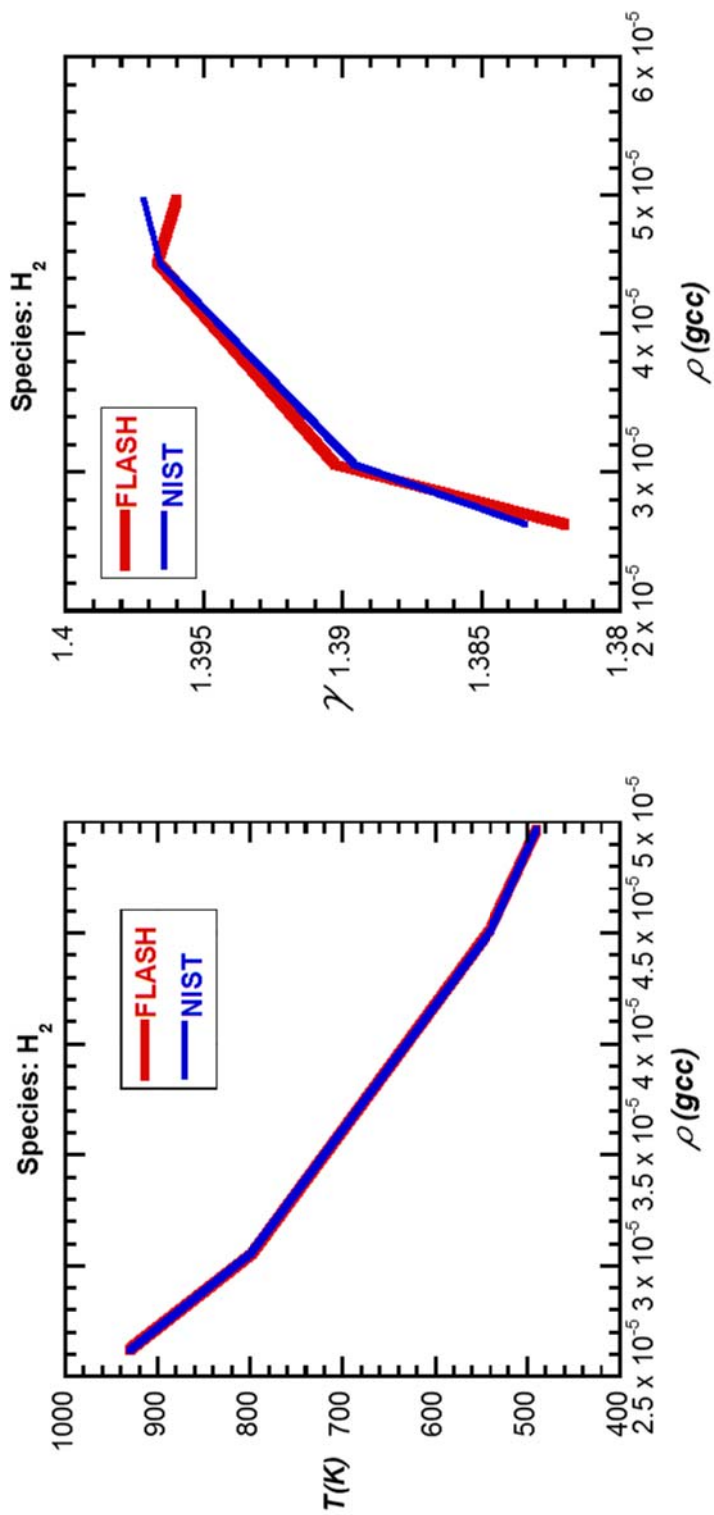


FIGURE A.1 (a) :Temperature and adiabatic index ( $\gamma$ ) for hydrogen from FLASH compared with high accuracy data compiled by NIST[67] at different densities.

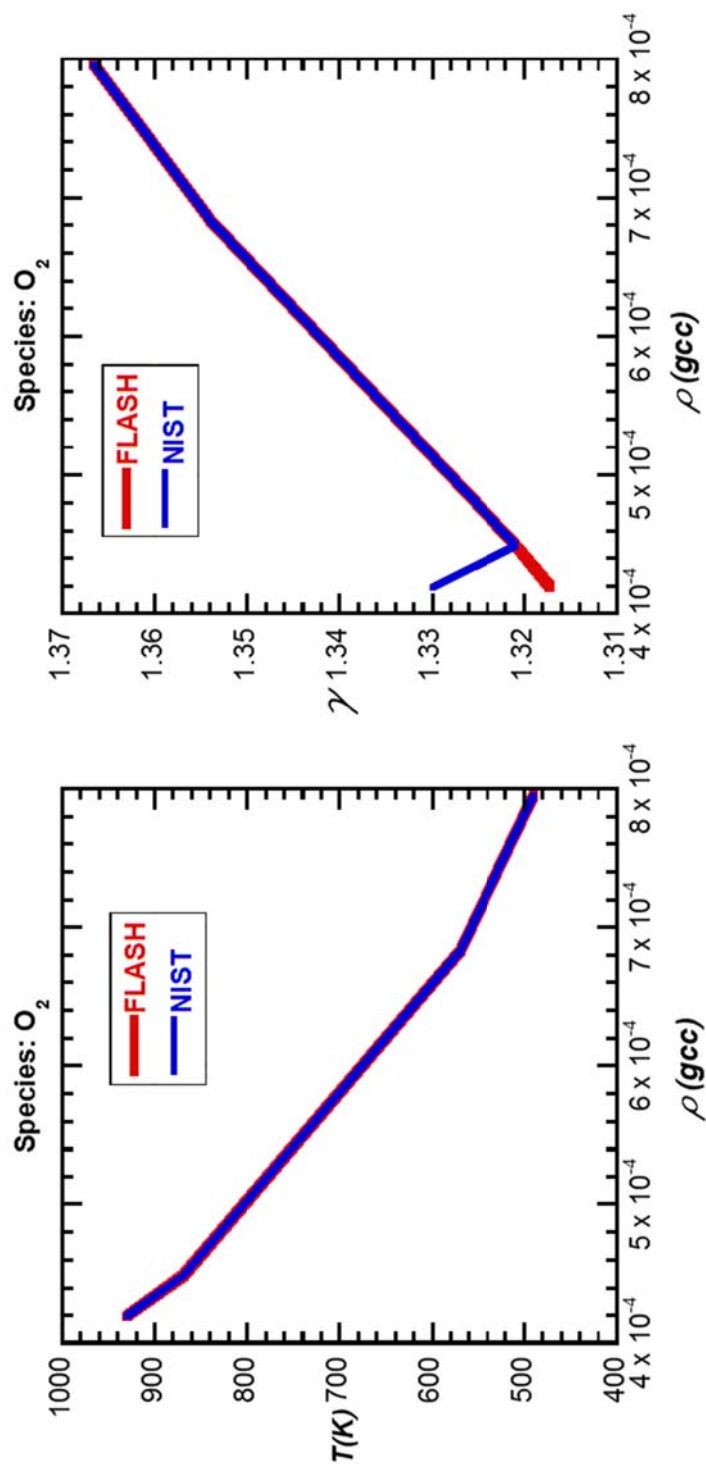


FIGURE A.1(b): Temperature and adiabatic index ( $\gamma$ ) for oxygen from FLASH compared with high accuracy data compiled by NIST[67] at different densities.

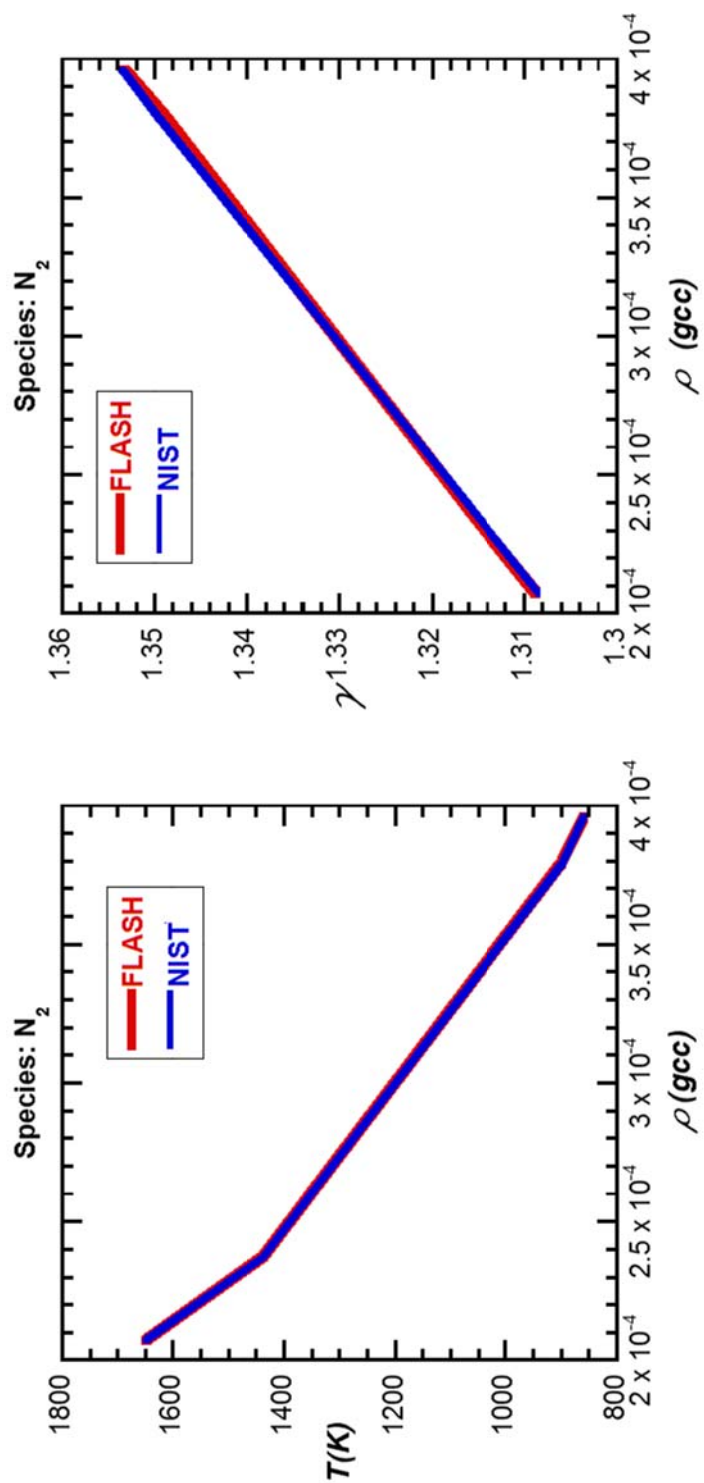


FIGURE A.1(c): Temperature and adiabatic index ( $\gamma$ ) for nitrogen from FLASH compared with high accuracy data compiled by NIST[67] at different densities.

### Laminar jet calculation:

We present the verification of the flux-based viscous diffusion implementation by comparing the axial velocity decay of a non-reacting, axisymmetric laminar jet with the analytical solution from [68] and the DNS results of [69].

Figure A.2 is a schematic of the 2D computational domain used in the FLASH simulation. Inlet flow with a constant velocity  $U_0 = 0.5$  cm/s is confined to the region  $0 \leq r \leq 100$  cm. The flow leaves the domain through the outlet boundary at  $x = 200$  cm, through the imposed outflow boundary condition on that surface. Outflow conditions in FLASH, which in actuality allow outflow and inflow across the surfaces on which they are imposed, are also enforced on the far radial boundary ( $r = 100$  cm), and in the recessed inlet region shown in figure. The recessed back step is necessary for supplying ambient fluid entrained by the main jet. Finally,  $r = 0$  is treated as an axis of symmetry for this cylindrical jet calculation. The simulations were performed with a resolution  $\Delta x = 0.125$  cm ( $N_x = 100$ ) and  $\Delta y = 0.25$  cm ( $N_y = 100$ ).

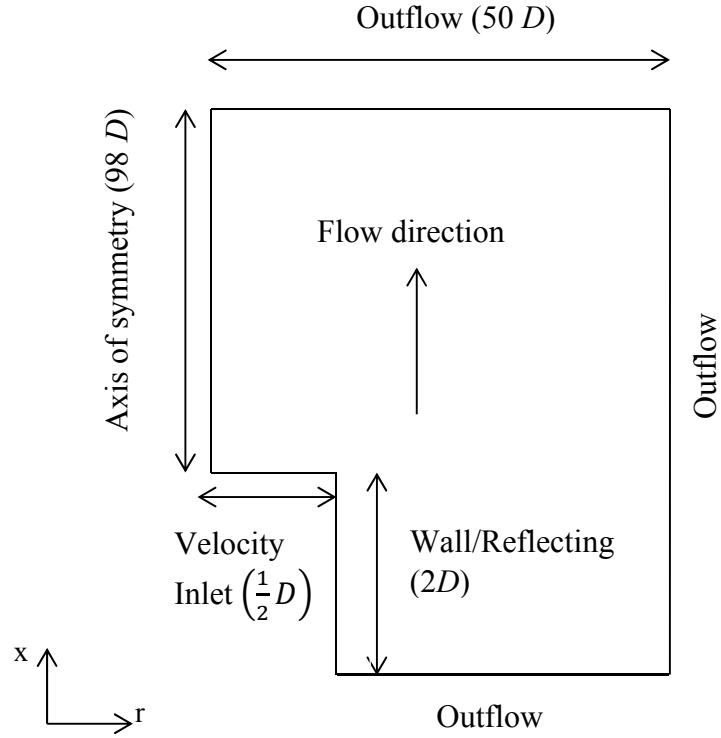


FIGURE A.2: Schematic of computational domain for simulation of 2D axisymmetric laminar jet.

Figure A.3 is a plot of the non-dimensional, axial velocity profile from FLASH alongside the DNS of [69] and the exact solution from [68]. The initial difference between the analytic solution and the numerical results (FLASH and [68]), is due to the theoretical jet originating from a point source with infinite velocity, while the computational jet is initialized with a finite inlet velocity across a nozzle, thus implying a virtual origin. The analytic solution from boundary layer theory [68] is given by

$$U_{exact} = \frac{3\pi r^2 U_0^2}{8\nu(x-x_0)}, \quad (\text{A.1})$$

where  $U_0$  is the inlet velocity (0.5cm/s),  $r$  is the jet radius (1cm),  $\nu$  is the kinematic viscosity ( $3.4 \times 10^{-3} \text{cm}^2/\text{s}$ ), and  $x_0$  is the virtual origin associated with the finite source of momentum. Extrapolating from the growth of the jet in the FLASH data, we infer a virtual origin location of  $x_0 = 35$  cm. Similarly, the plot of the radially integrated and normalized mass flux in figure A.4 shows a constant rate of entrainment for the main jet. Finally, the computational jet conserves axial momentum flux to within  $\sim 7\%$  in this steady-state simulation in figure A.4.

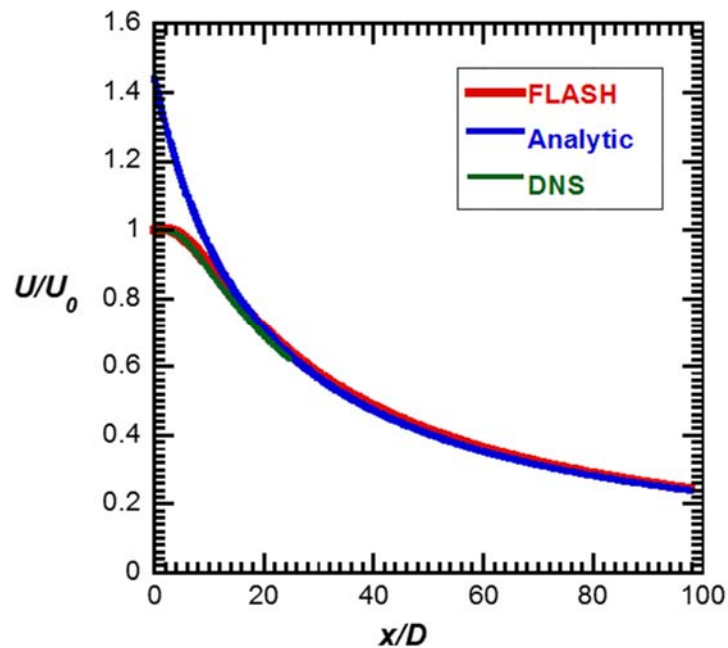


FIGURE A.3: Steady-state, non-dimensional, axial velocity from FLASH compared with DNS[69] and analytic solution[68].

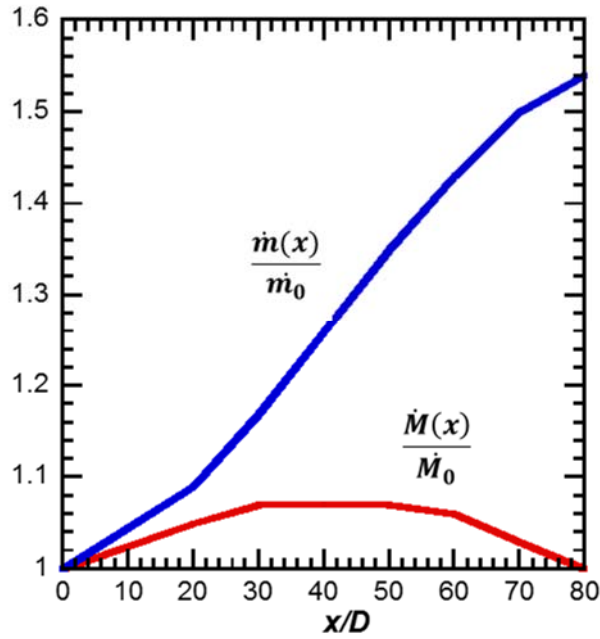


FIGURE A.4: Steady-state, non-dimensional momentum  $\dot{M}(x)/\dot{M}_0$  and mass  $\dot{m}(x)/\dot{m}_0$  fluxes from FLASH.  $\dot{M}_0$  and  $\dot{m}_0$  are inlet values.

Decay of a potential vortex:

The temporal decay of an initially ideal vortex is dictated by viscous diffusion, and serves as a demanding test problem for the viscous solvers. Analytic solutions are available from solving the symmetric Navier-stokes equations, and are provided in [70]. Here, we describe results from FLASH simulations with the viscous-diffusion equation solved by the implicit solver, as well as the flux-based method.

For a vortex of initial strength  $k_0$  and radius  $r_0$ ,  $k_0 = V_\phi r_0$  and the tangential velocity  $V_\phi$  everywhere is given by

$$V_\phi = \frac{k_0}{r} \left( 1 - e^{-\frac{r^2}{4\nu t}} \right). \quad (\text{A.2})$$

The FLASH simulations were performed in a Cartesian coordinate system with a computational domain of 40 cm in the  $x$  and  $y$  directions. The ‘initial’ conditions for the simulation was the exact solution at  $t = 0.1$ s to avoid the singularity in equation (A.2) for  $t \rightarrow 0$ . The computational domain was initialized with a uniform density and pressure field, while all boundaries were specified as ‘outflow’ surfaces. Finally, the simulations had  $\nu = 10 \text{ cm}^2/\text{s}$ ,  $r_0 = 5 \text{ cm}$ , and  $V_{\phi_0} = 2 \text{ cm/s}$ . The simulations were performed with a resolution  $\Delta x = \Delta y = 0.15625 \text{ cm}$  ( $N_x = N_y = 256$ ).

Figure A.5 is a plot of the tangential velocity at  $t = 0.1$ s,  $t = 0.2$ s and  $t = 0.5$ s from our simulations using (a) implicit and (b) flux-based diffusion, showing excellent agreement with the analytic[70] solution. On the computational Cartesian grid, the solution remained symmetric for all times for both diffusion methods.

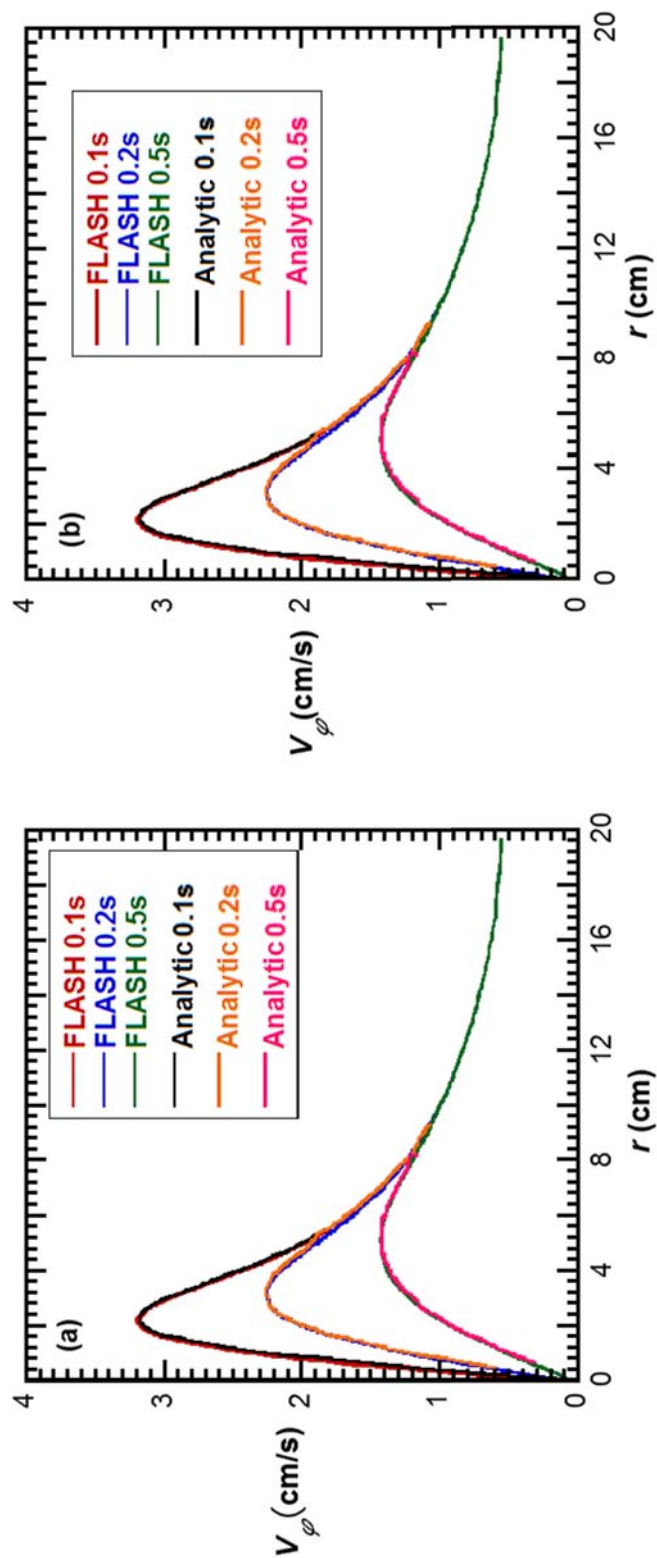


FIGURE A.5: Tangential velocity profiles in a decaying vortex at  $t = 0.1$  s (initial condition),  $t = 0.2$  s and  $t = 0.5$  s (a) analytic solution [70] and FLASH (implicit viscous diffusion), (b) analytic solution [70] and FLASH (flux-based viscous diffusion)

## 2D advection of reacting $H_2$ rings:

We have evaluated the directionally split solver with a 2D test problem involving a reacting  $H_2$  ring in a background flow. Of interest is the ability of FLASH to maintain the circular symmetry of the reacting ring as it is convected by a directional background flow. Diffusion effects are included through an implicit solver.

A circular  $H_2$  ring immersed in  $O_2$  at 1 atm pressure was advected with a uniform velocity. The location and thickness of the ring in Cartesian co-ordinate system is specified through the mass fraction of  $H_2$ ,

$$Y_{H_2} = \frac{1}{2} [1 + \tanh(C(\frac{l}{2} - |r - r_0|))], \quad (\text{A.3})$$

where,  $r_0 = \sqrt{(x_0^2 + y_0^2)}$  and  $r = \sqrt{(x^2 + y^2)}$ . In equation A.3,  $C$  determines the sharpness of the front and was specified to be  $80 \text{ cm}^{-1}$ ,  $l (= 0.6 \text{ cm})$  specify the width of the hydrogen plateau while  $x_0$  and  $y_0$  specify the center of the ring. For all the simulations presented in this section, a mesh resolution of  $\Delta x = 0.01 \text{ cm}$  and  $\Delta y = 0.01 \text{ cm}$  was employed. The Lewis number was assumed to be unity, while the boundaries were treated as outflow surfaces. Table A.1 lists the simulations performed and categorized according to the direction of the background flow. The initial configuration is shown in figures A.6 (a) and (b) through  $H_2$  mass fraction and temperature contours.

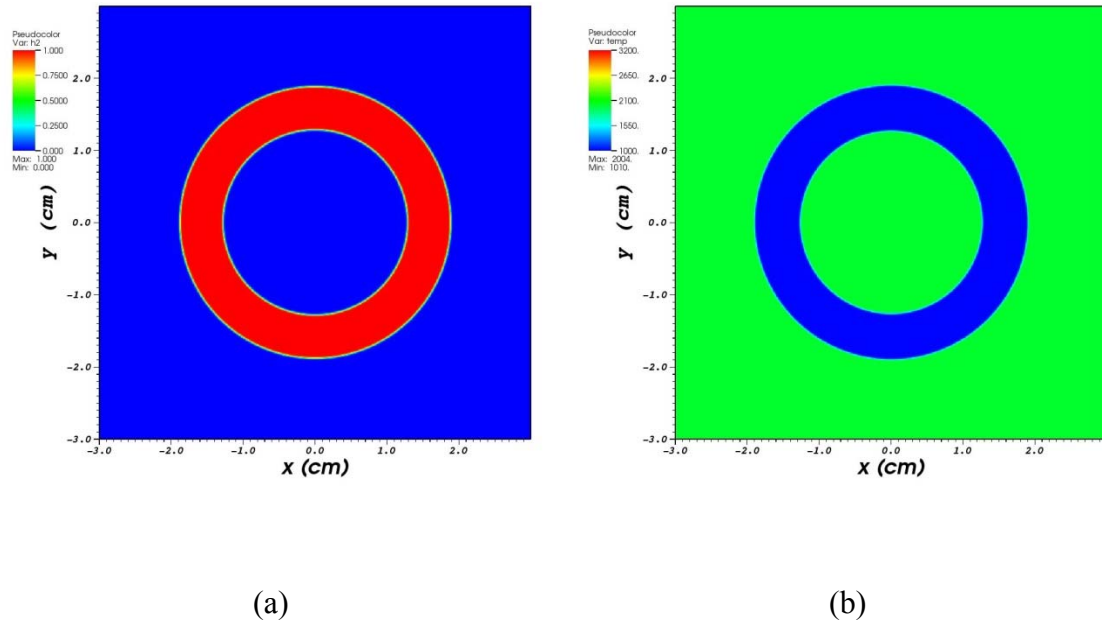
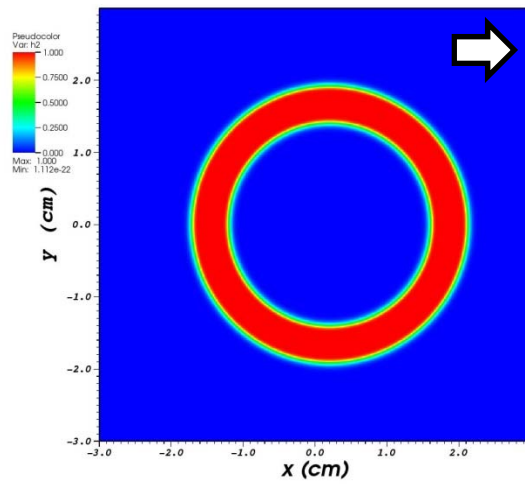


FIGURE A.6: Plots at  $t = 0$ s of (a) mass fraction of Hydrogen, and (b) temperature.

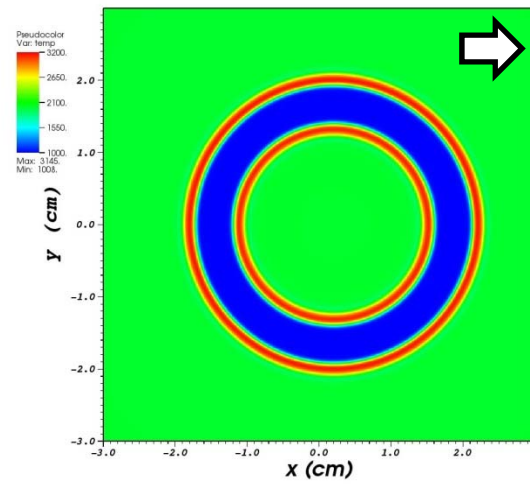
Figures A.7 (a) and (b) show contours of mass fraction of  $H_2$  and temperature at  $t = 100\mu s$  for case A.1, while figures (c) and (d) are plots of mass fraction of hydrogen and temperature for case A.2. We observe that the directionally split hydro solver in FLASH preserves radial symmetry (figure A.7), and the uniform burning of hydrogen results in a maximum temperature of  $\sim 3200K$  comparable to the analogous 1D simulation described in [82]. We also performed these simulations using the Godunov method in FLASH without diffusion effects and found that the numerical diffusion had a directional preference. When the x and y components of the velocities were non-zero and equal, circular symmetry was preserved. When the implicit diffusion solver was employed with PPM, there was no directional preference on diffusion and circular symmetry was preserved irrespective of the direction of advection. At the inner and outer periphery of the hydrogen ring, diffusion flames were formed and have the same thickness.

TABLE A.1: 2D Hydrogen ring (reacting) simulations performed using FLASH.

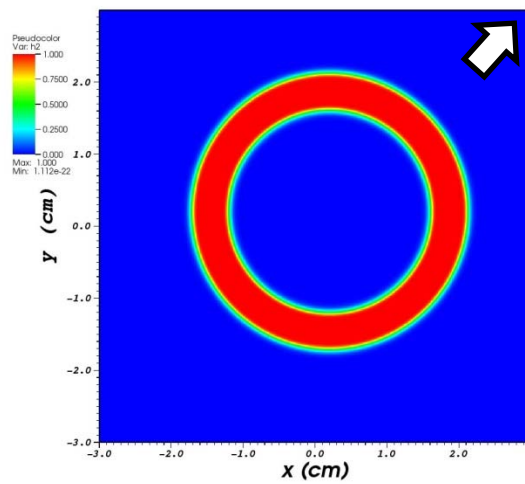
<b>CASE</b>	<b>Mass Diffusion</b>	<b>Thermal Diffusion</b>	<b>Viscous Diffusion</b>	<b><i>U</i> <i>cm/s</i></b>	<b><i>V</i> <i>cm/s</i></b>
A.1	Implicit	Implicit	Implicit	2000	0
A.2	Implicit	Implicit	Implicit	2000	2000



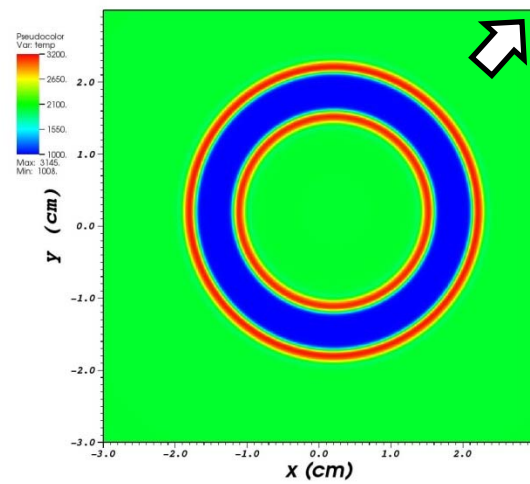
(a)



(b)



(c)



(d)

FIGURE A.7: Plots at  $t = 100\mu\text{s}$  for case A.1 (a) mass fraction of  $H_2$ , (b) temperature and case A.2 (c) mass fraction of  $H_2$ , (d) temperature.